جمهورية العراق
وزارة التعليم العـالي والبحث العلـمي
جامـــعة بـــابـــل
كليـــة العلـوم للبنات
قســـم فيزيـــاء الليزر

تحضير وتوصيف المتراكب النانوي من أوكسيد السيلكون /أوكسيد الكرافين / أوكسيد الزنك للتطبيقات الالكترونية البصرية

أطروحة

مقدمة الى مجلس كلية العلوم للبنات في جامعة بابل

كجزء من متطلبات نيل درجة الدكتوراه فلسفة في العلوم/ فيزياء الليزر وتطبيقاته

من قبل

سمية جعفر عباس

بكالوريوس في علوم فيزياء الليزر (كلية علوم البنات / جامعة بابل - 2016)
ماجستير في علوم فيزياء الليزر (كلية علوم البنات / جامعة بابل - 2019)

بأشراف

أ.م. د. أمير خضير النافعي

أ. د. رباح بوخروب

1445هـ 2023 م

Republic of Iraq
Ministry of Higher Education and
Scientific Research
University of Babylon
College of Science for Women
Laser Physics Department

Synthesis and characterizations of SiO / GO / ZnO Nanocomposites for Optoelectronic Aplications

A Thesis

Submitted to the Council of the College of Science for Women,

University of Babylon

In Partial Fulfillment of the Requirements for the Degree of

Doctor of Philosophy in Laser Physics and its Applications

By

Sumaya Jaafer Abbas

B.Sc. , Laser Physics, University of Babylon (2016)
M.Sc. Laser Physics, University of Babylon (2019)

Supervised by

Assist. Prof. Dr. Amer Khudair AL-NAFIEY

Prof. Dr. Rabah Boukherroub

2023 A.D. **1445 A.H**

بِسْمِ اللهِ الرَّحْمنِ الرَّحِيمِ

﴿هُوَ الَّذِي جَعَلَ الشَّمْسَ ضِيَاءً وَالْقَمَرَ نُورًا وَقَدَّرَهُ مَنَازِلَ لِتَعْلَمُواْ عَدَدَ السِّنِينَ وَالْحِسَابَ مَا خَلَقَ اللّهُ ذَلِكَ إِلاَّ بِالْحَقِّ يُفَصِّلُ الآيَاتِ لِقَوْمٍ يَعْلَمُونَ﴾

صَدَق الله العليّ العَظيم

سورة يونس الآية ﴿5﴾

Supervisor's certificate

I certify that this thesis entitled "***Structure , Optical and Photoelectronic properties of Si NWs / Graphene - ZnO NPS.***"

was prepared by the student (***Sumaya Jaafar Abbas***) under my supervision in the department of Laser Physics, College of Science for Women, University of Babylon, as a partial fulfillment of the requirements of the degree of Doctorate of philosophy in laser physics and its applications.

Signature:

Name: **Ass. Pro. Dr. Amer Khudair AL-Nafiey**

Title: Assistant Professor

(Supervisor)

Date: / / 2023

Head of the Department Certificate

In view of the available recommendations, I forward this dissertation for debate by the examining committee.

Signature:

Name: Jinan Ali Abd

Title: Assistant Professor

(Head of Laser Physics Department)

Examination Committee Certification

We certify that after reading this thesis, entitled: "***Structure , Optical and Photoelectronic properties of Si NWs / Graphene - ZnO NPS.***" and as committee, examined the student "***Sumaya Jaafar Abbas*** "

its contents and that in our opinion it meets the standards of a thesis for the Degree of Philosophy of Doctorate in Laser Physics and its Application.

Signature:
Name:
Dr. Ghaleb A. Al-Dahash **.**
Title: Professor
Date: / / 2023
(Chairman)

Signature:
Name:
Dr. Saif M. H. Al-Shareefi**.**
Title: Professor
Date: / / 2023
(Member)

Signature:
Name: **Dr. Oday A. Al- Owaedi**

Title: Assistant Professor
Date: / / 2023
(Member)

Signature:
Name: **Dr.**

Title: Assistant Professor
Date: / / 2023
(Member)

Signature:
Name: **Dr.**

Title: Assistant Professor
Date: / / 2023
(Member)

Signature:
Name: **Dr.**

Title: Assistant Professor
Date: / / 2023
(Member/Supervisor)

Approved by the Dean of College

Signature:
Name: **Dr. Abeer Fauzi Murad**
Title: Professor
Address: Dean of the College of Science for Women.
Date: / / 2023

Dedication

To: Army Martyrs of Iraqi

To: My Family and Friends

Acknowledgement

First of all, Praise is to Allah, mercy and peace are to the Prophet Mohammed and his relatives and companions.

I would like to express my deep thanks and gratitude to my supervisor, Assistant Professor Dr. Amer Khudair AL-Nafiey for suggesting this work and for her guidance and help.

I am deeply grateful to the Head of the Laser Physics Department, the staff, and the dean of the College of Science for Women for their support.

I wish to express my thanks to all my friends, especially the (Ph.D) group, for their kind assistance and support during our course studies and thesis work.

Sumaya

Abstract

Thin films consisting of a chemically prepared silicon oxide nanowire substrate (SiO NWs) were prepared, Graphene and zinc were then deposited on it (SiO NWs) substrate using an Nd: YAG laser with wavelength (1064 nm), pulses (200-500 pulses), where Pulsed laser deposition (PLD) has proven effective in producing thin films.

The structural properties of thin films was studied by X-ray diffraction (XRD). The results showed that (SiO NWs/G/ZnO NPs) films have the same structure. X-ray diffraction (XRD) was used to analyze the crystalline structure of the produced films and the results showed that all the prepared films were crystalline in the cubic phase for SiO NWs and the other samples. There is a decrease in the crystalline size of the nanoparticles, which is an indication of the improved properties of the prepared films.

The surface topography of the prepared films was studied using atomic force microscopy (AFM). It was observed that for the ternary compound, the grain size decreases with increasing number of laser pulses. There is also a reduction in surface roughness and RMS by increasing the number of laser pulses, and increase the density of graphene and zinc oxide.

The scanning electron microscope (SEM) results, the images show that the grain shape is spherical for all films. It can be seen that the silicon nanowires on the surface disappear due to the increased density of graphene and zinc nanowires by increasing the number of laser pulses on them, which leads to the formation of layers of materials.

Raman spectroscopy results showed that when ZnO is added to SiO NWs/GO, the G/D ratio increases leading to a value of 1.2. This indicates that the addition of ZnO leads to an increase in the regularity of the GO lattice. In

addition, the Raman spectrum of GO shows the presence of a peak around 1600 cm^{-1}, which is commonly observed in the Raman spectrum of graphene, indicating the possibility of a coating layer of reduced graphene oxide (RGO) on the SiO NWs.

The optical properties of the prepared films were studied using diffuse reflectance (UV-Vis) spectroscopy measurements in the spectral region (200-900) nm. The direct and indirect energy gap was calculated for almost all prepared films (3eV). This is the energy gap value for silicon oxide nanowire (SiO NWs), which indicates that silicon oxide nanowire is the dominant material and that the layers of graphene and zinc oxide nanowire particles are very thin films.

The electrical properties were studied as a Hall effect, where the results showed that the values of Hall constant (R_H) decrease gradually with increasing doping rates and that all prepared films are of type (p-type) because silicon is victorious. The reason mentioned above. It was also found that the conductivity increases, for example, for SiO NWs (8.54E + 01 σ (Ω.cm) $^{-1}$) while for (SiO NWs/G/ZnO NPs) (8.87E + 01 σ (Ω.cm) $^{-1}$) and vice versa for other films, the resistivity also decreases for example SiO NWS (1.17E-02 Ω.cm) while for (SiO NWS/G/ZnO NPs) (1.13E-02 Ω.cm) and vice versa for other films.

Thin film photodetector property measurements showed that all samples operated in the Vis-IR spectrum, the maximum response at approximately the wavelength (900 nm) being for the ternary compound (SiO NWS/G/ZnO NPs). Also, with regard to quantum efficiency, the maximum efficiency was (107.43%) for the ternary mixture (SiO NWS/G/ZnO NPs).

Abstract

Regarding the solar cell, the current-voltage characteristics of the hybrid junctions prepared from films (SiO NWs P-type/G/ ZnO NPs n-type) showed that the forward bias current when illuminated changes exponentially with the applied voltage and that the small efficiency values gradually increase and this is attributed to the increase in Concentration of charge carriers as a result of changing rates of doping with nanoparticles of graphene and zinc oxide.

الخلاصة

تم تحضير أغشية رقيقة تتكون من ركيزة من أسلاك أكسيد السيليكون النانوية المحضرة كيميائيًا (SiO NWs)، ثم تم ترسيب الجرافين والزنك عليها (SiO NWs) باستخدام ليزر Nd: YAG بطول موجة (1064 نانومتر)، ونبضات (200-500 نبضة).)، حيث أثبت الترسيب بالليزر النبضي (PLD) فعاليته في إنتاج الأغشية الرقيقة.

تمت دراسة الخصائص التركيبية للأغشية الرقيقة بأستخدام حيود الأشعة السينية .(XRD) أظهرت النتائج أن أغشية (SiO NWs/ G/ ZnO NPs) لها نفس البنية. تم استخدام حيود الأشعة السينية (XRD) لتحليل التركيب البلوري للأغشية المنتجة وأظهرت النتائج أن جميع الأغشية المحضرة بلورية في الطور المكعب لـ SiO NWS والعينات الاخرى. هناك انخفاض في الحجم البلوري للجسيمات النانوية ، وهذا مؤشر على الخصائص المحسنة للأغشية المحضرة.

تمت دراسة التشكيل السطحي للأغشية المحضرة باستخدام مجهر القوة الذرية(AFM). حيث لوحظ أن حجم الحبوب يتناقص مع زيادة عدد نبضات الليزر بالنسبة للمركب الثلاثي و هناك أيضًا انخفاض في معدل خشونة السطح ومعدل الجذر التربيعي (RMS) عن طريق زيادة عدد نبضات الليزر. وزيادة كثافة الجرافين وأكسيد الزنك.

بالنسبة لنتائج المجهر الإلكتروني الماسح (SEM) ، أظهرت الصور أن شكل الحبيبات كروي لجميع الأفلام. يمكن ملاحظة أن أسلاك السيليكون النانوية الموجودة على السطح تختفي بسبب زيادة كثافة الجرافين النانوي والزنك عن طريق زيادة عدد نبضات الليزر عليها ، مما يؤدي إلى تكوين طبقات من المواد.

أظهرت نتائج التحليل الطيفي لرامان أنه عند إضافة ZnO إلى SiO NWs/GO، تزداد نسبة G/D مما يؤدي إلى قيمة 1.2. يشير هذا إلى أن إضافة ZnO يؤدي إلى زيادة الانتظام في شبكة GO. بالإضافة إلى ذلك، يُظهر طيف رامان لـ GO وجود ذروة تبلغ حوالي 1600 سم -1، والتي يتم ملاحظتها بشكل شائع في طيف رامان للجرافين، مما يشير إلى إمكانية وجود طبقة طلاء من أكسيد الجرافين المخفض (RGO) على (SiO NWs).

تمت دراسة الخواص البصرية للأغشية المحضرة باستخدام قياسات التحليل الطيفي للأشعة فوق البنفسجية والأشعة المرئية (UV-VIS) للانعكاس المنتشر في المنطقة الطيفية (200-900) نانومتر. تم حساب فجوة الطاقة المباشرة والغير مباشرة لجميع الأفلام المحضرة (3ev) تقريباً وهذه قيمة فجوة الطاقة لأوكسيد السيلكون نانووايز (SiO NWs) مما يشير الى ان اوكسيد السيلكون نانووايز هو المادة المتغلبة وان طبقات جسيمات الغرافين والزنك اوكسيد النانوية اغشية رقيقة جداً.

تمت دراسة الخواص الكهربائية كتأثير هول حيث بينت النتائج قيم ثابت هول (R_H) تقل بشكل تدريجي مع زيادة نسب التشويب وان جميع الأغشية المحضرة من النوع (p-type) لأن السيليكون هو المنتصر, كما يلاحظ كذلك انخفاض قيم تحركية حاملات الشحنة (μ_H) لنفس السبب المذكور أعلاه. كذلك وجد أن الموصلية تزيد على سبيل المثال (SiO NWs (8.54E + 01 σ (Ω.cm) $^{-1}$ بينما بالنسبة لل (SiO NWs/G/ZnO NPs) (8.87E + 01 σ (Ω.cm) $^{-1}$) والعكس صحيح للأفلام

الأخرى ، تنخفض أيضًا المقاومية على سبيل المثال (1.17E-02 Ω.cm) SiO NWS بينما للمركب الثلاثي (1.13E-02 Ω.cm) وبالعكس للأفلام أخرى.

أظهرت قياسات خصائص جهاز الكشف الضوئي للأغشية الرقيقة أن جميع العينات تعمل في طيف VIS-IR ، أقصى استجابة عند الطول الموجي (900 نانومتر) تقريبًا كانت للمركب الثلاثي (SiO NWS/G/ZnO NPs). كذلك بالنسبة للكفاءة الكمية كانت أقصى كفاءة (107.43 %) للمركب الثلاثي (SiO NWS/G/ZnO NPs).

بالنسبة الى الخلية الشمسية أظهرت خصائص تيار- جهد للمفارق الهجينة المحضرة من الأغشية (SiO NWs P-type/G/ ZnO NPs n-type) ان تيار الانحياز الامامي عند الاضاءة يتغير اسيا مع الجهد المطبق وان قيم الكفاءة صغيرة تزداد تدريجيا ويعزى ذلك الى زيادة تركيز حاملات الشحنة نتيجة لتغير نسب التطعيم بجزيئات نانوية من الغرافين وأوكسيد الزنك .

Table of Contents

List of Symbols

Symbol	Physical meaning
D_m	The supersaturation of laser plasma
k_B	Boltzmann's Constant
T_s	substrate temperature
R_a	The actual deposition rate
R_e	The deposition rate of the thin film
n_o, p_o	The equilibrium carrier concentrations
n_i	The intrinsic carrier concentrations
λ	Wavelength
d_{hkl}	The interplanar distance
hkl	Miller indices
θ	Bragg diffraction angle
a	The lattice spacing Constant
D	Average Crystallite Size
β	The full width at half maximum
δ	Dislocation Density
ε	Microstrain
I_A	The intensity of absorbed light
I_o	The intensity of incident light
A	Absorbance
I_T	The intensity of transmitting rays

List of Symbols

T	Transmittance
R	Reflectance
λ_{max}	The maximum wavelength
h	Planck constant
ν	The incident photon frequency
c	The velocity of light in a vacuum
α	Absorption Coefficient
t	The thickness of the film
E_g	Optical band gap
E_a	Activation energy
E_P	The energy of an absorbed or emitted phonon
n_c	Complex refractive index
n	The refractive index
k_o	Extinction Coefficient
ε_r	The real part of dielectric constant
ε_i	The imaginary part of dielectric constant
R_H	Hall coefficient
V_H	Hall voltage
B	The magnetic field
p	The carriers concentrations of holes
n	The carriers concentrations of electrons

List of Symbols

e	The charge of the electrons
μ_p	The mobility for holes
μ_n	The mobility for electrons
σ_p	The Conductivity of holes
σ_n	The Conductivity of electrons
σ	Electrical Conductivity
μ_H	Hall Mobility
I-V	Current-Voltage
I_{Ph}	Photocurrent
I_{sc}	Short circuit current
V_{oc}	Open circuit voltage
I_s	The reverse saturation current
I_L	The light generated current
R_s	The series resistance
R_{sh}	The shunt resistance
V_m	Maximum voltage
I_m	Maximum current
F.F	Fill Factor
η	Conversion efficiency
P_o	Maximum power
P_{in}	Input power
S	Sensitivity

List of Symbols

R_a	The resistance of the sensor in the air
R_g	The resistance of the sensor in the presence of a gas
I_a	Sample current measured at ambient environment
I_g	Sample current measured under the test gas
τ_{res}	The response time
τ_{rec}	The recovery time
x	The width of the light fringes
y	The width of the dark fringes

List of Abbreviations

Symbol	Physical meaning
PVD	Physical Vapour Deposition
CVD	Chemical Vapour Deposition
PLD	Pulse Laser Deposition
XRD	X-Ray Diffraction
SEM	Scanning Electron Microscopy
AFM	Atomic Force Microscopy
XPS	X-ray Photoelectron Spectroscopy
HJ	Heterojunction
HF	Hydrofluoric acid
SiO	Silicon oxide
G	Graphene
ZnO	Zinc oxide
NWs	Nanowires
NPs	Nanoparticales
IR	Infrared
FWHM	Full Width at Half Maximum
V.B	Valence Band
C.B	Conduction Band
PV	Photovoltaic
Nd:YAG	Neodymium-doped yttrium aluminium garnet

List of Abbreviation

3D	Three-dimensional
RT	Room temperature
RMS	Root Mean Square
Ra	Roughness
Avg.C.s	Average Crystalline size
UV	Ultra Violet
Vis	Visible Spectrum

List of Tables

List of Figures

List of Figures

List of Figures

Chapter One

General Introduction

Chapter Two

Theoretical Part

Chapter Three

The Experimental Part

Chapter Four

Results and Discussion

References

1.1 Introduction

Nanoscience is the study and characterization of nanomaterials as well as their chemical and physical properties and the study of accompanying phenomena resulting from their miniaturization. As known, the term "nanoscale" refers to (10^{-9} m) and has gotten much attention and excitement, which is the key to today's advances in science and knowledge [1].

This technology is the beginning to infiltrate some commercial areas or applications, and there are no limits to the potential applications that are currently being tested. Photodetection devices are one of these applications [2].

1.2 Nanomaterials

Nanomaterials have played an important role in the development of the field of nanoscience and technology. It is defined as a group of materials whose dimensions or internal dimensions (1-100 nanometers) are covered, which is a billionth of a meter, which is the nanometer scale [3].

Nanomaterials show new optical, magnetic, electrical and a number of other properties. These properties have many applications in electronics, medicine and various other applied fields. As in Figure (1-1), which shows the dimensions of some nanomaterials [4].

Nanotechnology is an interdisciplinary field of physics, chemistry and materials science concerned with the design, manufacture and application of nanomaterials. This branch of science aims to understand the basic physical and chemical properties of nanomaterials and nanostructure, and due to the diversity and novelty of the application of

nanomaterials, the science of nanomaterials has developed accordingly and has become at the forefront of applied research interests [5]. In the past three decades, many inventions have been discovered in the field of nanoscience in terms of controlling the manufacture of new materials (controlling shape and size through innovative techniques) and benefiting from them for various applications [6].

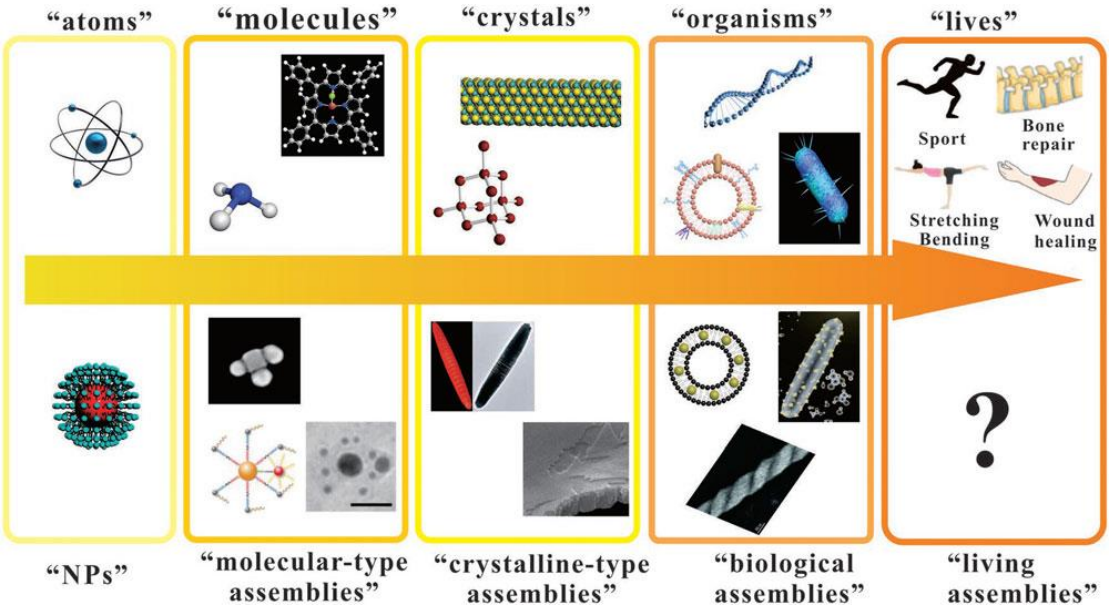

Fig. (1-1) shows nano-dimensional images of atoms and living organisms [4].

Sometimes inert materials at the large scale are active when they are produced at the nanoscale, that is, when the particles that make up the material are reduced, a very large proportion of the atoms are present on the surface compared to those on the inside. The particles that have a size of 30 nm are present only 5% of them on the surface, while the other with a size of 10 nm 20% of it is on the surface, and a volume of 3 nm of it 50% is on the surface, and since chemical reactions occur at the surface, the nanomaterials are more active than their counterparts in the larger space [7].

The quantitative effects begin to control the behavior of the material at the nanoscale, especially at the lower end, which affects the properties of electrical, magnetic and optical materials [8].

1.3 Synthesis of Nanomaterials

The nanomaterial can be prepared by one of two paths, one from top-down and the other from bottom-up. Through the first path, the researcher begins with a tangible size of the material under study, which gets smaller and smaller to reach the nanoscale, and the smallest size that can be reached is within the range of (1-100) nanometers, and the research is still continuing [9]. As for the other path, which is often chemical methods, it starts with single atoms as the smallest unit and then gathers together little by little in a larger structure. Through this path, the size of the products may reach from as small as (100 nm) [10].

After preparing the nano materials, their properties must be examined to confirm them using some familiar devices and techniques, the most important of which are: transmission electron microscopy (TEM), scanning electron microscope (SEM) and atomic force microscope (AFM), X-ray diffraction (XRD) and spectrophotometers, Fig.(1-2) shows the preparation of nanomaterials by the above-mentioned two paths[10].

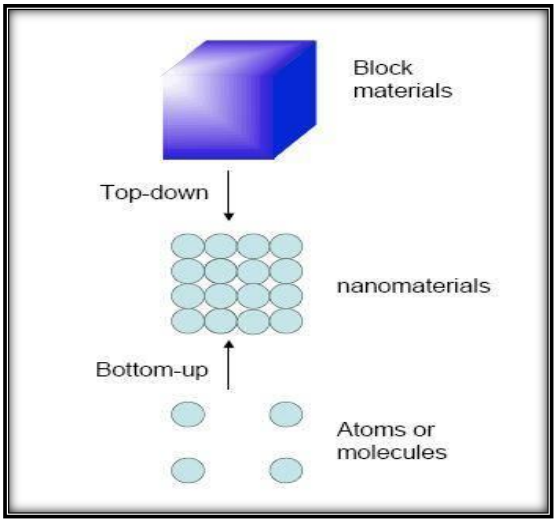

Fig. (1-2) The preparation of nanomaterials with two paths from top-down and bottom-up [10].

The great research efforts and the many different synthesis methods led to the classification of materials and nanoparticles based on dimensions, shape, composition, and agglomeration. In terms of dimensions, they are usually classified into four categories based on their dimensions: (0) dimensions, one-dimensional, two-dimensional and three-dimensional. Dimensions. Materials with a nanoscale are manufactured in several forms, the most important of which are: Quantum Dots, Nanoparticles, Nano Tubes and Nanowires (Quantum Wires) [11].

Since nanoparticles have properties different from those of bulk materials, these new materials have many applications in the electronic and photonic fields natural. As the properties of nanoparticles depend mainly on the dimensions of the material [12].

Shapes of nanoparticles are characterized by their different shapes, they may be flat, spherical, or have balanced proportions such as nanotubes, nanowires, and various shapes, including zigzag, spiral or bundle, and sometimes nanowires [13]. With variable diameters with

length, and if the aspect ratio is low, it includes spherical, cube, prismatic, oval, zigzag, or vertical shapes, where there are aggregates of nanoparticles in several forms, including powders, colloids, or plankton [14].

Nanostructured materials with custom nanoscale geometries and tunable nanostructure properties are very appealing for photo detection applications. This study will primarily concentrate on nonmetals/metal oxides such as graphene oxide (GO), Zinc oxide (ZnO), and Silicon (Si) nanostructures .

1.3.1 Silicon (Si)

Silicon is a chemical element with the atomic number 14 and the symbol Si. Silicon is a tetravalent semiconductor, but it is more reactive than germanium, which is located below it in the periodic table .

Silicon is the eighth most common element in the universe by mass, but it is rarely found in nature as a pure free element .It is widely distributed in dust, sand, and planets as various forms of silicon dioxide (silica) or silicates .More than 90 percent of the Earth's crust is made up of silicate minerals, making silicon the second most abundant element in the Earth's crust (about 28 percent by mass) after oxygen [15].

The majority of silicon is used commercially without separation, but some natural compounds are treated. These include direct industrial building uses of clay, silica sand, and stone . More modern silicon compounds, such as silicon carbide and ceramic, are excellent abrasives .

Silicon has a significant impact on the modern world's economy. Although the majority of free silicon is used in steel refining, aluminum casting, and the fine chemical industries (mostly for the production of

fumed silica), the relatively small portion of high-purity silicon used in semiconductor electronics (ten percent) is probably more important . Because silicon is widely used in integrated circuits, which are the foundation of most computers, a great deal of modern technology is based on it. [16].

Fig. (1-3) shows the spectral lines of the element silicon[15].

Silicon (Si) is preferred for the fabrication of visible and near-IR (NIR) photodetectors due to its abundance, well-matured, and cost-effective fabrication processes [17]. However, Si-based photodetectors exhibit large dark-current density, low efficiency, low photocurrent responsivity (< 0.1 A/W for wavelength < 400 nm) and limited spectral region due to the small bandgap energy (~1.12 eV) and low absorption, small temperature variations, and high reflection coefficient. To overcome these limitations, heterojunctions of Si with wide bandgap semiconductor materials is suggested [18] .

Compared with the planar counterparts and various nanostructures such as nanobelts, nanotubes, nanocages, and nanopropellers, vertically aligned nanowires (NWs) provide more surface area, reduced light reflection, fast charge transport, and increased charge collection for light-harvesting [19].

1.3.2 Graphene (G)

Graphene is a two-dimensional planar sheet of sp2-bonded carbon atoms arranged in a honeycomb crystal structure. The carbon–carbon bonds are 0.142 nm long and 120 degrees apart. The thermal and mechanical properties of carbon are due to the bonds between carbon atoms [20]. Graphene has the advantage of repairing any holes in its plates if it is exposed to carbon particles. This is a critical feature for a wide range of applications. This property works by bombarding the graphene sheet with pure carbon atoms, which adhere perfectly to the hexagonal graphene structure and thus fill the hole [21]. It can be wrapped into 0 dimension fullerenes, rolled into 1 dimension nanotubes, or stacked into 3 dimensions as graphite, as shown in Fig.(1.4) [22].

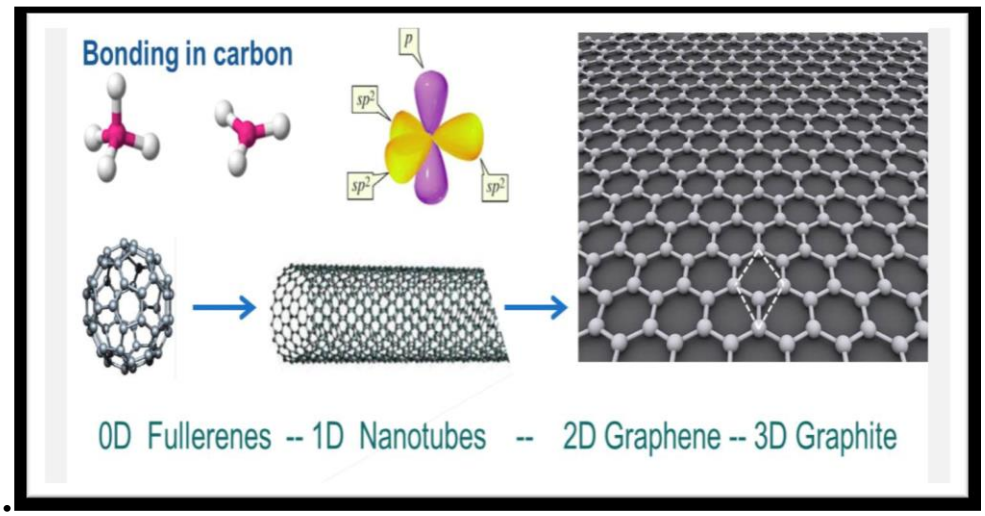

Fig. (1-4) Graphene in different forms a) Wrapped up into 0 dimension fullerenes, b)rolled into 1 dimensional nanotubes and c)stacked into 3-dimensional graphite[22].

Graphene is utilized to form a suitable heterojunction with other semiconductor materials due to its excellent properties including high mobility, high sensitivity, high current-density carrying capacity, low

resistivity, tunable Fermi level, and broadband light absorption and so on [23]. Such heterojunctions offer a high electric field beneficial for fast separation of the photo generated carriers without the application of an external bias, enabling the high performance and self-powered photodetectors [24].

However, few studies are reported demonstrating graphene and other semiconductor-based dual-heterojunction as a photodetector in the UV and IR spectrum .

1.3.3 Zinc oxide (ZnO)

Among these materials, ZnO has Semiconductor the interest of researchers due to its broad direct bandgap (3.3 eV) and properties associated with high-energy protons. A previous study's sponsor built and tested Zn-based nanostructure-related detectors. Because of the wide bandgap of ZnO, these photodetectors can only function under ultraviolet (UV) illumination [25].

Fig. (1.5) Zinc oxide [27].

Among the various wide bandgap semiconductor materials reported so far [26], zinc oxide (ZnO) demonstrates wide direct bandgap (~3.37 eV) materials with high transparency (>80%) in the visible region, large

exciton binding energy (60 mV), high UV absorption coefficient, low cost and better chemical and thermal stability at room temperature [27]. Intrinsically, ZnO material is of n-type, and hence direct p-n heterojunction can be formed by growing n-ZnO over p-type doped substrate [28].

We combine graphene with ZnO and Si as dual-heterojunction exhibits ultrafast and broadband spectral response from UV to NIR in self-powered mode [29]. The graphene layer helps in efficient carrier separation due to the tunable Fermi level. Also, it acts as an antireflection coating so as to reduce the light reflection by ~70% in the visible region and ~80% in the NIR region [30].

1.4 Interaction of Laser with Material

The laser beam must be absorbed in order for the laser to have an effect on the material. This absorption is critical for the process of laser interaction with the material to occur. This absorption process is a basic source of energy inside the material, and this basic source correctly shows that the laser beam emitted from the source determines what happens to the laser irradiated material [31], and in Figure (1-6), the incident laser pulse quickly heats the target material, causing a phase shift and generating stress waves at the radiating target. The substance then begins to melt and turn into a gaseous state in a very short period of time, and plasma is formed. The laser beam is absorbed by the plasma flame, resulting in a reduction in the intensity of the light falling on the target, as well as irritation and ionization of the plasma field, which expands away from the interaction area until it reaches the target area. The base forms a thin layer [32]. The laser beam falls on the target during the process of laser evaporation, and the material evaporates

from the target, and the vaporized material moves to the base and is deposited on it [33] .

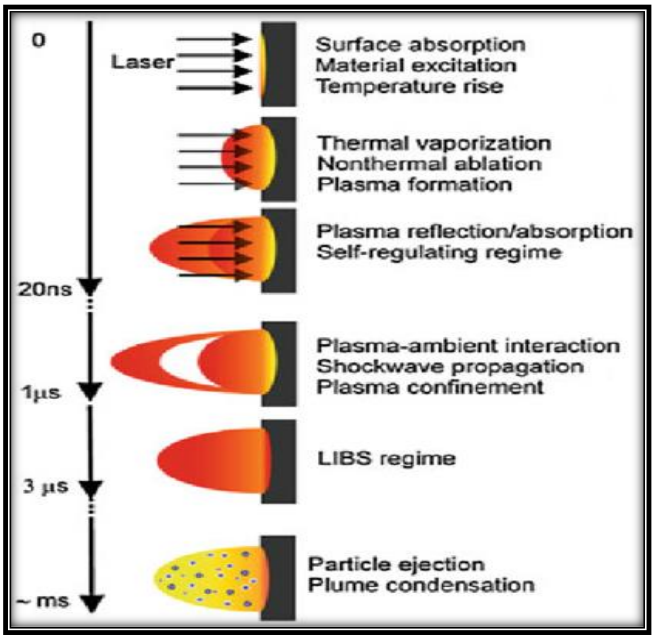

Fig. (1-6) Pulsed laser ablation (PLD) process [33].

When the intensity of the laser beam is close to the threshold of vaporization, the percentage of vacuum atomized materials will have little vaporization intensity at the surface of the target, and when the intensity of the laser beam increases, the percentage of atomized materials will be large, and this generates a layer called [34] Knudsen layer. The increase in the intensity of the laser beam It leads to an increase in the density of atoms and heat in the Knudsen layer, and the degree of its ionization will increase. When the intensity of the laser beam is greater than the threshold limit for the plasma flame, the total ionization of the plasma vapor will occur. In the laser deposition technique, the laser energy is responsible for generating plasma flames for the target material. In this method, we can evaporate and grow thin films of materials or compounds for several layers. The useful range of the wavelengths of the lasers used is often between (200-1100 nm),

because most materials have an absorption coefficient that increases with the decrease in the wavelength of the laser beam, and the materials show strong absorption of light in the spectrum region of ultraviolet and visible rays, and this high absorption of the spectrum Leads to reducing the threshold for the ablation process of the target material. [35]

1.5 Pulse Laser Ablation (PLA)

In which a high-energy pulsed laser is used on a solid target and the nanoparticles are dispersed and deposited on a base-forming thin film. This method was first used in the 1960's and was improved [36].

Since our research relates to the method of laser ablation, it can be defined as the technique by which the laser pulses falling on the target heat up the surface of the material at a very high speed, which leads to the formation of the plasma above the surface of the material, as the energy and the duration of the pulse determine the relative amount of the excised material [37].

The Advantages of Laser Ablation Method are not restricted to the use of a specific type of material and laser skimming can create effective nanostructures of materials, and manufacture of two or more materials at one time, formation of homogeneous and pure alloys and compounds, production of materials at extremely low temperatures, the possibility of chemical modification in the nanocomposite during the skimming process [38].

The most important differences between pulsed laser ablation in vacuum and liquid are: The pressure and temperature of the plasma generated by the laser pulse and projected onto the surface of the metal target in the liquid, which are very large compared to the vacuum or the atmosphere due to the effect of quantum confinement [39], and the rapid

progress and development of preparing nanoparticles for metal alloys as a result of laser ablation in vacuum or gas and expansion by using the manufacture of different Nano powders in the gas phase or in solutions [40],and the volume of plasma decreased in the liquid ocean compared to air and vacuum. This results in the formation of nanoparticles distributed in an average diameter less than the expansion of air or vacuum, due to the loss of the expansion state of the plasma to vaporization of the surrounding liquid and the additional pressure of the plasma from the vapor of the liquid [41].

1.5.1 Pulsed Laser Deposition system Mechanism (PLD)

(PLD) Pulsed Laser Deposition technique which is an important method for depositing G, ZnO films with good stoichiometric size. In particular, there is a strong relationship between the plasma generated by the pulsed laser and pressure inside the chamber [42].

When a laser pulse is directed at a solid target, the process of skimming the material occurs under gaseous conditions. The materials can be assembled or formed into a powder or deposited on a chip. Although some applications require the production of powder with nanostructures such as applications of fuel cells (carbon nanotubes) [43]. However, most applications require nanostructures in the form of thin films. The pulsed laser deposition PLD mechanism is shown in Figure (1-7) [43].

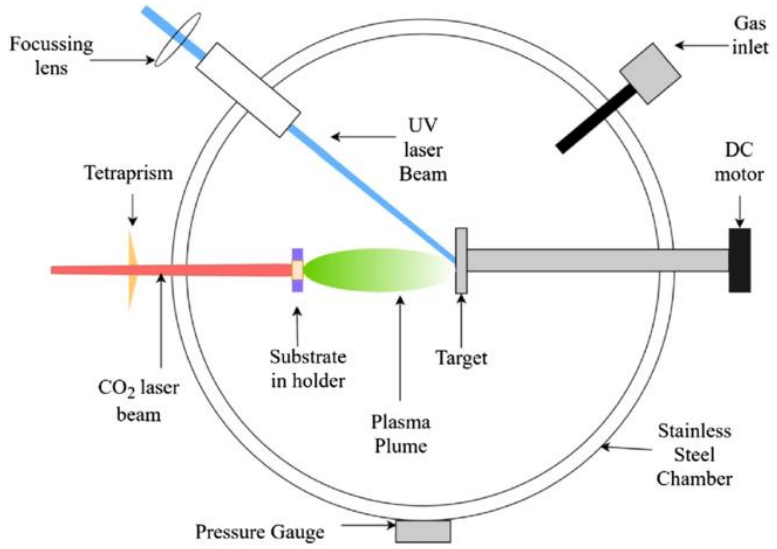

Fig. (1-7) The pulsed laser deposition mechanism [43].

Usually, nanosecond lasers (ns) (KrF, ArF) are used with wavelengths located in the ultraviolet region (192-248 nm) or by the second and third harmonic of the Nd:YAG laser with a wavelength (355-532-1064 nm). These wavelengths are poorly absorbed by the plasma, which reduces from the effect of the plasma on the scraping process. Usually in this technique the laser beam is focused on the surface of a rotating target with an angle of incidence of 45˚, the energy density usually ranges between (108-109 W/cm2)[44].

The laser induces the plasma cloud to expand perpendicular to the surface of the slide that is placed on a rotary basis and at a few centimeters from the target, as the slide holder is kept at room temperature or heated to improve the adhesion of the film to the slide and usually these slides are carried outside in the presence of inert gas (He,Ar). Keeping the gas at a low pressure (0.01-20 Torr) and making sure the chamber is emptied of air before filling it with gas. The target material is placed in a high vacuum chamber, and the atoms and ions atomized from the target will be deposited on the base, where the surface of the base is always parallel to the surface of the target and

between them a certain distance. The pulsed laser deposition mechanism is shown in Figure (1-8)[44].

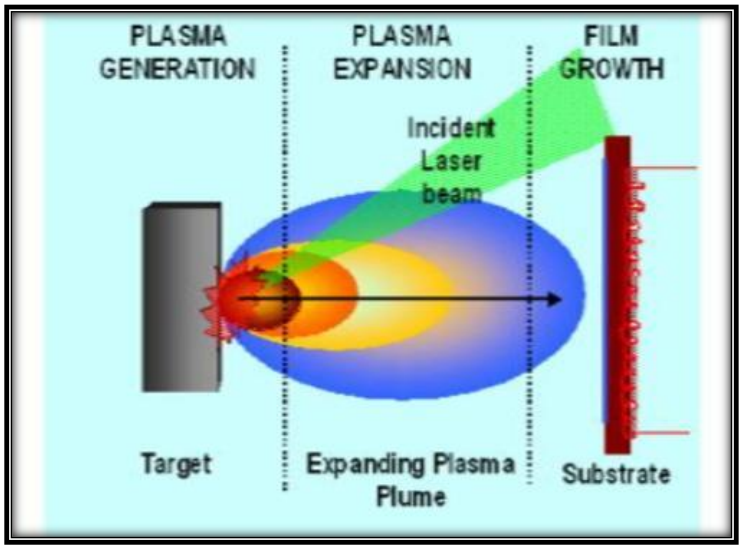

Fig. (1-8) Pulsed laser mechanical deposition [44].

There are conditions through which the sedimentation process takes place:

1- The laser beam falls directly on the surface of the target, and a lens with a suitable focal length is used to focus the laser beam to pass through an optical window that allows the laser beam to pass into the sedimentation chamber, or a glass bell is used to allow the laser beam to pass through.
2- The target material rotates in two levels x, y relative to the laser beam, in order to ensure that the focus of the laser beam remains uniform with each pulse.
3- The sedimentation bases are pre-heated before the sedimentation process to obtain a high adhesion to the film.
4- Sometimes the vacuum chamber of the laser deposition system may be equipped with different gases such as (He, Ar) or others when an interaction between the gas and the membrane material is required during the membrane growth process.

1.6 Silicon Chemical Etching

There are several methods to produce aligned Si NW arrays, such as chemical vapor deposition (CVD), vapor-liquid-solid (VLS) growth, electrochemical etching, but the method most commonly used is metal-assisted chemical etching (MACE). This is due to several reasons: (a) MACE is a simple and low-cost method with the ability to control various parameters of aligned Si NW arrays; (b) MACE method can be used to manufacture aligned Si NW arrays on the large area of silicon substrate with uniform quality; (c) MACE can be performed on the single crystalline silicon substrate and then the crystalline quality of SiNWs fabricated by this method is higher than SiNWs fabricated by the CVD and VLS growth methods [45].

In general, the MACE method involves two steps. The first step is deposition of metal particles on the silicon sample surface, and the second step is etching of the silicon sample coated with the metal particles in an appropriate solution to create aligned SiNW arrays. In literature there were reports on controlling the parameters of SiNWs either by changing the conditions of the metal deposition step, such as metal type, metal deposition time, and metal deposition method, or changing the etching conditions, Among the metals used to assist the etching process to create SiNWs, the most commonly used metal is silver, and silver is usually deposited on Si substrate using aqueous solution of HF/AgNO3 [45].

Effect of AgNO3 concentration on structure of aligned silicon nanowire arrays 345 to the best of our knowledge, so far in literature there were no reports about the dependence of the structure and

properties of aligned SiNW arrays on the AgNO3 concentration in the silver deposition step, so in present work we will address this issue [46].

Nanowires (NWS) are structures with a thickness or diameter restricted to tens of nanometers and an unrestricted length of hundreds of micrometers, i.e. in a length-to-width ratio greater than 1000 times. As expected, it outperforms traditional wires (3 -dimensional). Conductors (such as silver), semiconductors (such as silicon), and insulators (such as silicate) are among them, including inorganic molecular wires, may be used in the near future to connect precise electronic components within a small circuit. As a result, its expected electronic applications are numerous, including nano-molecular biosensors [47], and Figure (1.9). An image obtained using a scanning electron microscope of nanowires [47].

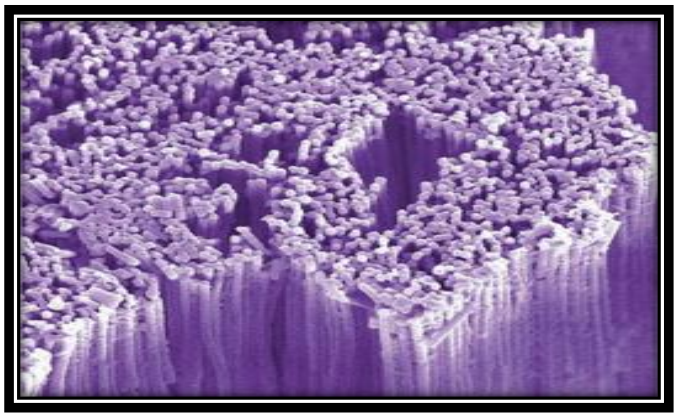

Fig. (1-9) scanning electron microscope of Si nanowires [47].

Aligned silicon nanowire (Si NW) arrays are composed of orderly arranged one dimensional units. Like other one-dimensional materials, aligned Si NW arrays have many unique structural, electrical, optical, and thermoelectric properties. Owing to its large surface to volume ratio and high sensitivity, Si NWs offers unique optoelectronic properties by means of better absorption and electron transport during visible and near-IR

(NIR) rays illumination. The nanowires can be experimentally grown by both chemical and physical techniques [48].

With such special properties, aligned Si NW arrays are promising candidates for applications in many fields, such as advanced electronic devices, bio-medical sensors, optoelectronic devices, and solar cells, and therefore in recent times they have attracted great attention [49].

1.7 Photodetectors

Photodetectors are electronic components that convert a directed beam of light into an electrical signal, such as current or voltage, by amplifying the signal. A detector is any device that produces a measurable physical response to radiated energy from incident photons. Of course, the most common detector is in the eye. The eye, on the other hand, provides a qualitative and subjective response. The majority of detectors are classified as thermal or photodetectors, and the photo-detectors classify as photoconductive, photovoltaic, photoionization, or photodiode [50].

Photodetectors are found in nearly every electronic device that communicates with the outside world or with other devices. Photodetectors are used in many industrial sectors, including telecommunications, food production, transportation, defense, and healthcare [51].

Although the miniaturization of electronic devices such as transistors has enabled higher computational speeds and smaller portable devices, the miniaturization of light sensors has not continued at the same rate due to several physical factors limiting the scaling of these devices .

The development of ultra-thin and flexible photodetectors is particularly difficult with standard semiconductor materials due to the inflexible quality of the materials utilized and the low absorbance at nanoscale thickness [51].

Photodetectors have received considerable research interest due to their numerous scientific applications including optical imaging, optical communication, space communication, environmental monitoring, and military surveillance, etc. Unlike narrow band conventional photodetectors, the broadband photodetectors offer ultraviolet (UV)-visible-infrared (IR) light-based communication utilizing only a single device architecture. In other words, extending the photodetector's detection range would increase their application area [52].

Till date, many efforts are done in the development of single broadband photodetector based on quantum well, quantum dots, organic perovskite, and inorganic nanomembranes. However, these devices suffer from the short detection range and relatively slow response speed. In addition, obtaining stability and high photocurrent responsivity without compromising the response speed in the UV region comparable to visible and IR remains a challenge [52].

1.7.1 PhotoDetector performance parameters

The performance of photodetectors is typically defined by a number of different parameters. These parameters sometimes referred to as (merit numbers), must be specified because manufacturers typically describe the performance of their detectors in these terms. To describe the performance of detectors that respond to a small signal in the presence of noise, merit figures have been developed [53].

1.8 Literature Survey

In (2011) Basant Chitara, et al. [54] Electronic properties of graphene have been studied more extensively than its photonic applications, in spite of its exciting optical properties. Recent results on solar cells, light emitting diodes and photodetectors show its true potential in photonics and optoelectronics. Here, they have explored the use of reduced graphene oxide chemically using simple drop cast method. as a candidate for solution processed ultraviolet photodetectors. UV detection is demonstrated by reduced graphene oxide in terms of time resolved photocurrent as well as photoresponse. The responsivity of the detectors is found to be 0.12 A/W with an external quantum efficiency of 40%. Also they showed demonstrated UV sensing properties of chemically reduced graphene oxide using simple drop cast method. The competition between electron trapping by C¼O groups and electron photogeneration under light radiation is responsible for the observed behavior for an incident wavelength of 360 nm at 1 V.

In (2011) Chitara Basant, et al. [55] IR detection is demonstrated by RGO and GNRs in terms of time-resolved photocurrent and photoresponse. The responsivity and external quantum efficiency of RGO is 4 mA W − 1 and 0.3%, respectively, whereas for GNR these values are significantly higher (ca. 1000 times), being 1 A W − 1 and 80%, respectively, for an incident wavelength of 1550 nm at 2 V. All these results demonstrate that RGO and GNRs, but especially the latter, can be effectively used as high-selectivity, high sensitivity, and high-speed nanometer-scale photodetectors and photoelectronic switches, suggesting a strong impact in many future applications of graphene, including in nanoelectronics.

In (2012) Shiang-Kuo Chang-Jian, et al. [56] Characterizations of photoresponse of a graphene oxide (GO) thin film to a near infrared laser light were studied. Results showed the photocurrent in the GO thin film was cathodic, always flowing in an opposite direction to the initial current generated by the preset bias voltage that shows a fundamental discrepancy from the photocurrent in the reduced graphene oxide thin film. Light illumination on the GO thin film thus results in more free electrons that offset the initial current. By examining GO thin films reduced at different temperatures, the critical temperature for reversing the photocurrent from cathodic to anodic was found around 187◦C. The dynamic photoresponse for the GO thin film was further characterized through the response time constants within the laser on and off durations, denoted as τ on and τ off, respectively. τ on for the GO thin film was comparable to the other carbon-based thin films such as carbon nanotubes and graphenes. τ off was, however, much larger than that of the other's. This discrepancy was attributable to the retardation of exciton recombination rate thanks to the existing oxygen functional groups and defects in the GO thin films.

In (2013) Wenhao Guo, et al. [57] they demonstrate an efficient charge transfer between ZnO quantum dots (QDs) and a single layer graphene. Graphene was exfoliated from graphite by mechanical cleavage onto degenerately doped Si substrates with 300 nm SiO2. ZnO QDs were prepared according to the method of Pacholski. They fabricate a graphene based ultraviolet (UV) sensitive device with ZnO QDs on top of the graphene layer, and find that the electrical response of the device to UV light is largely enhanced due to the charge transfer. They show that the oxygen molecules play a vital role in the charge transfer process, by

being adsorbed on or desorbed off the QDs surface. With a gain of as high as 10^7, this new hybrid nano structure may lead to the improvements for design of the photoelectric devices and the realization of high performance graphene-based UV sensors and detectors.

In (2014) Sin Ki Lai, et al. [58] Graphene oxide (GO) was synthesized by a hydrothermal method using glucose solution as the sole reagent. The wavelength-dependent photoresponse of GO was investigated by fabricating metal– GO–metal photodetectors. The devices demonstrated a broadband photoresponse from 290 to 1610 nm covering deep ultraviolet (UV) to near-infrared (NIR), which is the broadest spectral range yet demonstrated on GO. The response times of the photodetectors in the UV and visible range are about 100 ms, which are at least one order of magnitude faster than photodetectors based solely on GO reported previously. The responsivity of the photodetector can be as high as 23.6 mA W^{-1} in the visible range. The wavelength-dependent photoresponse is closely related to the absorption characteristics of GO. Potential for a self-powered GO based photodetector is first demonstrated, and the device shows a prominent photoresponse at zero bias. The GO based photodetectors pave the way for developing low-cost, broadband, self-powered as well as spectrally tuneable photodetectors.

In (2015) Hao Liu, et al. [59] a ZnO nanowire array/ reduced graphene oxide film hybrid nanostructure was realized, which was realized by the electrophoretic deposition of rGO on top of ZnO NW arrays, and the photovoltaic responses from the visible to the near-infrared range were investigated. Compared with the pure ZnO nanowire array and rGO thin film, the hybrid composite exhibited a fast and greatly enhanced

broadband photovoltaic response that resulted from the formation of interfacial Schottky junctions between ZnO and rGO. They believe that this strategy could be universally applied to a variety of rGO-incorporated nanostructured systems for photodetector applications.

In (2015) Dali Shao, et al. [60] the performance of graphene field-effect transistors is limited by the drastically reduced carrier mobility of graphene on silicon dioxide (SiO_2) substrates. Here they demonstrate an ultrasensitive ultraviolet (UV) phototransistor featuring an organic self-assembled monolayer (SAM) sandwiched between an inorganic ZnO quantum dots decorated graphene channel and a conventional SiO_2/Si substrate. Remarkably, the room-temperature mobility of the chemical-vapor deposition grown graphene channel on the SAM is an order-of magnitude higher than on SiO_2, thereby drastically reducing electron transit-time in the channel. The resulting recirculation of electrons (in the graphene channel) within the lifetime of the photogenerated holes (in the ZnO) increases the photo responsivity and gain of the transistor to $\sim 10^8$ A/W and $\sim 3 \times 10^9$, respectively with a UV to visible rejection ratio of $\sim 10^3$. Our UV photodetector device manufacturing is also compatible with current semiconductor processing, and suitable for large volume production.

In (2015) Vinh Quang Dang , et al. [61] Ultraviolet (UV) photo detectors based on ZnO nanostructure/graphene (Gr) hybrid-channel field-effect transistors (FETs) are investigated under illumination at various incident photon intensities and wavelengths. The time-dependent behaviors of hybrid-channel FETs reveal a high sensitivity and selectivity toward the near-UV region at the wavelength of 365 nm. The devices can operate at

low voltage and show excellent selectivity, high responsivity (R_I), and high photoconductive gain (G). The change in the transfer characteristics of hybrid-channel FETs under UV light illumination allows to detect both photo voltage and photocurrent. The shift of the Dirac point (V_{Dirac}) observed during UV exposure leads to a clearer explanation of the response mechanism and carrier transport properties of Gr, and this phenomenon permits the calculation of electron concentration per UV power density transferred from ZnO nano rods and ZnO nanoparticles to Gr, which is 9×10^{10} and 4×10^{10} per mW, respectively. The maximum values of R_I and G infer from the fitted curves of R_I and G versus UV intensity are 3×10^5 A W^{-1} and 10^6, respectively. Therefore, the hybrid-channel FETs studied herein can be used as UV sensing devices with high performance and low power consumption, opening up new opportunities for future optoelectronic devices.

In (2016) Ching-Cheng Cheng, et al. [62] a self-powered photodetector with ultrahigh sensitivity, fast photoresponse, and wide spectral detectivity covering from 1000 nm to 400 nm based on graphene/ZnO/Si triple junctions has been designed, fabricated, and demonstrated. In this device, graphene serves as a transparent electrode as well as an efficient collection layer for photogenerated carriers due to its excellent tunability of Fermi energy. The ZnO layer acts as an antireflection layer to trap the incident light and enhance the light absorption. Furthermore, the insertion of the ZnO layer in between graphene and Si layers can create build-in electric field at both graphene/ZnO and ZnO/Si interfaces, which can greatly enhance the charge separation of photogenerated electron and hole pairs. As a result, the sensitivity and response time can be significantly improved. It is believed that our methodology for achieving a high-performance self-powered photodetector based on an appropriate

design of band alignment and optical parameters can be implemented to many other material systems, which can be used to generate unique optoelectronic devices for practical applications.

In (2016) Yoshikazu Ito, et al. [63] Preparation of Nanoporous Graphene by CVD, The photoconductor devices were fabricated by attaching np-GO films on SiO 2 /Si substrates. Reduced graphene oxide (RGO) is an important graphene derivative for applications in photonics and optoelectronics because of the band gap created by chemical oxidation. However, most RGO materials made by chemically exfoliated graphite oxide are 2D flakes. Their optoelectronic performance deteriorates significantly as a result of weak light-matter interaction and poor electrical contact between stacking flakes. Here we report a bicontinuous 3D nanoporous RGO (3D np-RGO) with high optoelectronic performance for highly sensitive photodetectors. 3D np-RGO demonstrates an over 40 times higher light absorption than monolayer graphene materials and at least two orders of magnitude higher electron mobility than conventional RGO from discrete RGO flakes. The np-RGO with an optimal reduction state shows ultrahigh photoresponse of $3.10*10^4$ A W^{-1} at room temperature, approximately four orders of magnitude higher than graphene and other graphene derivatives at similar levels of light intensity radiations, and the excellent external quantum efficiency of $1.04*10^7$ % better than commercial silicon photodetector. The ultrahigh capability of conversing photons to photocurrent originates from strongly enhanced light absorption, facilitated photocarrier transport, and tunable oxygen on defects and reduction states in the 3D interconnected bicontinuous RGO network.

In (2017) Hua Yang, et al. [64] Compared with mechanically exfoliated and chemical vapor deposited graphene, reduced graphene oxide (RGO)

possesses unique advantages such as a wet process synthesis, high yield, and the ability to assemble large-area thin films on various substrates. However, RGO usually is not recommended for advanced devices owing to its poor electrical conductivity. They report a new method to prepare highly conductive free-standing RGO thin films. The as-prepared RGO thin film possesses the highest conductivity of 87100 S m-1, the second-lowest sheet resistance of 21.2 sq-1, and medium-level mobility of 16.7 cm2×V-1×s-1 among all of the reported RGO films. To demonstrate the application potential of the free-standing RGO thin films in photoelectric devices, a fully suspended RGO photodetector is constructed using the free-standing RGO thin film, which exhibits the fastest (ca.100 ms) and broadest (from the ultraviolet to terahertz spectral range) photo response among all of the RGO film photodetectors that have been reported. The response speed is even comparable with those of CVD-grown graphene photodetectors and mechanically exfoliated graphene photodetectors. These results pave the way toward high-conductivity RGO thin films by a wet process assembly, thus facilitating applications of RGO in advanced electronic, optoelectronic, and sensing devices.

In (2020) Yu Liu, et al. [65] prepared and made heterojunction photoelectric devices based ZnO nanowires were fabricated on p-Si substrate with and without single-layer graphene as insert layer. ZnO nanowires and graphene were prepared by hydrothermal method and chemical vapor deposition respectively. The effect of insert layer on the morphology of ZnO nanowires was very weak as can be seen from scanning electron microscope and X-ray diffraction. Raman scattering showed that the graphene prepared was a single layer structure. The ultraviolet detection performance of photodetectors with single graphene insert layer was much better than that of photodetectors without single

graphene insert layer. The ultraviolet irradiation sensitivity of photodetectors with single graphene insert layer was up to 1071 which was improved 7 times than that of photodetectors without single graphene insert layer. Moreover, photodetectors with single graphene insert layer had faster response time (1.02 s) and recovery time (0.34 s).

In (2020) Shonak Bansal, et al. [66] This paper presents three self-powered photodetectors namely, p+-bilayer graphene (BLG)/n+- ZnO nanowires (NWs), p+-BLG/n+-Si NWs/p–-Si and p+-BLG/n+-ZnO NWs/p– -Si. The Silvaco Atlas TCAD software is utilized to characterize the optoelectronic properties of all the devices and is validated by analytical modeling. The proposed dual-junction photodetectors cover broadband spectral response varying from ultraviolet to near-infrared wavelengths. The dual-heterojunction broadband photodetector exhibits photocurrent switching with the rise and fall time of 1.48 and 1.27 ns, respectively. At –0.5 V bias, the highest external quantum efficiency, photocurrent responsivity, specific detectivity, and the lowest noise equivalent power of 71%, 0.28 A/W, 4.2×1012 cmHz1/2/W, and 2.59×10–17 W, respectively, are found for the dual-heterojunction device with a wavelength of 480 nm at 300 K. The proposed nanowires based photodetectors offer great potential to be utilized as next-generation optoelectronic devices.

In (2021) Hasmat Mondal ,et al. [67] A significantly improved silicon nanowire (SiNW)-based broadband photodetector is obtained in this work using the core–shell structure of Si NWs with hydrothermally processed nitrogen-doped graphene quantum dots (N-GQDs). The performance of the photodetector device is enhanced significantly by enlarging the

effective surface area of the Si NW/N-GQD heterostructures by controlled KOH etching of Si NWs. In combination with Si NWs, low-cost hydrothermal processed N-GQDs are used as a light absorber in the UV region and also as an emitter in the visible region which is reabsorbed by the SiNWs to enhance the device performance. Significantly improved external quantum efficiency (EQE) exceeding 150% in the near IR and ∼500% at 460 nm wavelength in the visible region.

In (2022) Pooja Singh ,et al. [68] They report a new class of infrared (IR) photodetectors in near IR region comprising of zinc oxide (ZnO) nanoparticles − silicon nanowire (Si NWs) hybrid nanostructure. Si NWs on p-Si (1 1 1) substrate were synthesized by metal-assisted chemical etching (MACE) whereas ZnO nanoparticles were prepared using green synthesis technique accompanied by the deposition of these ZnO nanoparticles over Si NWs. The NIR photo sensing response of ZnO/Si NWs was measured by using the radiation wavelength of 1064 nm at room temperature wherein it showed a large photoresponse under this illumination. The photo-resistive response of the ZnO/Si NWs hybrid nanostructure was observed to be very fast (3 s) wherein ∼ a 12% decrease in the initial resistance was observed under NIR illumination. As they turned off the IR source, the sensor reached its initial state within 3 seconds.

In (2023) Muhammad Aamir lqbal ,et al. [69] an attempt was made to successfully deposit graphene on a silicon substrate. This results in the formation of a Schottky junction, which could extend the operation window of the graphene/silicon hybrid device to the near-infrared (NIR) region. Furthermore, since photodetectors built with Van der Waal heterostructures successfully extend the lifespan of dynamic charge

carriers with improved the transportation range and speed of charge separation for effective photodetection, the technical development of optoelectronic devices has been greatly accelerated. Recent developments in graphene-silicon junction-based devices, their photodetection effectiveness, and active factors that can be used in a variety of applications are outlined, including optical synaptic systems, optical spectrometers, plasmonic devices, optical waveguides, and ultrafast photodetectors. Moreover, the shortcomings of the present optoelectronic devices are also concisely reviewed, along with the viable solutions offered by this new device and its application in next-generation devices.

1.9 The Aims of work

The purposes of this project are :

1- Prepare SiO NWS, or Prepare Si NWS depend on the results of metal-assisted chemical etching.

2- Prepare SiO NWS/G, SiO NWS/ZnO, and SiO NWS/G/ZnO nanocomposite by using the pulse laser deposition method.

3- Study the structural, morphological, optical, and electrical properties of prepared films to find the optimization for prepared films.

4- Applications (Photodetector and solar cell).

2.1 Introduction

This chapter gives a general description of PLD technique and the theoretical part containing the characteristics. Structural, optical, electrical, optoelectronic, and the main properties which make Silicon nanowire SiO NWS/graphene G/Zinc Oxide ZnO metals nanocomposite a good candidate for certain application. The study of structural and morphological properties was performed with X-ray diffraction (XRD), atomic force microscope (AFM), and scanning electron microscope (SEM), X-ray photoelectron spectroscopy (XPS) or Electron Spectroscopy for Chemical Analysis (ESCA), Raman Spectroscopy, Optical properties of nanocomposite (reflectivity and energy gab), electrical properties (Hall Effect) (resistivity (ρ), mobility (μ)), and photodetector properties (responsivity (R), detectivity (D) and quantum efficiency (QE),Solar cell.

2.2 Pulsed Laser Deposition (PLD)

The Q-switching Nd: YAG pulsed laser beam is focused via a window by a lens with a focal length of 30 cm as shown in figure (2-2). The beam of laser is passed into the chamber through a window made of quartz material. The chamber has more than one quartz windows, laser beam is admitted into one, whilst the others are employed in-situ plasma diagnostics and growth monitoring. The laser radiation is incident onto the surface of target with 45° angle. The substrate is positioned in target front (face to face) so that its surface is parallel to the targets. Between the substrate and the target, a sufficient distance is maintained such that the incoming laser beam is not blocked by the substrate holding adjustment of the deposition components on a regular basis in order to get higher quality films via the process, such as heating the substrate, rotating the target, and positioning the substrate in respect to the target [69].

2.2.1 Dynamic and Plasma Engineering

One benefit of pulse laser deposition mechanism is that it is possible to fill up the vacuum chamber with or without inert gas that reacts with the plume of plasma before it reaches to the substrate .It can be seen in figure (2-1). When the chamber pressure increases, it changes the spatial distribution of the plasma plume and reduces the ions number reaching to the substrate. Therefore, the atoms kinetic energy in the plasma plume decreases as a consequence of collision with atoms of gas [70]. This will change the pattern of film growth, the crystal structure and the film deposition direction.

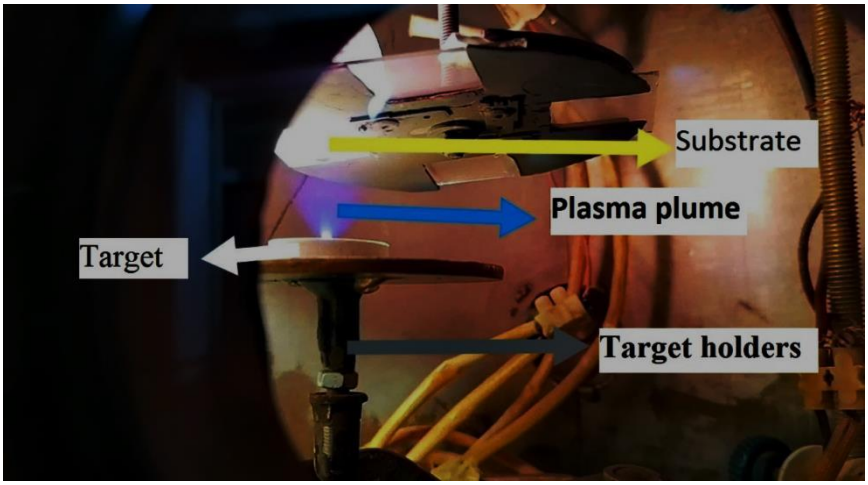

Fig. (2-1) Plasma plume generated by laser incident [70].

2.2.2 Deposition Chamber

The deposition chamber is cylindrical in form. The chamber geometry may be created totally freely since the PLD technique does not require ultra-high vacuum. Pumping system, pressure monitoring, gas inlets, substrate, target, laser beam, and view components are often included in the chamber.

During the deposition process, the ablation target has been held in a vertical position by the target holder. It is necessary rotated during the deposition process, while the laser reaction spot is remained stationary. This arrangement

provides an advantages, where the surface area of target may be used more effectively and successfully for a longer period without creating a hole [71].

2.2.3 Vacuum System

The deposition chamber has been fixed onto steel flange including a groove with O-ring for vacuum sealing and feed-through in the base for electrical connections (the substrate heater and control the stepper motor) and the chamber evacuated using rotary pump connecting directly to the chamber using steel flexible tubes to get a vacuum more than 10^{-2} mbar and by using Pirani gauge, monitoring the pressure inside the chamber. The rotary pump is a type (GALILEO TP model 949-9325S006) and it is the main part of the vacuum and diffusion pump from type (DIFFUSION PUMP DPF-4Z) which used to get vacuum of 10^{-6} mbar in chamber. For depositing all films and quartz substrates, has been used a Nd-YAG laser with deposition temperatures of (300) ^{o}C [72].

2.3 Interferometric Method for the Thickness Measurements

For the determination of the thickness of the films deposited, an interferometric Fizeau was used. In Fig. (2-2a), the experimental setup for observing Fizeau fringes is shown schematically, and in Fig. (2-2b) the Fizeau pattern is shown. The thickness of the film is calculated by the optical interferometer process. The approach is based on the interference of the reflection of the light beam from the thin film surface and the bottom of the substrate. It uses He-Ne Laser (600 nm). To calculate the thin film thickness, the following equation [73]:

$$t_t = \frac{\Delta X}{X} \cdot \frac{\lambda}{2} \qquad (2\text{-}1)$$

Where X is the spacing of the fringes, ΔX is the displacement and λ is the laser light wavelength.

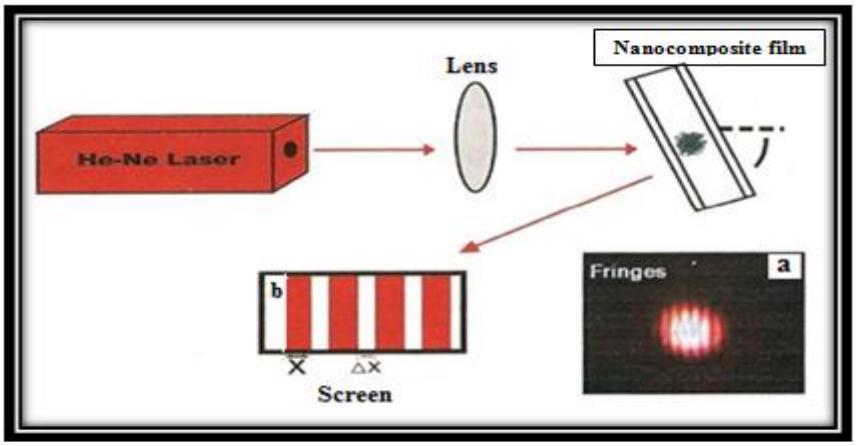

Fig. (2-2) (a, b) Experimental arrangement for observing Fizeau fringes [73].

2.4 Structural and Morphological Properties:

The structural properties are important tool for study the thin films crystallographic structure.

2.4.1 X-ray Diffraction (XRD)

One of the most important methods for qualitative study of crystalline compounds is X-ray diffraction (XRD). XRD is a commonly used experimental method for deciding crystal lattice parameters and desired orientation. The XRD mechanism is simple. If the Bragg's law is satisfied, constructive diffractions (or interference) from parallel planes of atoms with inter-planar spacing (d) occur when a monochromatic X-ray beam is incident onto a crystal sample [74-75].

$$2d \sin\theta = n\lambda \quad \ldots\ldots\ldots\ldots\ldots\ldots\ldots\ldots\ldots\ldots\ldots\ldots\ldots\ldots \quad (2.2)$$

Where:

n, θ and λ are integer that indicates the order of the reflection, Bragg diffraction angle of the XRD peak (degree) and the wavelength of the X-ray beam.

If the wavelength of the X-ray beam is known by measuring the Bragg angle (θ), the interplanar distance (d) can be obtained. These specific directions appear as spots on the diffraction pattern which called reflections, as shown in figure (2-3).

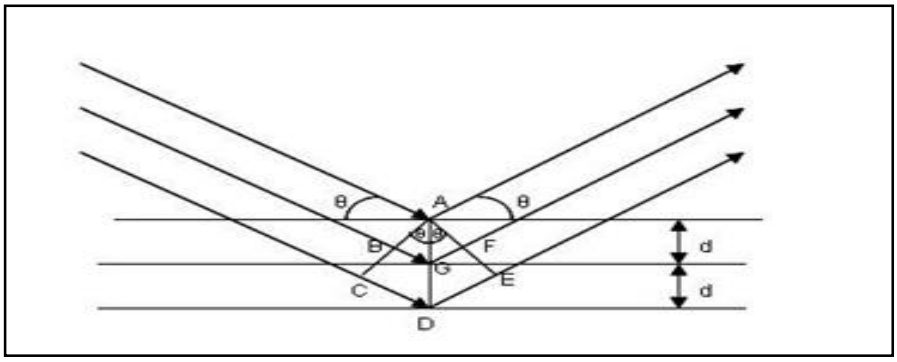

Fig.(2-3) X-rays diffraction[75].

Parameters Calculation

XRD is commonly used to determine various parameters and to elucidate the investigations of deposited films.

Average Crystallite Size (D)

The single line method is one of the many line profile analysis methods that use a Voigt function to calculate the average grain size (D) and the size-strain parameters (micro-strains and crystallite sizes)[76], which can be calculated using the Scherer's eq.[77]:

$$D = \frac{0.94\,\lambda}{\text{Ɓ}\cos\theta} \qquad \ldots\ldots\ldots\ldots\ldots\ldots\ldots\ldots\ldots\ldots\ldots\ldots\ldots\ldots \quad (2.3)$$

Where: Ɓ is (FWHM) full width at half maximum by (radian).

2.4.2 Atomic Force Microscope (AFM)

Atomic force microscopy (AFM) is a widely used technique for quantifying surface topography and investigating the surface microstructure. The picture of a

thin film surface may be zoomed in using current and extremely sophisticated technological methods in the aforementioned approach. Its benefits include a large analysis capacity of up to (5×10^2 - 10^8) and the ability to operate it under ordinary barometric pressure without the need for a high vacuum. As a result of the varying conditions and film processing process sand impurities used in the films, a strong distinction can be seen with the film surfaces under inspection. The end probe of the microscope has an arm (Cantilever) with a sharp tip (Tip) that is used to scan the sample surface. This arm is generally constructed of silicon nitride (Si_3N_4) and has a few nanometers in radius[78] . It's usually used to determine the surface area of insulators, conductive materials, and semiconductors. Atomic force microscopy was used to determine the average grain size and surface topography of the samples on an atomic scale. It also provides us with extremely detailed statistics on roughness and grain size[79].

As The average particle size is an important parameter to describe the size of the nanoparticles in the sample. It is defined as the arithmetic average of the particle sizes in the sample [80]. The RMS value is a measure of the deviation of the particle size distribution from the average particle size. It is calculated by taking the square root of the sum of the squared differences between the particle sizes and the average size, divided by the number of particles [80]. The Ra value provides information about the surface roughness of the nanoparticles. It is calculated as the arithmetic average of the absolute values of surface irregularities [81].

2.4.3 Scanning Electron Microscope (SEM)

A significant method for investigating the surface and morphology of nanostructures is scanning electron microscopy (SEM). By using it, we can estimate the nanostructure’s diameter, weight, thickness, density, shape and orientation [82]. To emit electrons by heating, an electron gun made of tungsten

or LaB-6 filament is used and these emitted electrons are guided and concentrated on the sample by the use of an anode and various electromagnetic lenses between the electron gun and the sample. After entering the sample, these predicted electrons expel secondary and back-scattered electrons. These secondary and back scattered electrons expelled from the sample are detected by detectors and these detectors pass these electrons detected into the electronic signal sent to the image display device [83].

2.4.4 X-ray photoelectron spectroscopy XPS or ESCA

X-ray photoelectron spectroscopy (XPS), also known as electron spectroscopy for chemical analysis (ESCA), is a surface analysis technique that provides information about the elemental composition and chemical state of a material [84].

In the case of the combination of silicon nanowires, graphene, and zinc oxide nanoparticles, XPS can be used to determine the chemical composition of the surface of the material. The technique works by irradiating the sample with X-rays, which causes the emission of electrons from the surface of the material. The energy and intensity of these emitted electrons are then measured to determine the chemical composition of the surface [85], as in Fig.(2-4).

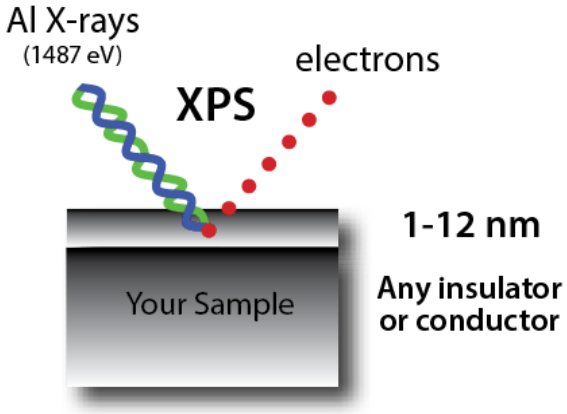

Fig. (2-4) The X-ray photoelectron spectroscopy (XPS).

In particular, XPS can be used to determine the chemical states of silicon, carbon, oxygen, and zinc on the surface of the material. For example, the binding energy of the silicon 2p, carbon 1s, oxygen 1s, and zinc 2p electrons can be measured to determine the oxidation states of these elements and the chemical environment in which they are located [85].

Overall, XPS is a powerful tool for the chemical analysis of surfaces and can provide valuable information about the composition and chemical state of materials such as silicon nanowire-graphene-zinc oxide nanoparticles.

2.4.5 Raman Spectroscopy

Raman spectroscopy is a technique that uses laser light to probe the vibrational modes of molecules in a material. In the case of silicon nanowire-graphene-zinc oxide nanoparticles, Raman spectroscopy can provide information about the structural and electronic properties of the material [86].

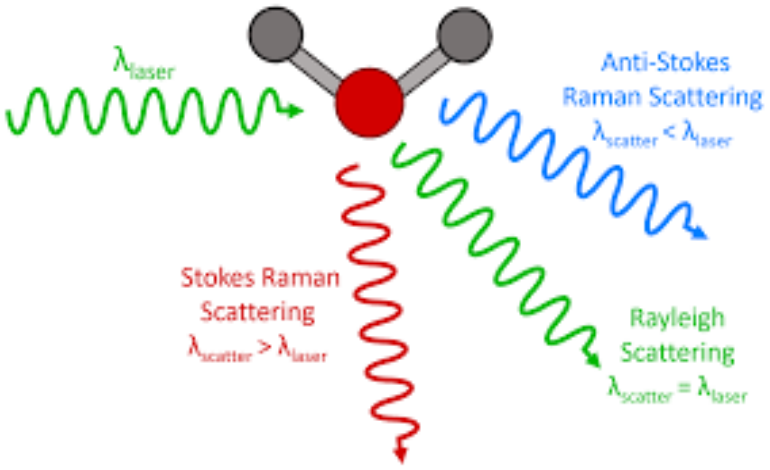

Fig. (2-5) Raman scattering and Rayleigh scattering

When a laser is directed onto the sample, the photons interact with the molecules in the material and cause them to vibrate. The scattered light is then analyzed to determine the vibrational frequency and intensity of the molecular

vibrations. The frequency and intensity of these vibrational modes are characteristic of the chemical bonds and crystal structure of the material [87].

In the case of silicon nanowire-graphene-zinc oxide nanoparticles, Raman spectroscopy can be used to determine the quality and structural integrity of the graphene layer, as well as the presence of any defects or impurities in the material [88]. The Raman spectra of graphene typically exhibit two prominent peaks, known as the G and 2D bands, which correspond to the stretching and bending of carbon-carbon bonds in the graphene lattice. The intensity ratio of these two peaks can be used to determine the number of graphene layers and the degree of disorder in the graphene [89].

Raman spectroscopy can also be used to probe the vibrational modes of the silicon nanowire and zinc oxide nanoparticles. The Raman spectra of these materials typically exhibit peaks that correspond to the phonon modes of the crystal lattice, which can provide information about the crystal structure and quality of the material [90].

Overall, Raman spectroscopy is a powerful tool for the characterization of silicon nanowire-graphene-zinc oxide nanoparticles, as it can provide information about the structural and electronic properties of the material at the nanoscale level.

2.5 Optical Properties

2.5.1 Diffused Reflectance UV-Vis Spectrometer(DRS):

The Kubelka-Munk theory is a well-known method for determining the optical properties of materials, specifically their absorption and scattering coefficients, from reflectance or transmittance measurements. This theory assumes that the sample is a homogeneous, isotropic and opaque medium, and that the scattering

and absorption properties of the material are independent of the direction of the incident light [91].

In the case of measuring the energy gap of (SiO nanowires / graphene, ZnO NPs) using diffuse reflectance spectra, the Kubelka-Munk theory can be applied to determine the absorption coefficient of the material. The energy gap, also known as the bandgap, is the minimum energy required to excite an electron from the valence band to the conduction band. This energy is typically determined from the material's absorption spectrum, which shows the amount of light absorbed by the material at different wavelengths. The energy gap can then be determined from the absorption coefficient using the Tauc plot method. Note that the Tauc plot method assumes that the material has a direct energy gap. as in Kubelka-Munk equation following (2.4) [91].

F=(1-R∞)^2/2R∞ (direct) . ……...(2.4)

$\alpha h\nu = C_1(h\nu - Eg)^{1/2}$

$\alpha = F(R\infty)$

$[F(R\infty)\ h\nu]^2 = C_2(h\nu - Eg)$

F(R)=(FR*hv)^0.5 (indirect) . ……..….(2.5)

$h\nu = 1240/\lambda$

where R∞ = sample reflection coefficient; λ= absorption wavelength.

In the Kubelka-Munk theory, the absorption coefficient is related to the diffuse reflectance by a mathematical expression, which can be used to determine the energy gap. The energy gap can be calculated by extrapolating the linear portion of the absorption spectrum to the energy axis, which corresponds to the energy required to excite an electron from the valence band to the conduction band [92].

It is worth noting that the accuracy of the energy gap measurement depends on several factors, including the quality of the sample preparation, the accuracy of the reflectance measurements, and the assumptions made in the Kubelka-Munk theory [92]. Therefore, it is important to carefully consider these factors when interpreting the results obtained from the Kubelka-Munk analysis.

Note that the Tauc plot method assumes that the material has a direct energy gap. For materials with an indirect energy gap, additional corrections may be necessary.

To correct for this, two methods are commonly used:

1-The Cody method: This method involves plotting (αhν)^2 versus hν, where α is the absorption coefficient and hν is the energy of the incident photon. The energy gap can then be determined from the point of maximum curvature in the plot [93]. This method assumes that the absorption coefficient can be described by a function of the form

α = A(hν - Eg)^n, where A, n, and Eg are constants.

2- The Davis and Mott method: This method involves plotting (αhν)^2 versus hν^2. The energy gap can then be determined from the point where the plot intersects the x-axis [94]. This method assumes that the absorption coefficient can be described by a function of the form

α = (hν - Eg)^2.

Both methods have their limitations and should be used with caution. It's important to note that the accuracy of the energy gap determination for materials with an indirect energy gap can be affected by factors such as sample preparation, instrument calibration, and measurement conditions. Therefore, it's recommended to use multiple methods and verify the results with other techniques to ensure the accuracy of the measurement.

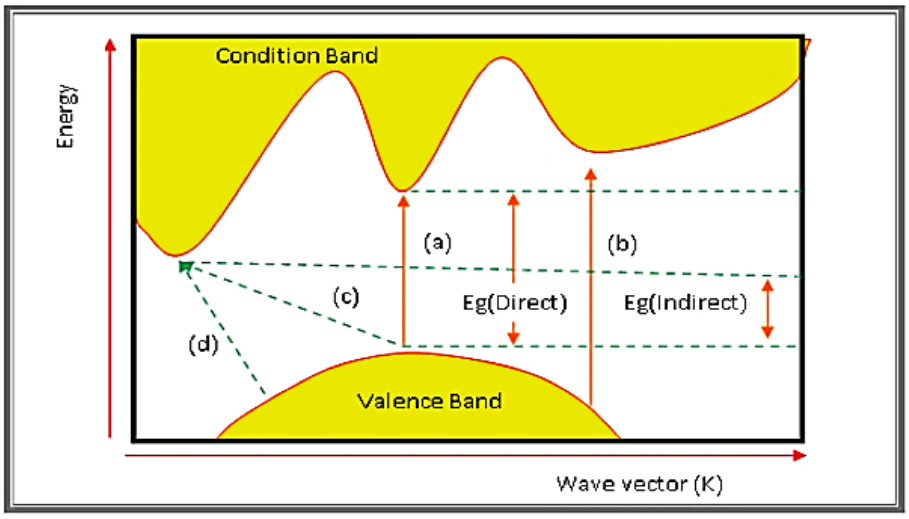

Fig. (2-6) the optical transitions [95].

(a) Allowed direct, (b) Forbidden direct, (c) Allowed indirect, (d) Forbidden indirect

2.8 Electrical properties:

Consideration of the electrical properties of materials is often important when materials selection and processing decisions are being made during the design of a component or structure. This section will discuss some electrical properties of thin films such as the Hall Effect [96, 97].

2.8.1 Hall Effect

The Hall effect is used in common practice to measure certain properties of semiconductors: namely, the carrier concentration, the mobility, and the type (n or p).It is an important analytical tool since a simple conductance measurement can only give the product of concentration and mobility. Figure (2.7) shows when a magnetic field is applied at right angles to a current flow(I).An electric field (E_H) is generated which is mutually perpendicular to the current and the magnetic field, and is directly proportional to the product of the current density(J) and the magnetic inductions [96] :

$$E_H = R_H JB \qquad (2\text{-}19)$$

where R_H is the Hall coefficient and $J = \frac{I}{A'}$ where $A^{/}$ is the cross section area and B is the magnetic field. The generated electric field (E_H) is called Hall field which is related to the Hall voltage (V_H) by the relation [97] :

$$V_H = E_H W \qquad (2\text{-}20)$$

where *W* is the distance between the two electrode**s**.

By scheming Hall voltage as a function of current, Hall coefficient can be determined by the relation [97]:

$$R_H = \frac{V_H}{I} . \frac{t}{B} \qquad (2\text{-}21)$$

where *t* is the film thickness.

Carrier's concentration can be determined by using the relation [97]:

$$n = \frac{-1}{q\ R_H} \quad \text{for electrons} \qquad (2\text{-}20)$$

or

$$p = \frac{+1}{q\ .\ R_H} \quad \text{for holes} \qquad (2\text{-}21)$$

From Hall measurements, the Hall mobility can be obtained according to the relation [98]:

$$\mu_H = R_H \sigma_{R.T} \qquad (2\text{-}22)$$

where σ_{RT} is the conductivity at room temperature.

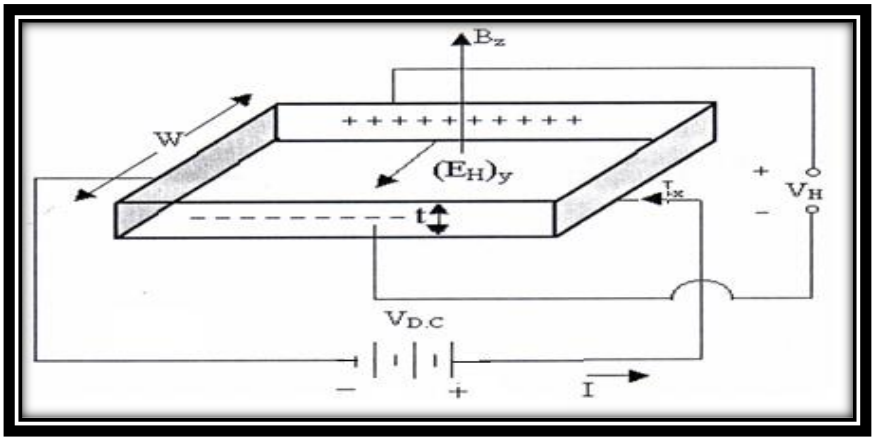

Fig. (2-7) Hall Effect measurement circuit [94].

1. Resistivity (ρ)

The conductivity of semiconducting material, in addition to being dependent on electron and/or hole concentration, is also a function of the charge carriers mobilities. The resistivity of any conductor (film) can be calculated from the relation [99]:

$$\rho = R_e \times A^* / L \quad \Omega.cm \qquad (2\text{-}23)$$

where A* is the cross section area (film sheet) and L is the conductor length (inter electrode spacing). The resistivity of the films related to the electric field and the current passing through the film is [100]:

$$\rho = E / J \qquad (2\text{-}24)$$

where (E) is the electric field equals to (V/d), (V) is the applied voltage, (d) is the electrode spacing distance, and (J) is the current density equals to (I/A*).It depends on the resistivity (or conductivity), that is on the carrier concentration (electrons or holes). It is affected by so many parameters or conditions mainly the doping, temperature and deposition technique [100].

2. Mobility (μ)

Mobility is an important parameter for carrier transport because it refer to how strongly the motion of an electron is influenced by an applied electric field [101]:

$$\upsilon_n = -\mu_n \ E \qquad (2\text{-}25)$$

Analogous expression can be written for electrons in the conduction band and holes in the valence band respectively [101]:

$$\upsilon_p = \mu_p E \qquad (2\text{-}26)$$

where (μ_n) and(μ_p)are the electrons and holes mobility respectively, (E) is the electric field, (ν_n)is the electron drift speed and(ν_p)is the hole drift speed .The negative sign is removed in eq.(2.25) because the holes drift in the same direction as the electric field [101].

2.9 The properties' of the photodetector

Photonic detector convert photons directly into free current carriers, when light falls on the detector the photons exciting the electrons to higher energy levels lead to forming electrical charge carriers (e or h) that remain inside the detector material. The incident photon must has energy equal or greater than band gap energy to excite valence electrons, the longest wavelength that can be absorbing is specific by cut-off wavelength (λ_c) given by Equation [102]:

$$\lambda_0 = \frac{1.24}{E_g(eV)} \dots\dots\dots\dots\dots\dots\dots\dots\dots\dots (2.27)$$

These reagents are characterized by having a spectral response within a specified range of wavelengths depending on the type of reagent and have a short response time. It is an important parameter of the photodetector that was calculated:

1- The Responsivity

It is the ratio between the output quantity current or voltage from the photodetector to the power of the incident radiation. As in the relationship [1 02] [103]:

$$R_\lambda = \frac{I_{ph}}{P_{in}} \ (A/W) \qquad \text{or} \ \frac{V_{photovoltge}}{P_{input}} \ (V/W) \dots\dots\dots\dots\dots\dots (2.28)$$

Where I_{ph} photogenerated current, P_{in} input light power.

2- Quantum Efficiency

It is the ratio between the number of electron-hole pairs (EHP'S) generated to the total number of absorbed photons [102]. The quantum efficiency is essentially another way of expressing the effectiveness of the incident optical energy for producing an output of electrical current, it may be related to the responsivity by the equation [102][103]:

$$\eta_{quantum} = R_\lambda \frac{1.24}{\lambda_{(\mu m)}} \text{ x } 100\% \ldots\ldots\ldots\ldots\ldots\ldots\ldots\ldots (2.29)$$

3- Detectivity

The term detectivity replaced by specific detectivity (D*) used to compare types of reagents and is known by relationship [103][104]:

$$D^* = R_\lambda \frac{\sqrt{A.\Delta f}}{I_n} \qquad cm.HZ^{1/2}.W^{-1} \quad \ldots\ldots\ldots\ldots\ldots\ldots (2.30)$$

$$I_n = (2qI_d\Delta f)^{1/2} \ldots\ldots\ldots\ldots\ldots (2.31)$$

Where

I_n : Total noise current

Δf : the noise-bandwidth

A: active area of the photodetector

I_d:dark current

q: electron charge.

2.10 Heterojunctions

The heterojunction is defined as a connection between two semiconductor materials that differ in the energy gap, electronic affinity, dielectric constant, and work function as well as a mismatch in the lattice constant for the two materials, while the homo junction consists of the connection of two semiconductor materials of the same type, i.e. identical in the energy gap,

electronic affinity, dielectric constant, the work function and the lattice constant. [105, 106].

Heterojunctions are classified into sudden heterojunctions and graded heterojunctions and sub-classified as different connection points on both sides of the divide. The semiconductor has the same name as the connection-symmetric uniform combination (heterojunctions isotype) such as (p-p), (n-n), otherwise a different combination of asymmetric (An isotype heterojunctions) such as called (n-p), (p-n) [107].

Heterojunctions have unique electrical and optical properties and can be divided into three classes [108, 109]:

1. The first class is between two different semiconductor wafers, such as PZT and Si.
2. The second class is between metals and semiconductors, the ohmic connection such as Al and PZT.
3. The third class is between the phase semiconductor crystals with the same type of semiconductor random phase, such as c-Si with a-Si.

2.11 Solar Cells

A solar cell is a (p-n) junction device that converts the incident sunlight to electrical power without applied voltage (photovoltaic PV mode) and pollution and noise. When the light ($hv > E_g$) strikes the cell, the electron-hole pairs will be created in the space charge region. Electrons in the conduction band and holes in the valence band can contribute to produce the current under the electrical field which sweeps out and produces the photocurrent (I_{Ph}) in the reverse bias direction as shown in figure (2.8). Short circuit current (I_{sc}) and the open circuit voltage (V_{oc}) are very important parameters that characterize the performance of a solar cell [110, 111].

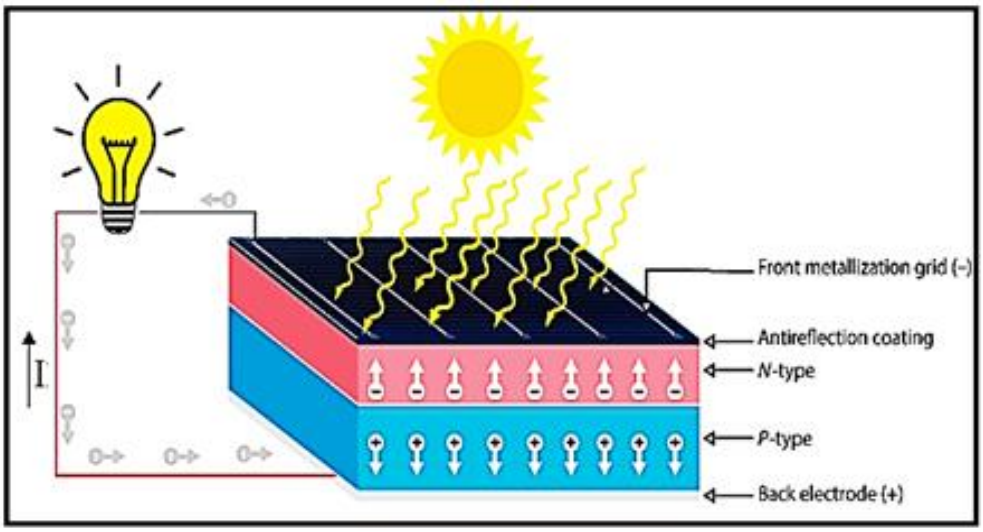

Fig. (2-8) Operation of a solar cell [109].

2.11.1 I-V Characteristics of Solar Cell

The I-V curve of solar cells describes the current and voltage characteristics of a specific photovoltaic (**PV**) cell. It gives a detailed description of its solar energy conversion ability and efficiency. Knowing the electrical I-V characteristics of a solar cell is critical in determining the device's output performance and solar efficiency.

The main electrical characteristics of a (**PV**) cell are summarized in the relationship between the current and voltage produced on a typical solar cell I-V characteristics curve. The intensity of the solar radiation that hits the cell controls the current, while the increases in the temperature of the solar cell reduce its voltage [112, 113].

The I-V curve of a solar cell is the superposition of the I-V curve of the solar cell diode in the dark with the light-generated current. The light has the effect of shifting the I-V curve down into the fourth quadrant where power can be extracted from the diode. Illuminating a cell adds to the normal "dark" currents in the diode so that the diode law becomes [112, 113]:

$$I = I_0 [\exp(qV/nkT) - 1] - I_L \qquad (2.32)$$

Where *n* is the ideality factor and I_L is the light generated current.

Figure (2.10) represents the I-V curve of the solar cell in the dark and under light [114].

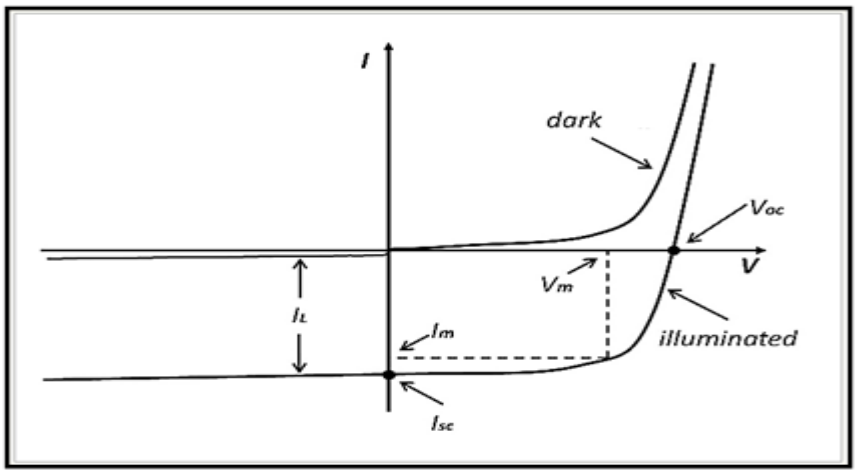

Fig. (2-9) The I-V curve of the solar cell in a dark and under light [114].

2.11.2 Solar Cell Circuit and Device Parameters

A photovoltaic cell may be represented by the equivalent circuit model shown in figure (2-10) [115]. This model consists of current due to optical generation (**I_L**), a diode that generates a current, a series resistance (R_s), and shunt resistance (**R_{sh}**). The series resistance is due to the resistance of the metal contacts, ohmic losses in the front surface of the cell, impurity concentrations, and junction depth. The series resistance is an important parameter because it reduces both the short-circuit current and the maximum power output of the cell. Ideally, the series resistance should be (**$R_s = 0$**). The shunt resistance represents the loss due to surface leakage along the edge of the cell or due to crystal defects. Ideally, the shunt resistance should be infinite (**$R_{sh} = \infty$**) [111, 116].

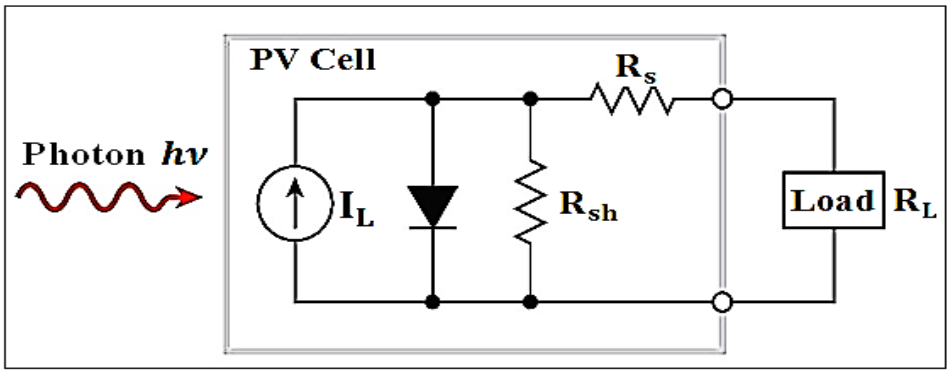

Fig. (2-10) Idealized equivalent circuit of a photovoltaic cell [115]

There are several parameters are used to characterize solar cells.

1. **Open circuit voltage (V_{oc})**: It is the maximum voltage produced by a solar cell (the resistance reaches infinity) and the net current is zero and given by the following equation [106, 116]:

$$V_{oc} = \frac{nk_BT}{q} \ln\left(\frac{I_{sc}}{I_0} + 1\right) \qquad (2.33)$$

Where T is the temperature, q is the electron charge, and I_o is the reverse saturation current or the dark current.

2. **Short circuit current (I_{sc})**: The current that flows through the solar cell when it is short-circuited (the resistance of load is zero) which leads to (V = 0 volt) and given by the following relation [110, 116]:

$$I_{sc} = I_s\,[exp(qV_{oc}/kT) - 1] + V_{oc}/R_{sh} \qquad (2\text{-}34)$$

Where R_{sh} is the shunt resistance.

The short-circuit current depends on a number of factors such as the solar cell area, the number of photons, the spectrum of the incident light, and the optical properties (absorption and reflection) of the solar cell.

3. **Fill factor (FF):** The fill factor measures how far the I-V characteristics of an actual PV cell differ from those of an ideal cell. The fill factor is given by the relation [102-114]:

$$F.F = \frac{I_m V_m}{I_{sc} V_{oc}} \quad (2.35)$$

4. **Conversion efficiency** (η): is a measure of the amount of light energy that is converted into electrical energy and is given by[102-114]:

$$\eta = \frac{P_m}{P_{in}} x\ 100\ \% = \frac{I_m V_m}{P_{in}} x\ 100\ \% \quad (2.36)$$

Where P_m is the maximum power output and P_{in} is the power input to the cell defined as the total radiant energy incident on the cell's surface.

3.1 Introduction

This chapter emphasizes the experimental descriptions used by pulsed laser ablation techniques in the manufacture and investigation of Silicon-graphene-Zinc nanocomposites. The instruments used to analyze the thin films include X-ray diffraction (XRD), Atomic Force Microscopy (AFM), and Scanning Electron Microscopy (SEM), X-ray photoelectron spectroscopy (XPS) or Electron Spectroscopy for Chemical Analysis (ESCA), Raman Spectroscopy, studied into structural and morphological features. The optical properties and the setting measurements of the photodetector and Solar cell are also studied. The schematic diagram of the experimental work starting from material up to film characterization is shown in Figure (3-1).

3.2 Materials

The imported materials were prepared from international origins. Table (3-1) shows the materials used in the research, their purity percentage, and country.

Table (3-1) of the materials used in the research, their purity percentage, and country.

Materials	Purity (%)	Company and Country
Si wafer*	99.8	Sigma Aldrich-China
HF acid	ACS reagent" with a 48% concentration	Sigma Aldrich-China
HNO_3 acid	65% concentration	Sigma Aldrich-China
$AgNo_3$	98	EMD Milipore Corporation - Made in Germany
Graphite	98.9	Henan CXH Purity-China
Zinc	99.9	Hi Media Laboratories Pvt. Ltd. LBS Marg, Mumbai- Made in India

*Silicon wafer Crystal Orientation:110 , model P-Type, standard-GB, Made in China.

3.3 The steps of preparation

Figure (3-1) depicts a schematic representation of the experimental study.

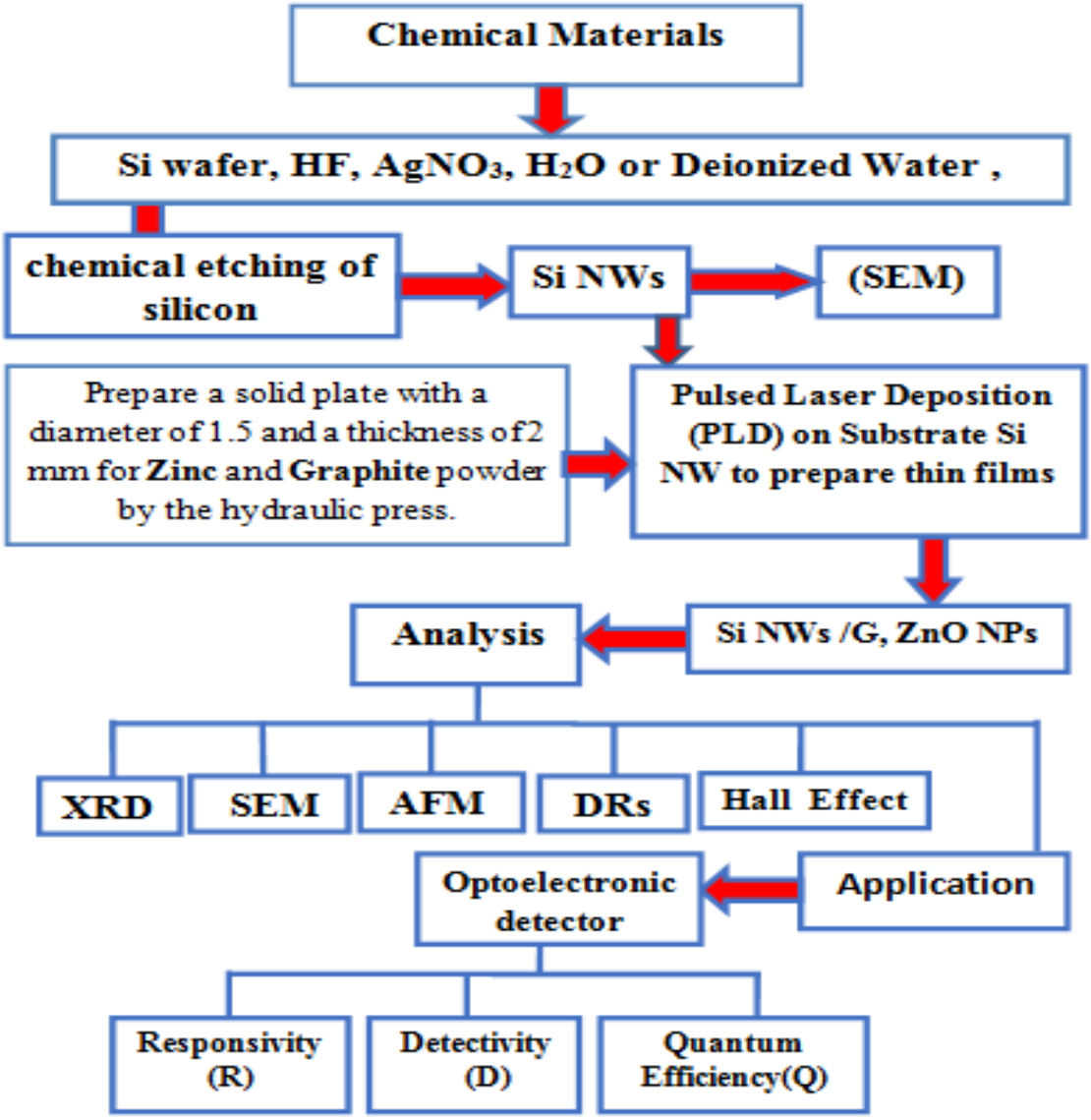

Fig. (3-1) Schematic diagram of experimental work.

3.4 Preparation of the Nanocomposite

3.4.1 Targets Preparation (graphite, zinc)

Molecular weight ratios (8 g) of the material (graphite) were taken using a sensitive electronic digital balance with high accuracy and grind it using a pottery mortar for (20) minutes, then the powder was placed in a small pressure mold after cleaning, with a width of 2 cm and a thickness of 2 mm, which It is

placed inside a hydraulic press under a pressure of (20 MPa) for graphite as well as for zinc under a pressure of no more than 10 tons of zinc, according to the nature of the material.

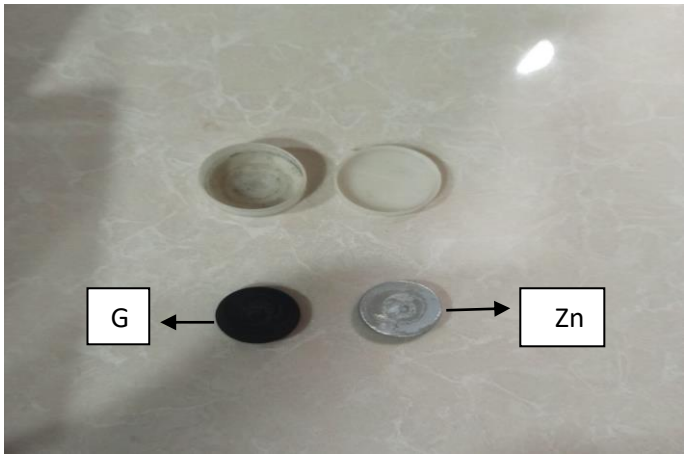

Fig. (3-2) A piece of graphite and zinc after pressing.

.35 Films Deposition

The deposition process of thin films consists of the following steps:

.35.1 Silicon Etching

P-type silicon substrates have been used for the deposition of thin films. These substrates are cut into square pieces with dimensions (2 x 2) cm2. The thickness of about (0.5 mm). The process of cleaning substrates is essential due to the influences of the organic or dust that affect the properties of the thin film. This process can be described as the following steps:

1. The substrates are cleaned in distilled water to remove the impurities from their surface.
2. Immersed the substrates in a beaker containing pure alcohol (C_2H_5OH) for (12-15) min to clear any organic.
3. The silicon substrates have been placed in a container containing a combination of 50% HF, 50% Deionized water, and 0.03 gm of AgNo3 for 4 hours.

The substrates were dried by exposing them to air. Finally, the slides are kept in a container and thus ready for the thin film deposition. The deposition procedure is carried out promptly after the silicon substrates have been withdrawn from the container.

3.5.2 Pulsed Laser Deposition (PLD)

The Nd: YAG laser Q-switched, Second Harmonic Generation (SHG), (Diamond-288 pattern EPLS-Huafei Tongda Technology) is used for PLD, the deposition of graphene and zinc on silicon nanowire substrates. They are placed in a vacuum chamber under vacuum pressure (10^{-4} mbar). The whole system consists of a light route system, power supply system, cooling system, and computer control system. The light route system is integrated into the manual handle. The control and cooling systems are installed in the machine box of the power supply. The Nd: YAG laser system was utilized to precipitate thin films with easy-to-control major parameters, which is located at the University of Babylon, College of Science for Women, as shown in table (3.2) and Figure (3-3), the samples parameters shown in table (3.3).

Table (3.2) Laser parameters for PLD.

Lasers Specification	
Laser type	**Q-switching (Nd:YAG)**
Wavelength	**1064 nm**
Pulse duration	**10 ns**
Pulse energy	**10 -1000 mJ**
Lens focal length	**30 cm**
Frequency	**6 Hz**
Pulse width	**10 ns**
Diameter of Beam	**3 mm**
Divergence	**0.1mrad**

Fig. (3-3) Pulsed Laser Deposition (PLD) system.

Table (3.3) samples parameters

Samples	material	Pulses
S1	SiO NWS	-
S2	SiO NWS/G NPs	500P
S3	SiO NWS / ZnO NPs	500P
S4	SiO NWS /G/ ZnO NPs	500P
S5	SiO NWS /G/ ZnO NPs	400P
S6	SiO NWS /G/ ZnO NPs	300P
S7	SiO NWS /G /ZnO NPs	200P

3.5.3 Deposition process

1- The vacuum chamber has been cleaned with acetone alcohol and a soft cloth, leaving it for about 24 hours exposed to air.

2- Clean quartz and silicon substrates have been located on the substrate holder so that it is opposite the target placed on the rotating target holder so that the distance between the target and the substrate is 3 cm.

3- Focus the laser beam of Nd-YAG with energy (500mJ) and pulse number (1000) on the targets using a lens with a convex focal length of 30 cm on the surface of the rotating target at an angle of 45°.

4- The vacuum chamber is closed with all valves closed and the discharge process starts by opening the valve of the rotary pump when the pressure reaches about (10^{-2}) mbar. Then it is closed and the valve of the diffusion pump is opened until the vacuum chamber reaches (10^{-5}) mbar.

5- To increase the material removed adhesion to the substrate, the substrate is heated by a halogen lamp until the temperature reaches 300 C.

6- The laser pulse generated a plasma state, and the particles reached the substrate and deposited while the discharge chamber valve remained open. After the deposit, all films were annealed in air at 750 °C for 5 hours.

7- Finally, the thin films of Graphene and Zinc material are obtained on Silicon nanowire substrates and are subjected to structural, electrical, optical, and detectors tests.

3.6 The Thickness Thin Films Measuring

The interferometric Ellipsometer from Holark Company was used for the determination of the thickness of the films deposited as in Figure (3.4). The approach is based on the interference of the reflection of the light beam from the thin film surface and the bottom of the substrate and uses the He-Ne Laser with a wavelength of 600 nm.

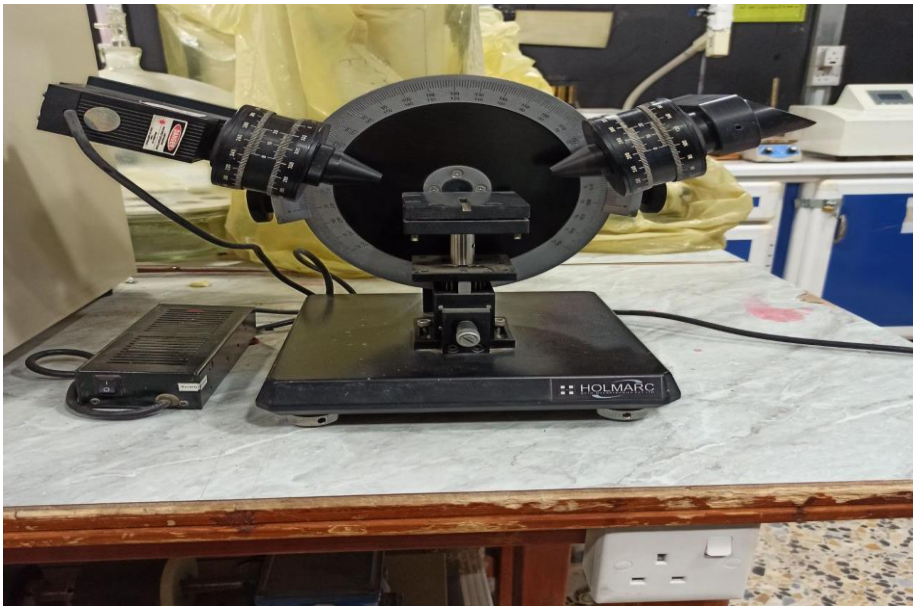

Fig. (3.4) Ellipsometer for measuring the thickness of thin films.

3.7 Structural and Morphological Measurements

The structural and morphological properties to find out the crystal structure, stresses, crystal and volumetric volumes, and surface roughness were measured using a number of examination systems for the thin film nanocomposites.

3.7.1 X-Ray Diffraction

Use the X-ray diffraction device (SHIMADZU, type XRD-6000), Japan, located at Ibn Al-Haytham College of Education/University of Baghdad. The crystal structure and the particle size of the crystalline material, which play an important role in the properties of the material, can be easily found from the X-ray spectrum by using the method of finding the mid-width at the top of the curve (FWHM)), then measuring the particle size from the Scherer equation, the density of the dislocations, the stress, and the figure (3-5) that represents the diffraction device used in the research.

Fig. (3-5) X-ray diffraction device.

3.7.2 Atomic Force Microscopy (AFM)

The atomic force microscope system, (Angstrom company, German, model (A3000)) located in the Ministry of Science and Technology / University of Baghdad, was used to find the average diameters of the prepared nanoparticles and the statistical distribution of particles, surface roughness, volumetric ratios, accumulation ratios and figure (3-6) shows the atomic force microscope used.

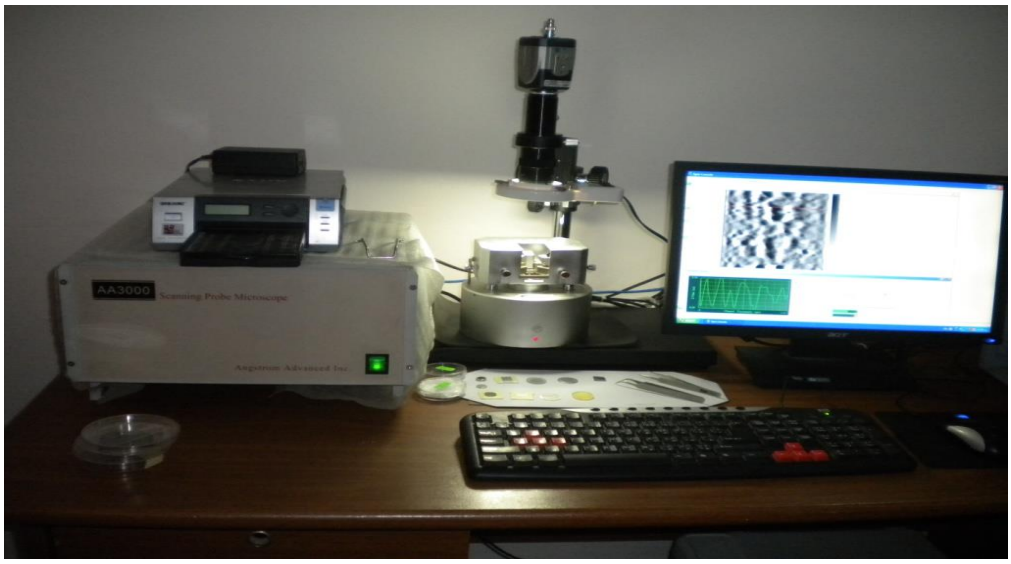

Fig. (3-6) Atomic force microscope device (AFM).

3.7.3 Scanning Electron Microscope (SEM)

The scanning electron microscope (INSPECT company, type 550, German), located in the College of Pharmacy/University of Babylon, was used to show nanowire and to measure particle sizes and shapes. Figure (3-7) illustrates the scanning electron microscope used in the research.

Fig. (3-7) The Scanning Electron Microscope (SEM) .

3.7.4 X-ray photoelectron spectroscopy XPS or ESCA

The X-ray photoelectron spectroscopy (XPS) or (ESCA) Electron Spectroscopy for Chemical Analysis is an advanced analytical technique that provides valuable chemical information about the composition, elemental and chemical state of the surface of materials. (TEKSAN company, Laser wavelength: 532 nm, Laser power from 0.5 to 70 milliwatts), located in the University of Tehran/ Iran, Figure (3-8) illustrates the X-ray photoelectron spectroscopy (XPS) used in the research.

Fig. (3-8) The X-ray photoelectron spectroscopy (XPS).

3.7.5 Raman Spectroscopy

Raman spectroscopy is the analytical technique where scattered light is used to measure the vibrational energy modes of the sample. This technique provides both the information on chemical and structural characteristics of the material and also the identification of substances through the detection of Raman scattering from the sample. (HORIBA (XPLORA PLUS) company, Laser wavelength 532 nm,), located in the University of Tehran/ Iran, Figure (3-9) illustrates the Raman Spectroscopy used in the research.

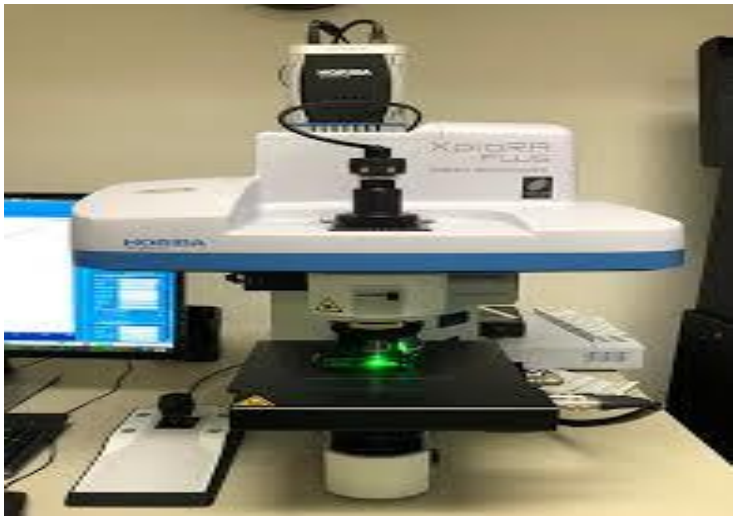

Fig. (3-9) The Raman Spectroscopy.

3.8 Optical Measurement

The optical measurements of the nanocomposite thin films are obtained by using a spectrophotometer (She made by Phillips, a Japan), as shown in fig. (3.11). the optical properties are calculated from these optical measurements.

3.8.1 Diffuse Reflectance UV-VIS Spectroscopy

The Diffuse Reflectance Spectroscopy system manufactured by (Avantes) company, model (DH-S-BAL-2048 UV-VIS), in a Wavelength range of (230-1100 nm), as shown in fig. (3.10), of Netherlands origin, located in Al Nahrain University / Baghdad, Jadriya, was used to find the Reflectance of the samples.

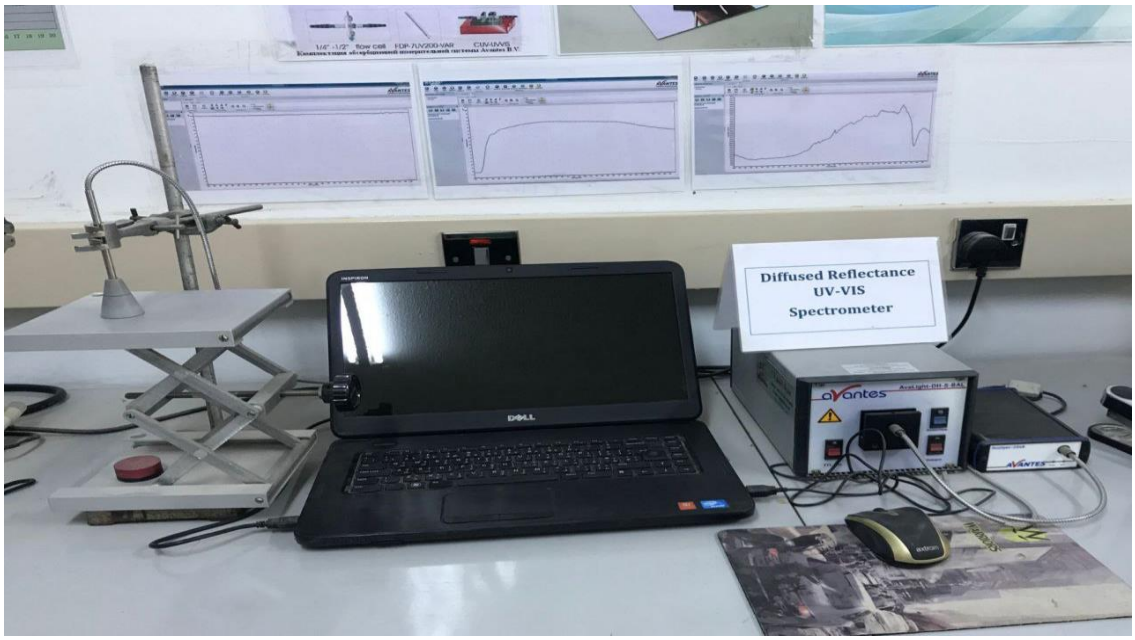

Fig. (3-10) Diffuse Reflectance UV-VIS Spectroscopy (DRS) system.

3.9 Electrodes Deposition

3.9.1 Electrodes deposition for Hall Effect

Aluminum sheets were used as a mask and were placed on films to deposit the aluminum on the surface of the nanocomposite by using thermal evaporation equipment (Edward). The electrodes are deposited by using aluminum wire placed in (Tangiesten W) boat material under pressure (10^{-5} Torr) with a diameter of (0.2) cm as illustrated and prepared as in Fig. (3.11).

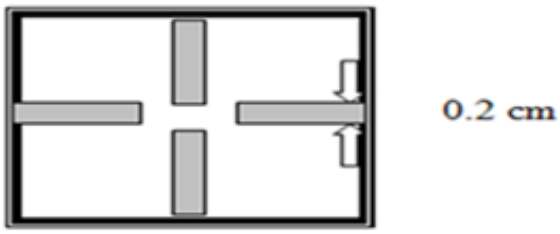

Fig. (3-11) The mask which used for the Hall effect

3.9.2 The Hall Effect

Hall Effect measurements of deposited films were carried out to know the charge carriers type and to calculate the Hall coefficient (R_H), the concentration of carrier, resistivity and mobility by using a device (Measurement Hall Effect System) type (HMS 3000) manufactured by (Ecopia) Taiwanese origin. It is possible to identify both of type and density of charge carriers using the intensity of the magnetic field (B = 0.55 T) and through the relationship between measured current (I) and Hall voltage (V_H). If the relationship is direct, the film is a positive type (P-type), while the film is negative (n-type) if the relationship is inverse [94, 95]. Carrier concentration, carrier type and mobility have been determined from Hall Effect measurements for the nanocomposite, the device is located in the College of Science, University of Baghdad, as shown in Fig. (3.12).

Fig. (3-12) The experimental set up of Hall effect.

3.10 Application

3.10.1 Preparation p-n junction and electrode deposition for Photo detector

By using the spin coating method with a speed (3000 rpm) for (15 second) to deposition of nanocomposite solution on the wafer silicon (Si)(p-type) substrate to fabricate p-n junction and then deposited electrodes on the surface of the nanocomposite by using silver baste as shown in fig.(3.13).

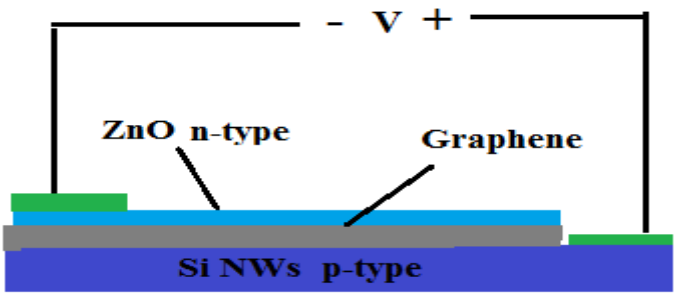

Fig. (3-13) The p-n junction of the nanocomposite (SiO NWs/G/ZnO NPS).

3.10.2 Photo Detector Measurement

The measurements of the spectral responsivity were performed using a double-beam UIR-210A spectrophotometer operating within the range (200-1000) nm of wavelengths while the current measurements were performed using a 8010 DMM Fluke digital multimeter are shown in fig.(3.14).

Fig. (3.14) The system of the Photodetector.

3.10.3 Sensing Measurements (Solar Cell):

3.10.3 Electrical Properties of Heterojunction

The electrical measurements for the p-SiO NWs, p-SiO NWs/G NPs, p-SiO NWs/n-ZnO NPs, and p-SiO NWs/G,n-ZnO NPs ..(500P) heterojunctions, which are prepared on the SiO NWs substrate and different contents of G,ZnO. Which was deposited using the (PLD) method. Current-voltage characteristics for the heterojunctions are measured in dark and illumination conditions.

1. The I-V Characteristics in the Dark Condition

The current-voltage measurements at dark are fulfilled for p-SiO NWs, p-SiO NWs/G NPs, p-SiO NWs/n-ZnO NPs, and p-SiO NWs/G,n-ZnO NPs ..(500P heterojunctions as shown in figure (3.15).

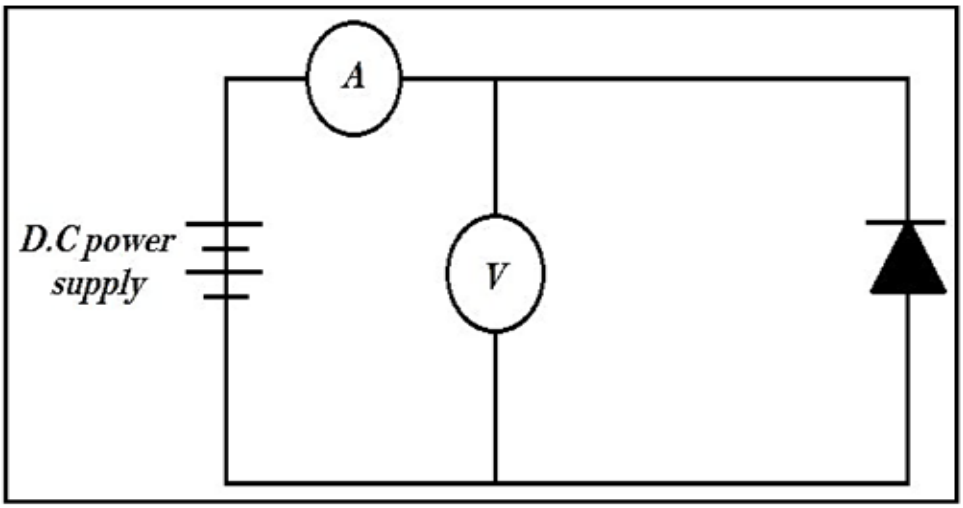

Fig. (3-15) Circuit diagram for I-V measurement in the dark.

2. The I-V Characteristics under Illumination Condition

The I-V measurements were made for p-SiO NWs, p-SiO NWs/G NPs, p-SiO NWs/n-ZnO NPs, and p-SiO NWs/G,n-ZnO NPs ..(500P) as shown in figure (3.16) heterojunctions when they exposed to a halogen lamp light source with a power of (120W) and an intensity of (105 mW/cm^2). The bias voltage changes in the range of (-5 to 5) volts in the forward and reverse bias. The device is located in the College of Science, University of Baghdad.

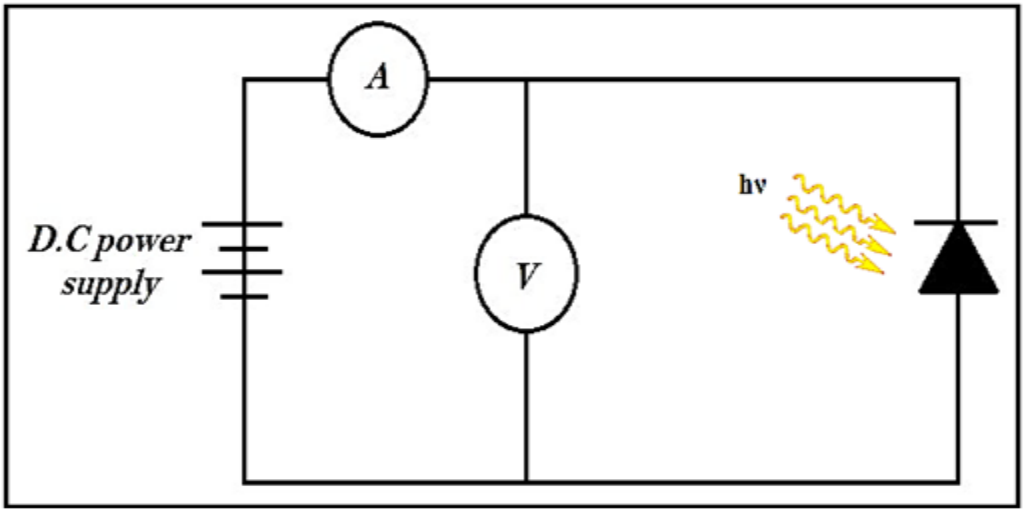

Fig. (3-16) Circuit diagram for I-V measurement in the illumination.

4.1 Introduction:

In this chapter, comprehensive results were obtained and analyzed using various characterization techniques such as thickness measurement (Ellipsometer), X-ray Diffraction (XRD), atomic force microscopy (AFM), scanning electron microscopy (SEM), X-ray photoelectron spectroscopy (XPS) or Electron Spectroscopy for Chemical Analysis (ESCA), Raman Spectroscopy, Diffused Reflectance spectrometer (DRS) the optical characteristics, and electrical Measurements (Hall Effect). The interpretation of these results provides valuable insights into the structural and morphological properties of the materials investigated, focusing on their application in photodetectors and solar cells.

This chapter will be divided into two sections. The first section will focus on the effect of the number of pulses on the thin film, while the second section will explore the application of the nanocomposite.

4.2 Structural and Morphological Properties

4.2.1 Thickness Measurement (Ellipsometer):

To determine the thickness of the deposited films, an Ellipsometer interferometer from Holark was employed. This technique relies on the interference of a light beam reflected from the surface of the thin film and the bottom of the substrate. The obtained thickness values of the thin films are summarized in Table (4-1):

Table (4-1) Samples Parameters and Film thickness for all the prepared films.

Samples	material	Pulses	Film Thickness (nm)
S1	SiO NWS	-	10000
S2	SiO NWS/G NPs	500	133
S3	SiO NWS/ZnO NPs	500	141
S4	SiO NWS/ G/ZnO NPs	500	173
S5	SiO NWS/ G/ZnO NPs	400	161
S6	SiO NWS/ G/ZnO NPs	300	155
S7	SiO NWS/ G/ZnO NPs	200	150

The table shows the thickness of thin films prepared by pulsed laser deposition (PLD). The number of pulses used to deposit the thin films is also shown in the table.

The thickness of the thin films increases with the number of pulses used to deposit them. This is because the number of pulses determines the amount of material deposited on the substrate. The thickness of the thin films also increases with the addition of graphene and zinc oxide nanoparticles. This is because graphene and zinc oxide nanoparticles are larger than silicon nanowires, so they take up more space on the substrate.

4.2.2 X-ray diffraction tests (XRD):

The X-ray diffraction (XRD) patterns of the SiO NWs/G/ZnO (500 Pulse), SiO NWs/G/ZnO (400 Pulse), SiO NWs/G/ZnO (300 Pulse), and SiO NWs/G/ZnO (200 Pulse) thin films are shown in Figure (4-1). The XRD pattern of the Si NWs/G/ZnO (500Pulse) thin film shows peaks at 11.91°, 24.00°, 26.37°, 32.92°, and 36.41°,as well Si NWs/G/ZnO (400Pulse)S5, Si NWs/G/ZnO (300Pulse)S6 and Si NWs/G/ZnO (200Pulse)S7 but with different number of pulses, It is noted that the same sharp peaks have appeared but with less intensity, Therefore, we

will limit the work to the best and clearest sample which is SiO NWs/G/ZnO …(500 Pulse)S4 in the the second section will explore the application of the nanocomposite.

The X-ray diffraction (XRD) patterns of the SiO NWs, SiO NWs/GO, SiO NWs/ZnO, and SiO NWs/G/ZnO thin films are shown in Figure (4-1). The XRD patterns show that all of the thin films are hexagonal with a hexa phase. The sharp peaks in the XRD patterns correspond to the characteristic diffraction peaks of SiO, GO, ZnO, and Si.

The XRD pattern of the SiO NWs thin film shows peaks at 32.92°, 33.14°, 28.45°, and 47.98°, which correspond to the (111), (201), (111) and Si (220) planes of SiO, respectively according to standard [00-027-1402] , this result is consistent with the studies [117],[118],[119]. The XRD pattern of the SiO NWs/GO thin film shows peaks at 11.45°, 26.36°, and 32.92°, which correspond to the (002),(001) plane of G,GO, the (111) plane of SiO , and a broad peak related to the interlayer distance between graphene oxide sheets, respectively , this result is consistent with the studies [120,121]. The XRD pattern of the SiO NWs/ZnO thin film shows peaks at 32.92°, 33.91°, 36.24°, and 56.15°, which correspond to the (111), (301), (101), and (110) planes of ZnO, respectively [122],[123]. The XRD pattern of the Si NWs/G/ZnO thin film shows peaks at (11.91°, 24.00°, 26.37°, 32.92°, and 36.41°), which correspond to the (111) plane of SiO, the (101) plane of ZnO, the (001),(002) plane of rGO, GO, and a broad peak related to the interlayer distance between graphene oxide sheets, respectively ,this result is consistent with the studies [117,120,122,123].

The XRD results show that the addition of GO and ZnO to the SiO NWs does not significantly affect the hexagonal structure of the thin films. However, there is a slight displacement in the locations of some

characteristic peaks, which is likely due to the formation of chemical compounds between SiO, GO, and ZnO.

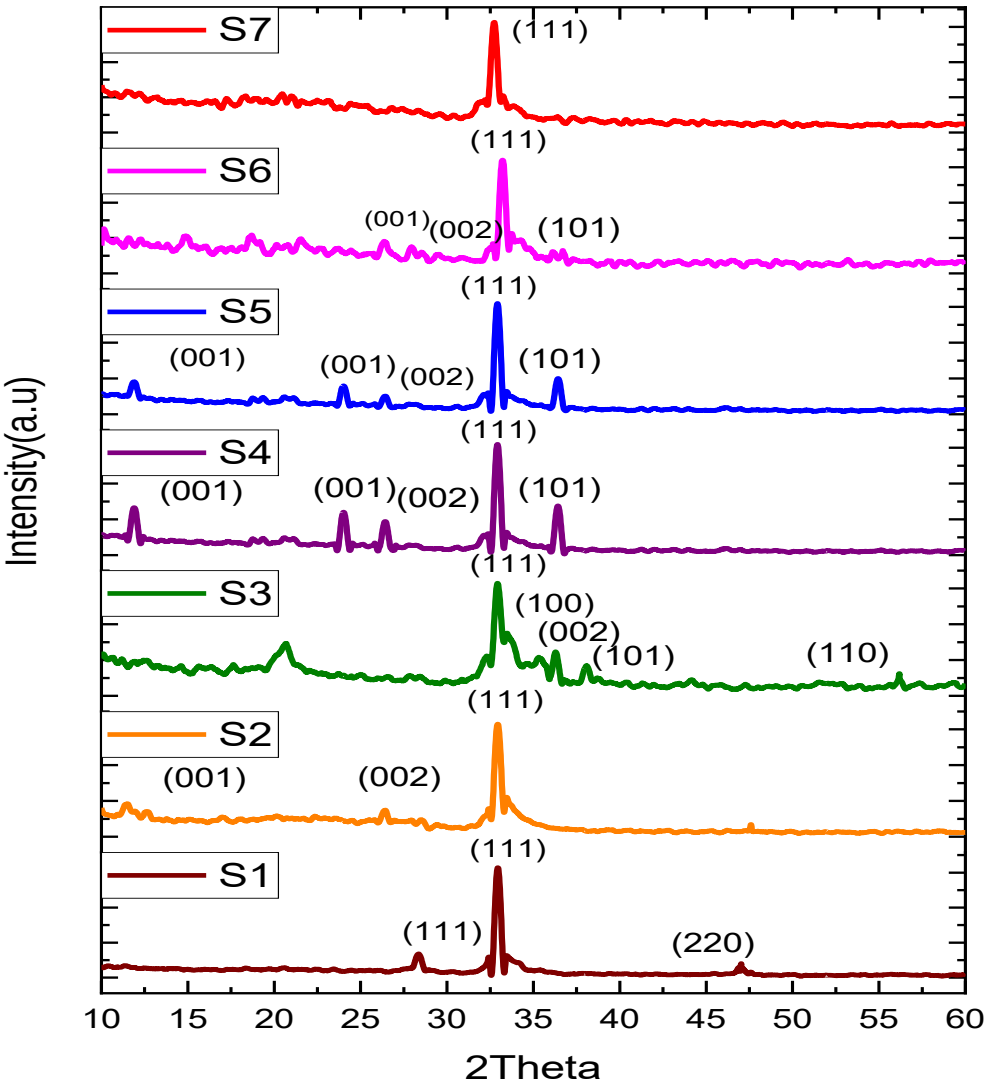

Fig. (4-1) X-ray diffraction for Samples of thin films.

The XRD-confirmed data pattern has been listed in Table (4-2), which showed excellent consistency with the interplanar distance standard values.

The table shows that the XRD results for the films (SiO NWs, SiO NWs/GO, and SiO NWs/G/ZnO) show that the addition of GO and ZnO to the SiO NWs causes the thin films to become more disordered. The SiO NWs/G/ZnO thin film is the most disordered of the three thin films,

with an average interplanar spacing of 40.99 nm, a significantly larger FWHM of the diffraction peaks, and slightly different diffraction angles than the other two thin films.

Table (4-2) values of crystalline levels and mid-width at the highest intensity and crystal sizes for samples.

Films	(hkl)	2 θ (deg)	FWHM	C.S(nm)	Avg C.S
S1-SiO NWs	Si (111)	28.45	0.3	25.11	25.27
	SiONW(111) SiONW(111)	32.92 33.14	0.28	25.87	
	Si (220)	47.98	0.3	24.83	
S2-SiO NWs/G NPs	GO (001)	11.45	0.38	20.35	20.73
	G (002)	26.36	0.38	19.91	
	SiONW(111)	32.92	0.34	21.92	
S3-SiO NWs/ZnO NPs	SiONW(111) ZnO (100)	32.92 33.91	0.38	19.61	20.5
	ZnO (002)	35.31	0.36	20.48	
	ZnO (101) ZnO (110)	36.24 56.15	0.34	21.41	
S4-SiO NWs/G, ZnO NPs(500P)	GO (001) rGO (001)	11.91 24.00	0.17	26.64	40.99
	G (002)	26.37	0.17	44.02	
	SiONW(111)	32.93	0.15	47.17	
	ZnO (101)	36.41	0.16	46.14	
S5-SiO NWs/G, ZnO NPs(400P)	GO (001)	11.16	0.26	29.22	28.51
	G (002)	26.16	0.25	29.72	
	SiONW(111)	32.93	0.25	29.04	
	ZnO(101)	36.18	0.28	26.07	
S6-SiO NWs/G, ZnO NPs(300P)	G (002)	26.13	0. 28	27.03	26.61
	Si (211)	33.22	0.28	26.27	
	ZnO(101)	36.37	0.29	26.62	
S7-SiO NWs/G, ZnO NPs(200P)	G (002)	26.91	0.29	25.88	25.85
	SiONW(111)	32.74	0.28	26.22	
	ZnO(101)	36.48	0.29	25.45	

The increased disorder in the Si NWs/G/ZnO thin film is likely due to the following factors:

- The different properties of GO and ZnO. These two materials have different chemical and physical properties, which can affect the way they pack into a crystal lattice.
- The different sizes of the GO and ZnO nanoparticles. GO nanoparticles are significantly larger than ZnO nanoparticles. This means that they are more difficult to pack into a regular crystal lattice, which can lead to disorder [124] .
- The introduction of defects into the crystal structure. The addition of GO and ZnO to the SiO NWs can introduce defects into the crystal structure of the thin film. These defects can be caused by the different chemical properties of GO and ZnO, as well as the different sizes of the GO and ZnO nanoparticles [125].

The crystal structure of SiO NWs is hexagonal, and the addition of GO does not change the crystal structure. The reason for this is that GO, which is a two-dimensional material with a hexagonal lattice structure[126]. When GO is added to SiO NWs, the GO sheets wrap around the SiO NWs, maintaining the hexagonal crystal structure. but ZnO, which is a three-dimensional material with a cubic lattice structure[126]. However, when GO and ZnO are added together, the GO sheets can interact with the ZnO nanoparticles, causing the ZnO nanoparticles to rearrange themselves into a hexagonal lattice structure in the SiO NWs/G/ZnO thin film.

The hexagonal crystal structure is more conductive than the cubic crystal structure, so the SiO NWs/G/ZnO thin film may have better electrical properties than the SiO NWs/ZnO thin film. Additionally, the hexagonal crystal structure has different optical properties than the cubic

crystal structure[127], so the SiO NWs/G/ZnO thin film may have different optical properties than the SiO NWs/ZnO thin film.

The increased disorder in the SiO NWs/G/ZnO thin film may have introduced new energy levels into the band gap of the thin film, which could lead to new optical properties[128].

4.2.3 Atomic force microscopy (AFM) results:

Atomic force microscopy (AFM) was used to study the surfaces topography and determine important parameters such as average particle size, distribution, root mean square (RMS), and roughness (Ra) of the thin films SiO NWs/G/ZnO (500 Pulse), SiO NWs/G/ZnO (400 Pulse), SiO NWs/G/ZnO (300 Pulse), and SiO NWs/G/ZnO (200 Pulse). The results, as presented in Table (4-3), It is noted that the same sharp peaks have appeared but with less intensity.

The highest value for the root mean square (RMS) roughness and average particle size were recorded at 7.95nm, 6.20 nm and 40.45 nm, respectively, for the SiO NWs/G- ZnO 500 Pulse sample. The lowest values were obtained for the SiO NWs/G/ZnO (200 Pulse) sample, with RMS roughness and average particle size of 3.12nm, 2.28nm, and 15.73 nm, respectively, which is attributed to the addition of graphene (G) and zinc oxide (ZnO) nanoparticles on SiO NWs substrate with a different number of laser pulses [129,130].as well SiO NWs/G/ZnO (400Pulse)S5, and SiO NWs/G/ZnO (300Pulse)S6, Therefore, we will limit the work to the best and clearest sample which is SiO NWs/G/ZnO (500 Pulse)S4 in the second part B- the properties Study of the compound.

The surfaces of SiO NWs/G,ZnO thin films prepared using the pulsed laser deposition (PLD) technique were examined using atomic force microscopy (AFM) to analyze their topography and determine important parameters such as average particle size, distribution, root mean square

(RMS), and roughness (Ra). The results, as presented in Table (4-3), indicate a clear change in the surface topography of the samples, which is attributed to the addition of graphene (G) and zinc oxide (ZnO) nanoparticles in thin thickness on SiO NWs substrate [129,130].

The highest value for the root mean square (RMS) roughness and average particle size were recorded at 7.95nm, 6.20 nm and 40.45 nm, respectively, for the SiO NWs/G- ZnO 500 Pulse sample. The lowest values were obtained for the SiO NWs sample, with RMS roughness and average particle size of 1.44 nm and 15.39 nm, respectively.

The difference in the grain size values measured by AFM and X-ray diffraction (XRD) is due to the fact that AFM measures the grain size directly, while XRD measures the crystal size using Scherrer's formula.

Table(4-3) AFM parameters for Samples thin films. (Ra) Roughness and (RMS) Root Mean Square.

Samples	Ra(nm)	RMS(nm)	Ave. Particle Size (nm)
S1- SiO NWS	1.44	2.04	15.39
S2- SiO NWS/G NPs	1.57	2.15	13.03
S3- SiO NWS/ZnO NPs	1.96	2.58	13.01
S4- SiO NWS/G/ ZnO NPs (500P)	6.20	7.95	40.45
S5- SiO NWS/G/ ZnO NPs (400P)	3.55	4.45	20.89
S6- SiO NWS/G/ ZnO NPs (300P)	2.77	3.62	17.86
S7- SiO NWS/G/ ZnO NPs (200P)	2.28	3.12	15.73

In Figure (4-2),the 3D AFM images of the as-deposited films show the formation of agglomerated grains stacked on top of each other. This is due to the close grains clustering together to cover the uneven peaks and hills from the silicon nanowires. Increasing the G and ZnO ratios improve the crystalline structure of the SiO NWs/G-ZnO films, which is in agreement with the XRD results. This leads to improving the responsivity properties of the films.

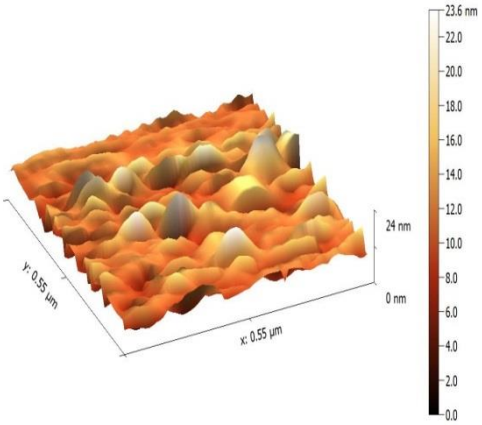

AFM images of (S1).

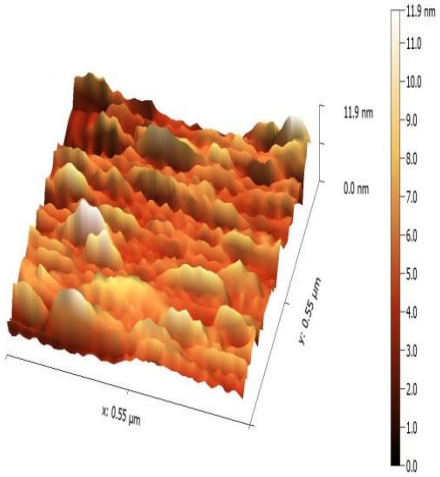

AFM images of (S2).

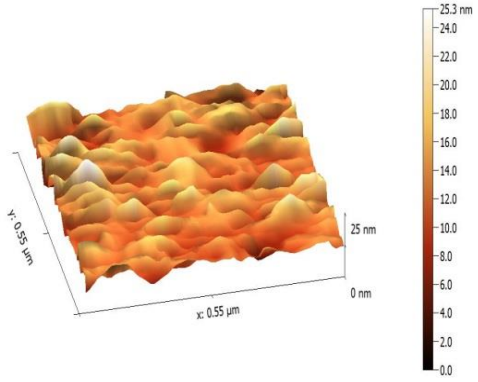

AFM images of (S3).

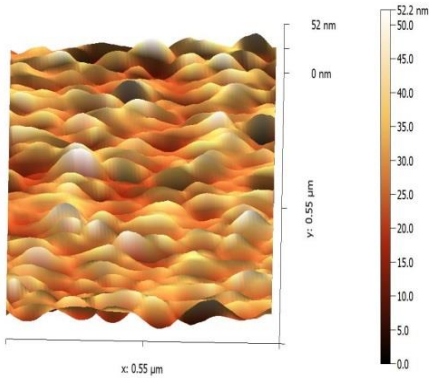

AFM images of (S4).

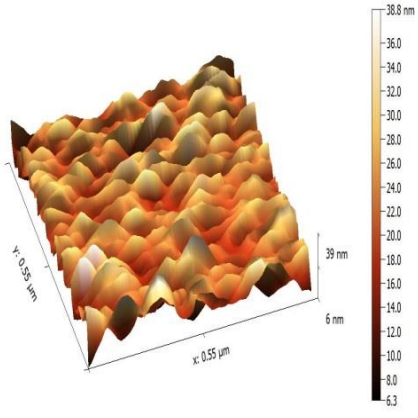

AFM images of (S5).

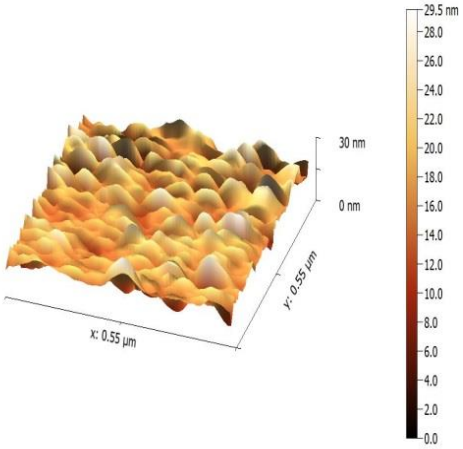

AFM images of (S6).

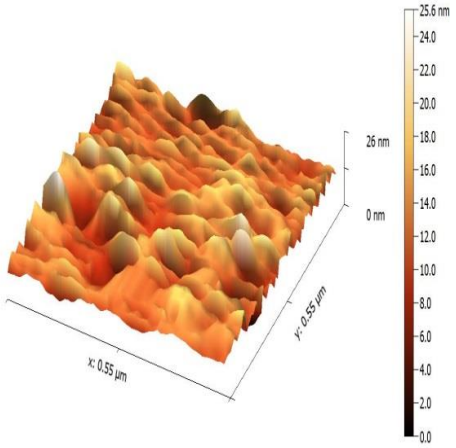

AFM images of (S7).

Fig. (4-2) Atomic force microscopy images of (S1, S2, S3, S4, S5, S6 and S7) .

4.2.4 Scanning Electron Microscopy (SEM)

(SEM) was used to examine the morphology of surface and estimate films of the SiO NWs, SiO NWs/GO, SiO NWs/ZnO, and SiO NWs/G/ZnO thin films.

(SEM) was used to study the surfaces topography of the SiO NWs/G/ZnO …(500 Pulse), SiO NWs/G/ZnO …(400 Pulse), SiO NWs/G/ZnO …(300 Pulse), and SiO NWs/G/ZnO …(200 Pulse) thin films. Through the SEM images in Fig. (4-3), it was observed that the thickness of the film deposited on a silicon nanowire substrate increased with the increase in the number of laser pulses. Thus the silicon nanowire was covered entirely in sample S4 SiO NWs/G/ZnO …(500 Pulse). So we will limit ourselves to work on it only in the second part B- the properties Study of the compound.

The SEM images presented in Figure (4-3) offer valuable insights into the shape and arrangement of the silicon nanowires. It is evident from the images that the nanowires possess varying lengths and diameters, with examples of nanowires measuring 80.11 nm and 121.8

nm in diameter. The nanowires exhibit a well-organized pattern, aligning with each other on the surface.

The deposition of the graphene and ZnO nanoparticles was carried out under uniform conditions, maintaining consistent temperature, pressure, and number of pulses within the PLD deposition chamber.

Moreover, the SEM images demonstrate the successful deposition of a thin film comprising graphene and ZnO nanoparticles onto the SiO NWs substrate. The graphene layer is clearly visible, serving as a protective cover encapsulating the silicon nanowires [129]. Additionally, the layer of ZnO nanoparticles can be observed distributed on top of the graphene layer.

The SEM results align with the findings from the AFM measurements, indicating that the introduction of graphene and ZnO nanoparticles onto the SiO NWs substrate resulted in significant changes in the surface topography of the films. The presence of the graphene layer appears to have smoothened the surface of the silicon oxide nanowires, while the ZnO nanoparticles contribute to the creation of a rougher surface.

The addition of graphene and ZnO nanoparticles led to increased roughness values and a reduction in average particle size. The enhancement of the crystalline structure observed in the SiO NWs/G, ZnO films, characterized by higher G and ZnO ratios, correlates with improved responsivity properties, consistent with the XRD results.

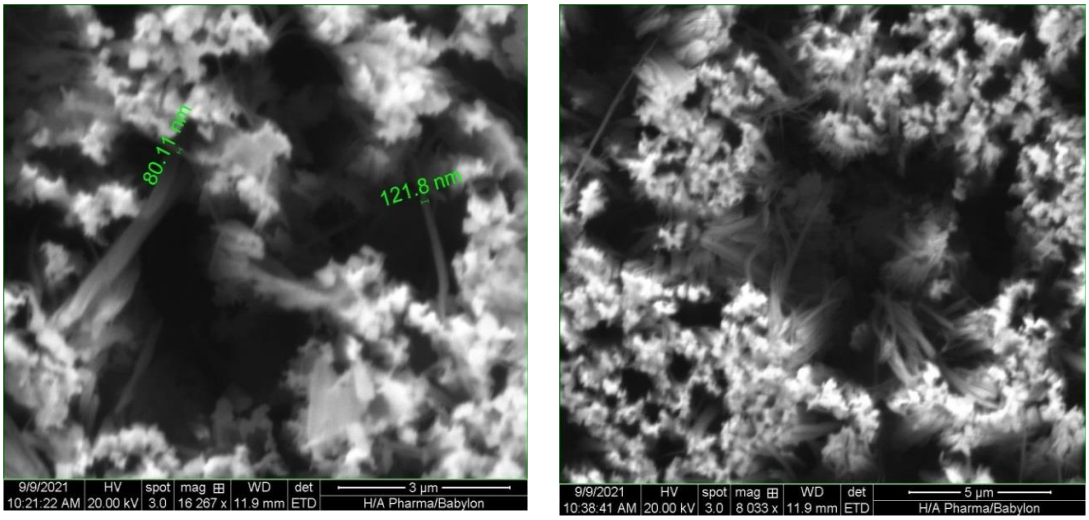

SEM images for SiO NWs

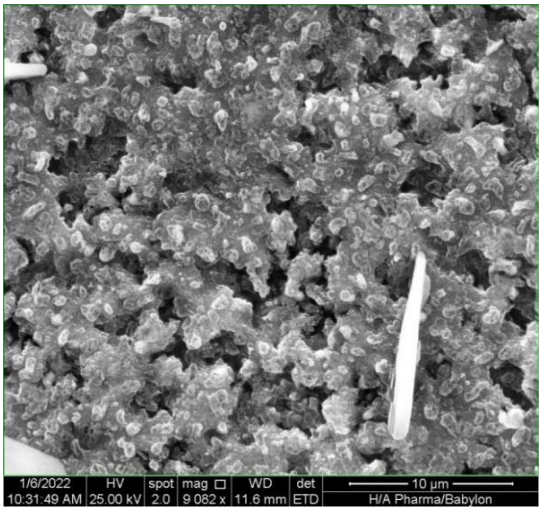

SEM images for (S2).

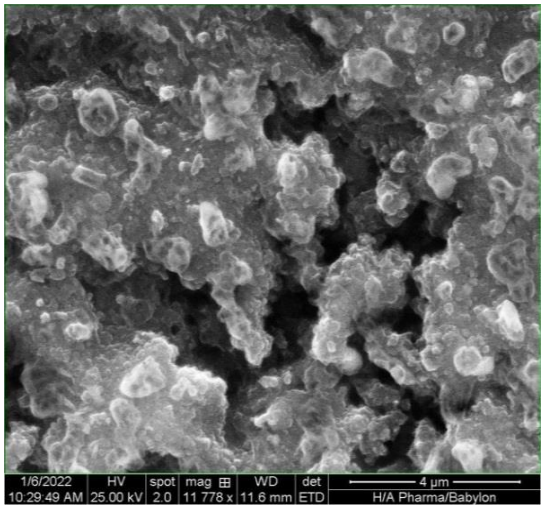

SEM images for (S3).

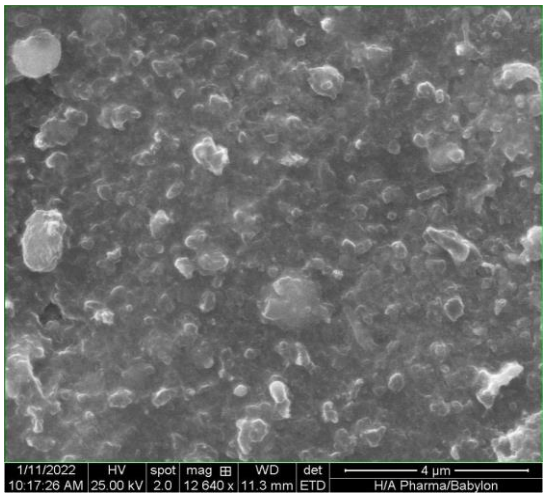

SEM images for (S4) at 500Puls

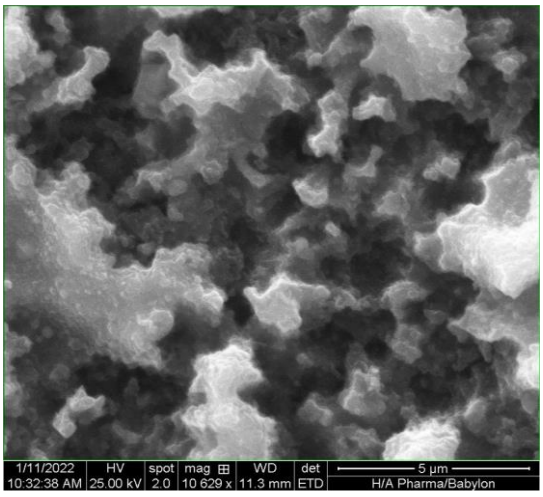

SEM images for (S5) at 400Pulse

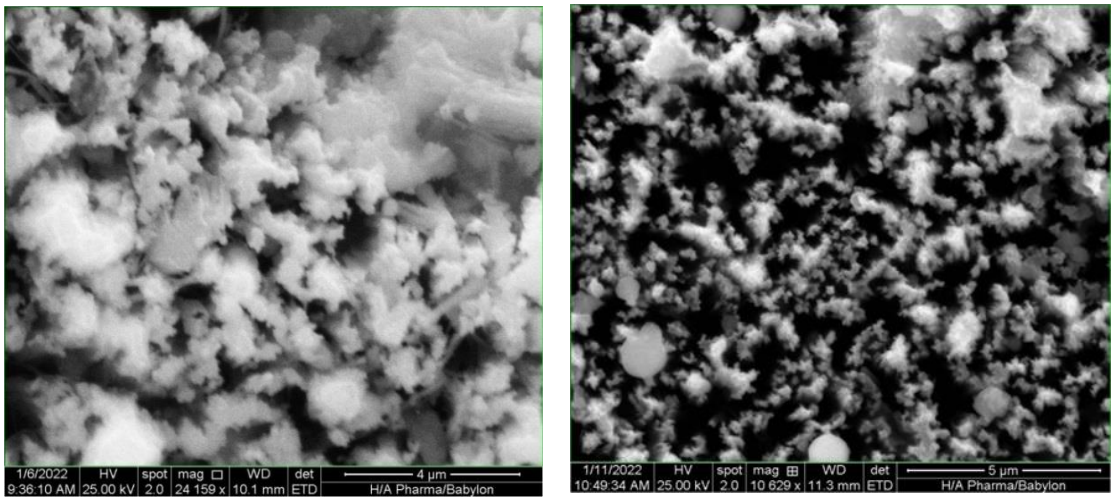

SEM images for (S6) at 300Pulse **SEM images for (S7) at 200Pulse**

Fig. (4-3) SEM images for thin films S1, S2, S3, S4, S5, S6,and S7.

4.2.5 X-ray photoelectron spectroscopy (XPS)

X-ray photoelectron spectroscopy (XPS) can be used to determine the chemical composition of the surface of the material, including silicon nanowires (SiO NWs), the XPS spectrum will typically show peaks corresponding to the Si 2p and Si 2s core-level electrons. The Si 2p peak can be used to determine the silicon atoms' oxidation state and the presence of any surface contaminants or adsorbates. The Si 2s peak can provide information about the electronic structure of the silicon atoms.

The diameter of SiO NWs can affect the XPS spectrum by introducing surface effects and changing the surface-to-volume ratio of the nanowires. As the diameter of SiO NWs decreases, the surface-to-volume ratio increases, which leads to a higher fraction of surface atoms and a more significant contribution of surface effects to the XPS spectrum [134].

The different binding energies and intensities observed in the Si 2p peak in the XPS results can indeed be attributed to the chemical

environment of the Si atoms and the interactions with other elements in the samples as shown in Figure (4-4).

When graphene is deposited on the SiO nanowires, the presence of graphene affects the electronic structure of the Si atoms. The donation of electrons from graphene to silicon leads to a lower binding energy of the Si 2p electrons, causing the peak to shift to a slightly lower binding energy range of 99-101 eV.

Similarly, when SiO nanowires are combined with ZnO nanoparticles, the Si atoms interact with zinc, leading to further changes in the electronic structure. The donation of electrons from zinc to silicon leads to a lower binding energy of the Si 2p electrons, resulting in a shift of the peak to 15600.

In the SiO NWs-graphene-ZnO sample, the Si atoms are exposed to a combination of oxygen, graphene, and zinc. This complex chemical environment results in a broadening of the Si 2p peak. The broadness indicates that the Si atoms have a range of binding energies due to their diverse interactions with different elements.

Additionally, the intensity of the Si 2p peak is influenced by the number of Si atoms in the sample and the amount of X-rays absorbed. The presence of graphene and zinc may partially block the X-rays from reaching the Si atoms, leading to a decrease in the peak intensity compared to the bare SiO nanowires.

We noticed the absence of XPS peaks for graphene and zinc may suggest that the thickness of these layers is exceptionally thin, potentially falling below the detection limits of the XPS technique.

Another possibility is that the graphene and ZnO layers are not well-dispersed on the SiO NWs. This could prevent the XPS instrument from detecting the peaks, even if the layers are thick enough [135].

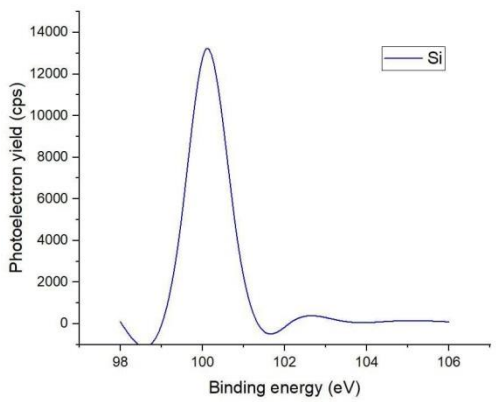

XPS images for (S1).

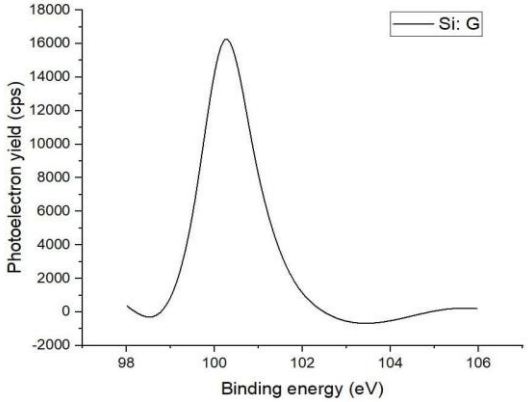

XPS images for (S2).

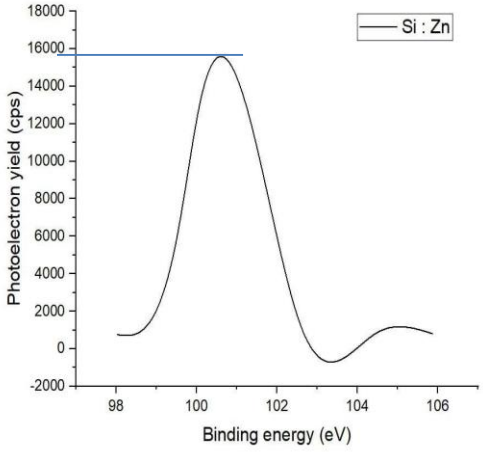

XPS images for (S3).

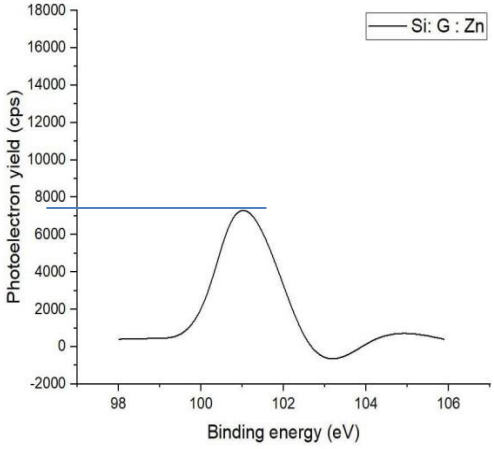

XPS images for (S4).

Fig. (4-4) XPS images for thin film S1,S2,S3,and S4 at 500Pulse

4.2.6 Raman Spectroscopy

Analyzing the Raman spectrum of SiO NWs, valuable information regarding their crystal structure, size, strain, and doping can be obtained. The Raman peaks observed in SiO NWs are influenced by the size and shape of the nanowires, as well as the confinement of phonons in the one-

dimensional structure of the nanowires. As the diameter of SiO NWs decreases, the Raman peaks shift to higher wavenumbers, and their intensities decrease due to the higher phonon energy and reduced phonon density of states [136].

The addition of zinc oxide (ZnO) to SiO NWs results in an increase in the Raman peak intensity from 1230 to 6000, indicating a decrease in phonon energy and speed. This suggests that the presence of ZnO causes the SiO NWs to become more strained, potentially due to differences in thermal expansion coefficients between SiO NWs and ZnO.

When graphene is added to SiO NWs, an additional peak is observed in the Raman spectrum at 525 cm-1, similar to the peak at 550 cm-1 in SiO NWs. This shift in peak position suggests compressive strain in the graphene, potentially due to interaction with SiO NWs. The G and D peaks associated with graphene and graphene oxide (GO), respectively, are also present in the Raman spectrum[121,129].

The G peak in the Raman spectrum of graphene is located around 1600 cm-1 and represents the Raman scattering of the E2g phonon mode, indicating in-plane vibrations of carbon atoms in the graphene lattice. The D peak, located at approximately 1380 cm-1, corresponds to the Raman scattering of the disorder-induced phonon mode in GO, associated with defects and disorder in the GO lattice[121].

The G/D ratio, calculated as the ratio of the intensities of the G and D peaks, provides information about the degree of disorder in the graphene or GO lattice. In SiO NWs/GO, the G/D ratio is calculated as 250/230, resulting in a value of 1.08, indicating a relatively disordered GO lattice. The presence of the C-O stretching mode around 1000 cm-1 further confirms the presence of GO in the SiO NWs/GO sample [121,129].

Upon the addition of ZnO to SiO NWs/GO, the G/D ratio increases to 1080/900, resulting in a value of 1.2. This indicates that the addition of ZnO leads to increased orderliness in the GO lattice. The increase in the G/D ratio may be attributed to the interaction between ZnO and GO, contributing to the reduction of disorder in the GO lattice[120,121].

Additionally, the Raman spectrum of GO may exhibit other peaks related to the presence of functional groups, such as the C-O stretching mode around 1000 cm-1. The presence of a peak around 1600 cm-1, commonly observed in the Raman spectrum of graphene, suggests the possibility of a coating layer of reduced graphene oxide (RGO) on SiO NWs[120].

The results obtained from Raman spectroscopy, along with other analytical techniques such as AFM and XRD, consistently demonstrate that the addition of graphene and ZnO to SiO NWs leads to significant changes in their properties. These changes include the ordering of GO, the strain in SiO NWs, and variations in surface roughness.

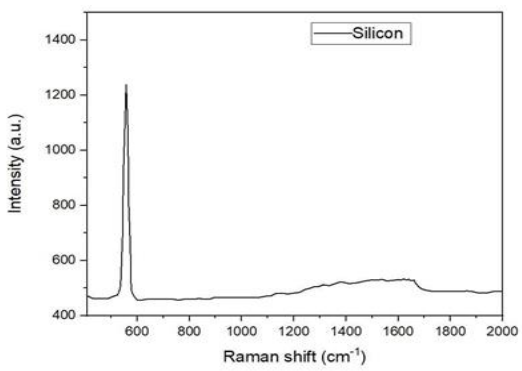

Raman Spectroscopy for (S1)

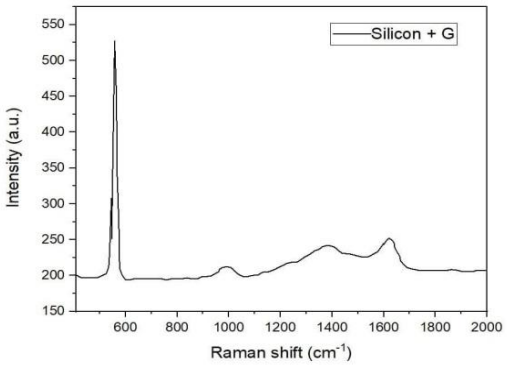

Raman Spectroscopy for (S2)

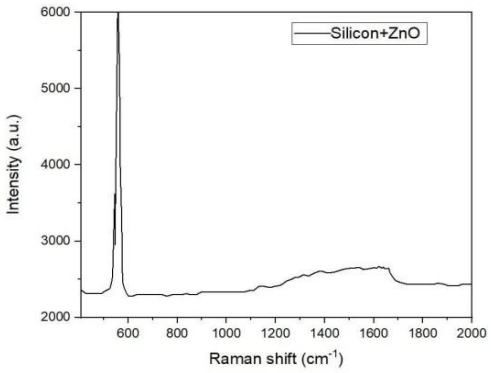

Raman Spectroscopy for (S3)

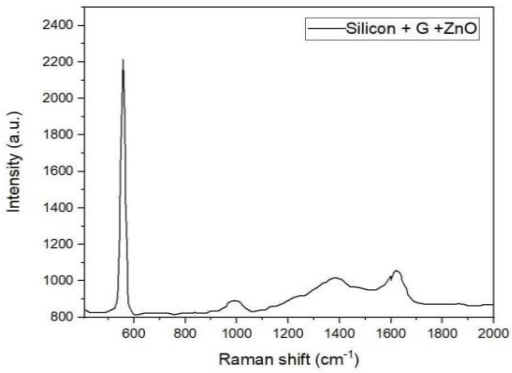

Raman Spectroscopy for (S4)

Fig. (4-5) Raman Spectroscopy for S1, S2, S3, and S4 at 500Pulse.

4.3 Optical properties

The study of the optical properties of the films is of great importance in finding the optical constants through which it is possible to know the value of the optical energy gap from the reflectance by using the Kubelka-Munk theory.

4.3.1 Reflectance (R)

The reflectance of silicon oxide nanowires (SiO NWs) depends on a variety of factors, including the diameter and length of the nanowires, the incident angle and polarization of light, and the refractive indices of the surrounding media.

SiO NWs exhibit lower reflectance compared to bulk silicon due to their enhanced light trapping and absorption properties. The increased surface area of the nanowires allows for multiple total internal reflections, which leads to a longer optical path and higher absorption of light. Additionally, the nanowire diameter of about 100 nm as in the SEM images can match the resonant wavelength of the incident light, resulting in even higher absorption.

However, the reflectance of Si ONWs can also be affected by surface roughness, contamination, and other structural defects that can scatter or reflect light.

From the observations in Figure (4-6), Si ONWs exhibit reflectivity in the ultraviolet (UV) region at 28%, and in the visible light range of 600-1000 nm, it increases from 3% to 10%. When graphene is added, the reflectance in the UV region increases by 42%, and in the visible light range, it increases significantly from 3% to 15%. In the infrared range, it increases from 15% to 30%. The same behavior is observed when zinc oxide (ZnO) is added. The UV reflectance increases to 75%, and in the visible region at 550 nm, it is 15%, and at 1000 nm, it is 30%. When graphene and ZnO are added to Si ONWs, the UV reflectance is 60%, the visible region is 25%, and at 1000 nm, it is 100%.

The increased reflectance of SiO NWs in the visible light range when graphene is added can be linked to the increased surface area of the nanowires. This is because graphene is a highly conductive material, and it can help to reduce the surface roughness of the nanowires.

The increased reflectance of SiO NWs in the UV and infrared ranges when ZnO is added can be linked to the higher refractive index of ZnO. This means that more light is reflected from the surface of the nanowires, resulting in a higher reflectance. The XRD results show that the addition of graphene and ZnO to SiO NWs can cause the nanowires to become

more strained. This strain can also contribute to the increased reflectance of the nanowires, as it can lead to the formation of localized surface plasmon resonances.

The reflectance results provide further evidence of the impact of graphene and zinc oxide additions on the optical properties of SiO NWs. The enhanced reflectivity in specific regions can be attributed to the improved light trapping, absorption, and modifications in surface properties brought about by the presence of graphene and zinc oxide in the SiONWs system.

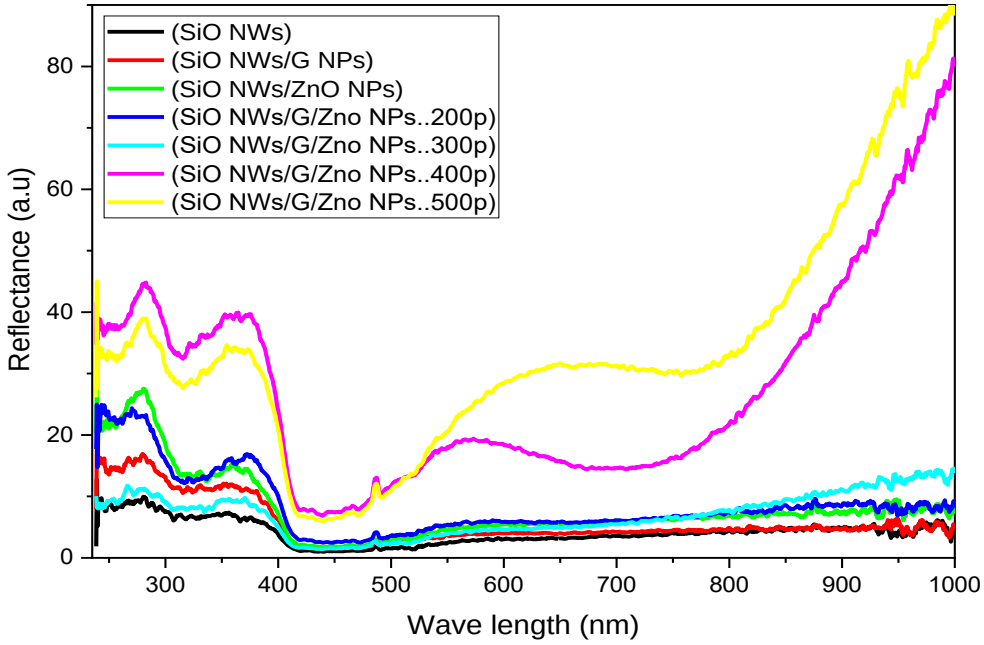

Fig. (4-6) The reflectivity as a function of the wavelength for all the prepared devices .

4.3.2 Optical Energy Gap (Eg)

The band gap of silicon oxide nanowires (SiONWs) is a critical property that determines their optical and electronic properties. The band gap of SiONWs can vary depending on several factors, such as the diameter, length, and surface properties of the nanowires, as well as the preparation method. Previous experimental studies have reported band

gap values for SiONWs ranging from approximately 1.5 eV to 3.5 eV [122,137].

In this study, we investigated the effect of different materials on the energy gap of SiONWs. We used the Kubelka-Munk theory, as described by Equation (2.4) in chapter 2, to measure the direct and indirect energy gap function for SiONWs alone, as well as for samples with added graphene, zinc oxide, and a ternary compound.

Figure (4-7) presents the energy gap plots for the different samples. Table (4-4) summarizes the direct and indirect energy gap values obtained for each sample. It is observed that the direct band gap of the SiO NWs was (3.03 eV, 3.06 eV, 3.06 eV, 3.05 eV, and 3.05 eV, 3.1 eV, 3.1 eV),respectively, for the samples with (SiO NWs, SiONWs/G NPs, SiONWs/ZnO NPs, and the composite (SiONWs/G/ZnO NPs at 500p,400p,300p,200p). The indirect band gap of the SiO NWs was(3.03 eV, 3.04 eV, 3.04 eV, 3.04 eV, 3.0 eV, 3.02 eV, and 3.04 eV), respectively, for the same samples.

Our results revealed that the energy gap of SiO NWs was not significantly influenced by the addition of graphene or zinc oxide, nor by the ternary compound. Specifically, the direct and indirect energy gap values for the seven samples were found to be similar, indicating that the silicon nanowire base is dominant and that the graphene and zinc oxide layers are thin nanolayers that do not significantly impact the energy gap of SiO NWs [122,137].

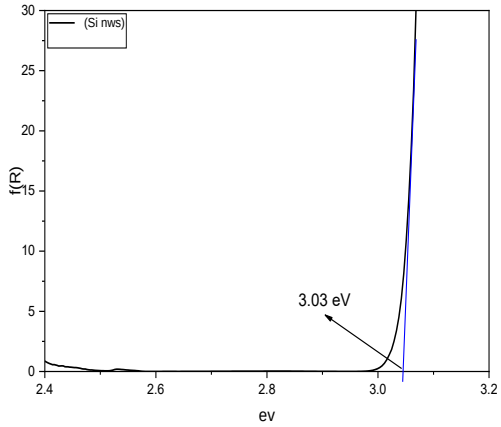

SiO NWs Direct

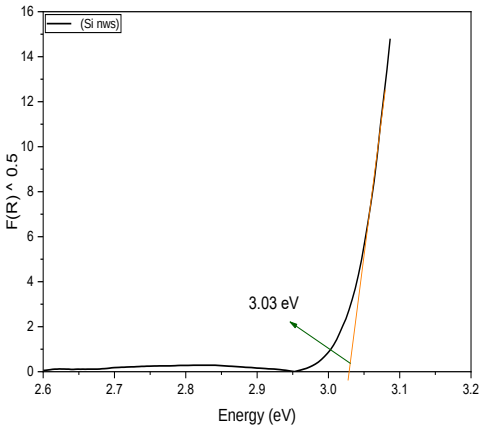

SiO NWs Indirect

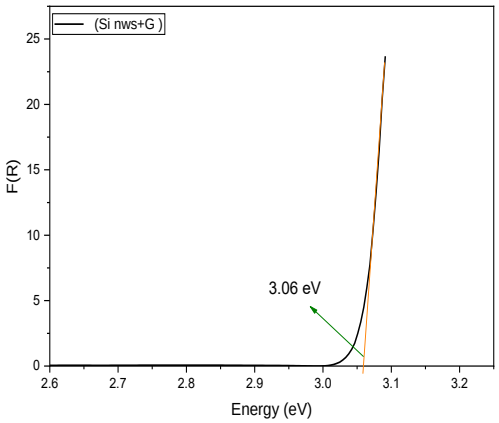

SiO NWs /G NPs Direct

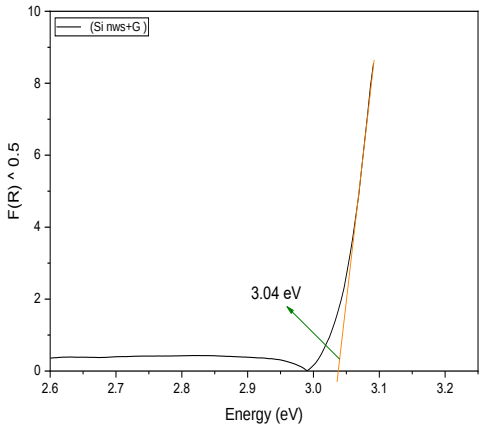

SiO NWs/G NPs Indirect

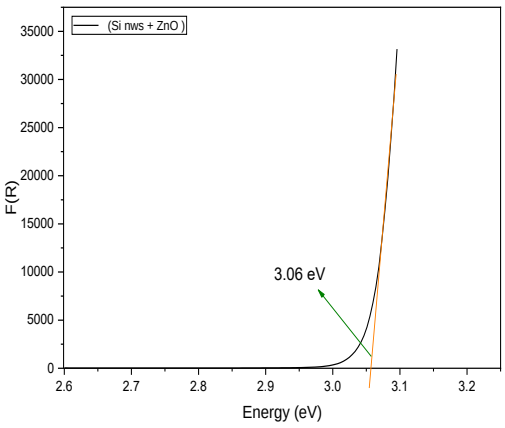

SiO NWs /ZnO NPs Direct

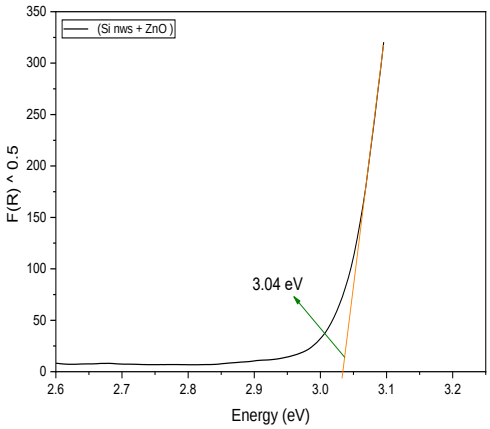

SiO NWs /ZnO NPs Indirect

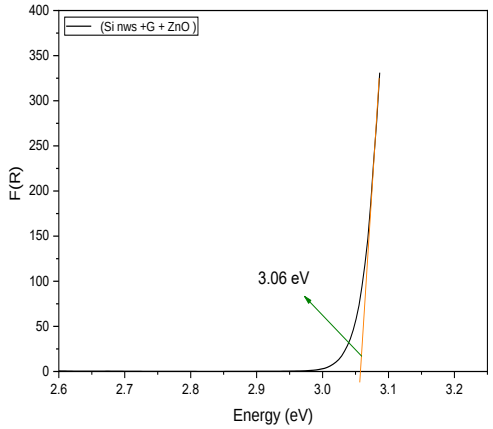

SiO NWs /G /ZnO NPs(500p) Direct

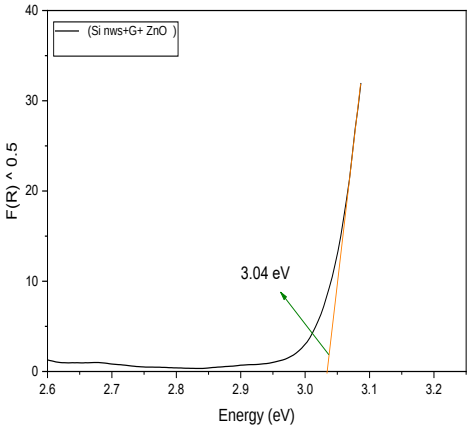

SiO NWs /G /ZnO NPs(500p) Indirect

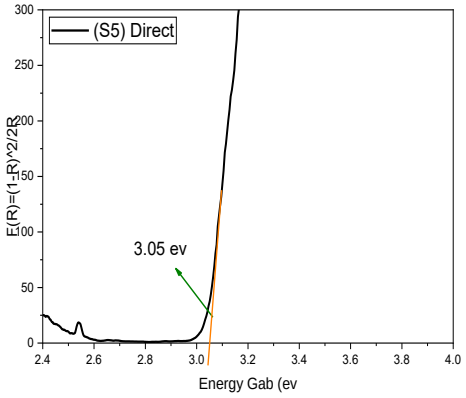

SiO NWs /G /ZnO NPs(400p) Direct

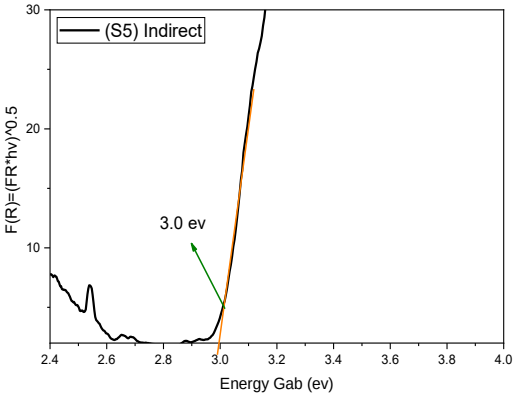

SiO NWs /G /ZnO NPs(400p) Indirect

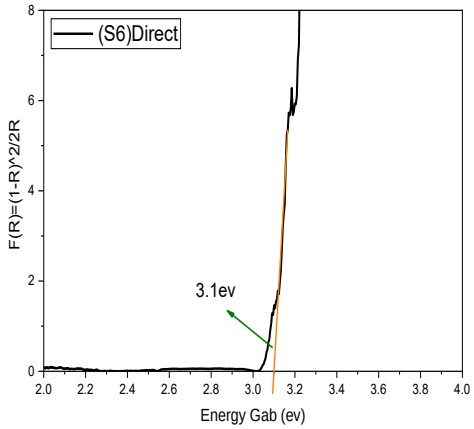

SiO NWs /G /ZnO NPs(300p) Direct

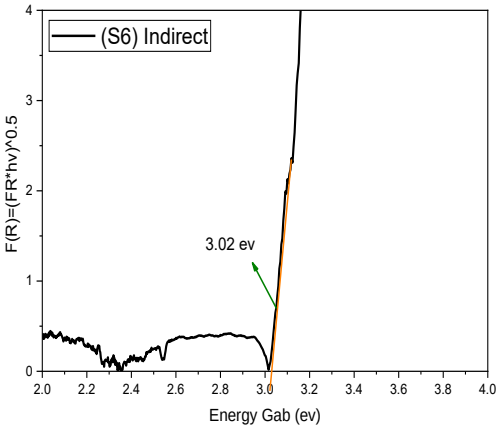

SiO NWs /G /ZnO NPs(300p) Indirect

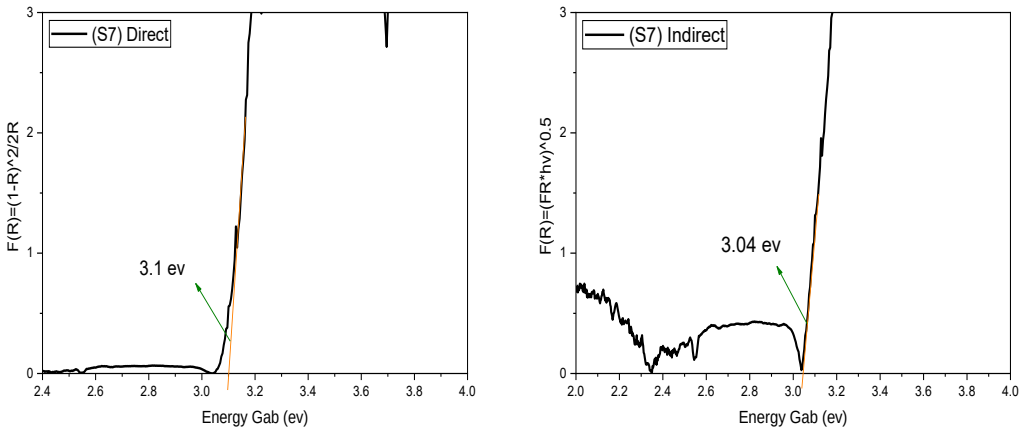

SiO NWs /G /ZnO NPs(200p) Direct **SiO NWs /G /ZnO NPs(200p) Indirect**

Fig. (4-7) The Energy Gap as a function of the wavelength for all the prepared devices.

Our findings have important implications for the development of SiO NWs-based devices, particularly in the fields of electronics, photonics, and energy conversion. By understanding the factors that influence the band gap of SiO NWs, researchers can design and optimize the properties of these materials for specific applications. Furthermore, our results suggest that SiO NWs combined with other materials, such as graphene and zinc oxide, may offer new opportunities for developing advanced nanomaterials with novel properties and potential applications in various fields.

Table (4-4) Energy Gap Values

Samples	E_g (eV) Direct	E_g (eV) Indirect
SiO NWS	3.03	3.03
SiO NWS/ G NPs	3.06	3.04
SiO NWS / ZnO NPs	3.06	3.04
SiO NWS / G/ ZnO NPs (500p)	3.05	3.04
SiO NWS / G/ ZnO NPs (400P)	3.05	3.0

SiO NWS / G/ ZnO NPs (300P)	3.1	3.02
SiO NWS / G/ ZnO NPs (200P)	3.1	3.04

4.4 Electrical Properties (Hall Effect Measurements):

Table(6.5) provides a comprehensive overview of the electrical characteristics of four distinct silicon-based samples, labeled as SiO NWs, SiO NWs/G NPs, SiO NWs/ZnO NPs, and SiO NWs/G/ZnO NPs.

Starting with SiO NWs, this sample exhibits a resistivity of $1.17x10^{-2}$ Ω.cm, a carrier concentration of $6.00x10^{17}$ cm^{-3}, a Hall coefficient of $1.04x10^{1}$ $cm^{3}C^{-1}$, a conductivity of $8.54x10^{1}$ $Ω^{-1}.cm^{-1}$, and a mobility of $8.88x10^{2}$ $cm^{2}V^{-1}s^{-1}$. It demonstrates a P-type carrier type.

Moving to SiO NWs/G NPs, this sample displays higher resistivity at $1.13x10^{-1}$ Ω.cm and an elevated carrier concentration of $8.61x10^{17}$ cm^{-3}. However, its Hall coefficient decreases to 7.25 $cm^{3}C^{-1}$, accompanied by a lower conductivity of 8.83 $Ω^{-1}.cm^{-1}$ and mobility of $6.4x10^{1}$ $cm^{2}V^{-1}s^{-1}$. It remains P-type in terms of carrier type.

SiO NWs/ZnO NPs exhibits a resistivity of $1.51x10^{-2}$ Ω.cm, coupled with a higher carrier concentration of $3.04x10^{18}$ cm^{-3}. Its Hall coefficient diminishes to 2.05 $cm^{3}C^{-1}$, while its conductivity increases to $6.63x10^{1}$ $Ω^{-1}.cm^{-1}$ and mobility rises to $1.36x10^{2}$ $cm^{2}V^{-1}s^{-1}$. It also maintains a P-type carrier type.

The sample SiO NWs/G/ZnO NPs emerges with the lowest resistivity of the group, measuring $1.13x10^{-2}$ Ω.cm, and boasts the highest carrier concentration at $3.92x10^{18}$ cm^{-3}. It exhibits a reduced Hall coefficient of 1.59 $cm^{3}C^{-1}$, while its conductivity soars to $8.87x10^{1}$ $Ω^{-1}.cm^{-1}$, along with a higher mobility of $1.41x10^{2}$ $cm^{2}V^{-1}s^{-1}$. It maintains a P-type carrier type, similar to the others.

Analyzing these findings, it's evident that the inclusion of graphene or ZnO in SiO NWs brings about notable alterations in their electrical characteristics. Introducing graphene leads to elevated carrier concentration and resistivity, along with reduced conductivity, mobility, and Hall coefficient. Conversely, the addition of ZnO contributes to higher carrier concentration, conductivity, and mobility, coupled with reduced resistivity and Hall coefficient.

Furthermore, the incorporation of both graphene and ZnO yields a sample with the most favorable electrical attributes: lowest resistivity, highest carrier concentration, conductivity, and mobility. Despite this enhancement, its Hall coefficient remains lower than that of SiO NWs alone. All samples maintain a P-type carrier type, indicating the prevalence of holes as charge carriers.

Table (4.5) Hall parameters for films at room temperature.

Sample Name	Resistivity ρ(Ω.cm)	Concentration of Carriers n_H cm^{-3}	Hall Coefficient RH (cm^3C^{-1})	Conductivity $\sigma(\Omega.cm)^{-1}$	Mobility μH ($cm^2V^{-1}s^{-1}$)	Type of Carriers
S1	1.17E-02	6.00E+17	1.04E+01	8.54E+01	8.88E+02	P
S2	1.13E-01	8.61E+17	7.25E+00	8.83E+00	6.40E+01	P
S3	1.51E-02	3.04E+18	2.05E+00	6.63E+01	1.36E+02	P
S4	1.13E-02	3.92E+18	1.59E+00	8.87E+01	1.41E+02	P

4.5 Applications

4.5.1 Optoelectronic Detector :

A. Spectral responsivity (Rλ)

An important merit of the photodetector is its photo responsivity, which measures the electrical response of the device to incident photons. The photo responsivity is given by equation (2). Figure (4-8) illustrates the responsivity as a function of wavelength for all the prepared devices. The figure clearly indicates that the responsivity increases when SiO NWS, G, and ZnO are combined, reaching a maximum at a wavelength of 800 nm. Specifically, the responsivity improves from 0.40 A/W for SiO NWS to 0.34 A/W for SiO NWS/G, 0.46 A/W for SiO NWS/ZnO, and 0.79 A/W for SiO NWS/G-ZnO device.

However, it is worth noting that the photoresponse of the photodetector for all the prepared devices covers the entire visible and near-infrared region but exhibits a lower response in the UV range. This increase in photoresponse can be attributed to the interaction between the nanocomposite and the electrons in Graphene NPS, which are captured by Silicon Oxide and Zinc Oxide ions through Coulomb interactions, resulting in the formation of Ion−Electron Bound States (IEBSs). Under illumination, all the (IEBSs) can be dissociated by absorbing photon energy, thereby significantly enhancing the photoresponse performance of the nanocomposite optoelectronic devices, as confirmed by the SEM analysis. Consequently, these nanocomposites are well-suited for visible and near-infrared detector applications. This behavior aligns with previous studies [129].

Measurements of the photodetector's properties on thin films indicate that all the samples operate effectively in the Vis-IR region, specifically within the wavelength range of 750-950 nm. However, samples S1 and S2 exhibit lower responses in the UV region at a wavelength of 350 nm. This trend is also observed in terms of detectivity and quantum efficiency.

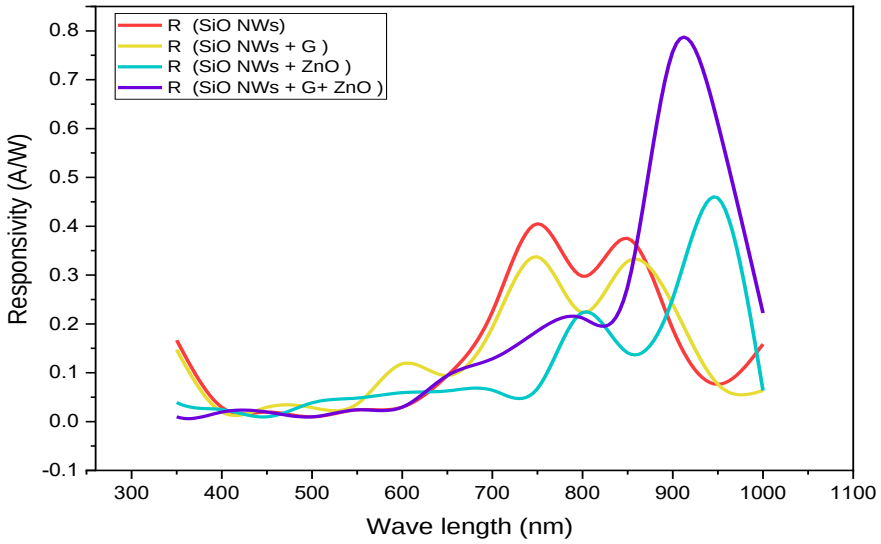

Fig. (4-8) The responsivity spectra as a function of the wavelength for all the prepared devices.

B. Specific detectivity (D_λ)

Another important parameter of optoelectronic detectors is detectivity, as in equation (4). Figure (4-9) illustrates the detectivity as a function of wavelength for all the prepared devices.

From Figure (4-9), a clear relationship between detectivity and responsivity is observed. Similar behavior is obtained, where the detectivity increases when SiO NWS, G, and ZnO NPS are combined. Specifically, the detectivity improves from 18.41×10^6 cm·Hz$^{1/2}$·W^{-1} for SiO NWS to 15.50×10^6 cm·Hz$^{1/2}$·W^{-1} for SiO NWS/G, 20.98×10^6 cm·Hz$^{1/2}$·W^{-1} for SiO NWS/ZnO, and 35.68×10^6 cm·Hz$^{1/2}$·W^{-1} for SiO NWS/G, ZnO device within the wavelength range of 700-1000 nm. Additionally, the specific detectivity increases from SiO NWS to SiO NWS/G, ZnO NPS device at a wavelength of 350 nm.

The higher responsivity directly leads to higher detectivity. The most common built-in noise within the detector is white noise, Johnson noise,

and thermal noise, which result from the random motion of current carriers within any resistive material. Another significant source of noise is generation-recombination noise, arising from the presence of defects acting as trapping centers. These results align with previous studies [130].

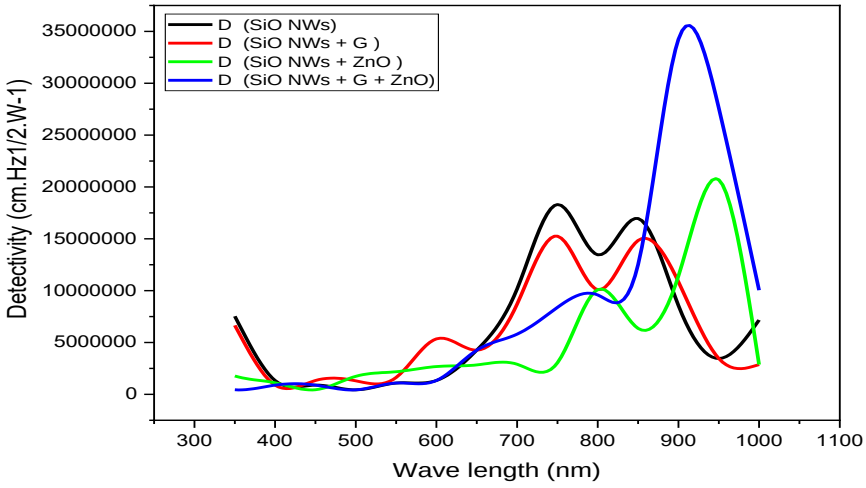

Fig. (4-9) The detectivity spectra as a function of the wavelength for all the prepared devices.

C. The Quantum efficiency (QE)

Figure (4-10) shows the detector's quantum efficiency as a function of wavelength, as given by Equation (3). The figure shows that the quantum efficiency is 67.42% for SiO NWs, which increases when G and ZnO NPS are added to SiO NWs. The quantum efficiency is 56.85% for SiO NWS/G NPs and the value of 60.74% for SiO NWS/ZnO NPs. Where The highest quantum efficiency is observed for the triple compound, with a value of 107.43% at a wavelength of 700-1000 nm.

The higher responsivity results in higher quantum efficiency. This is because the responsivity is a measure of the electrical response of the detector to incident photons, and the quantum efficiency is a measure of the fraction of incident photons that are converted into electrical current.

The highly effective collection of charge carriers photogenerated in SiO NWS is attributed to the nanocomposite devices.

The main goal of this research is to improve the speed of silicon-based photodetectors. To achieve this, we have tried to produce a nanocomposite that offers higher electron mobility and lower resistance. Wrapping G NPs with ZnO NPs seems to be the best solution for this challenge, as it results in high electron density and mobility, as confirmed by Hall effect measurements. This result is in agreement with previous studies [131].

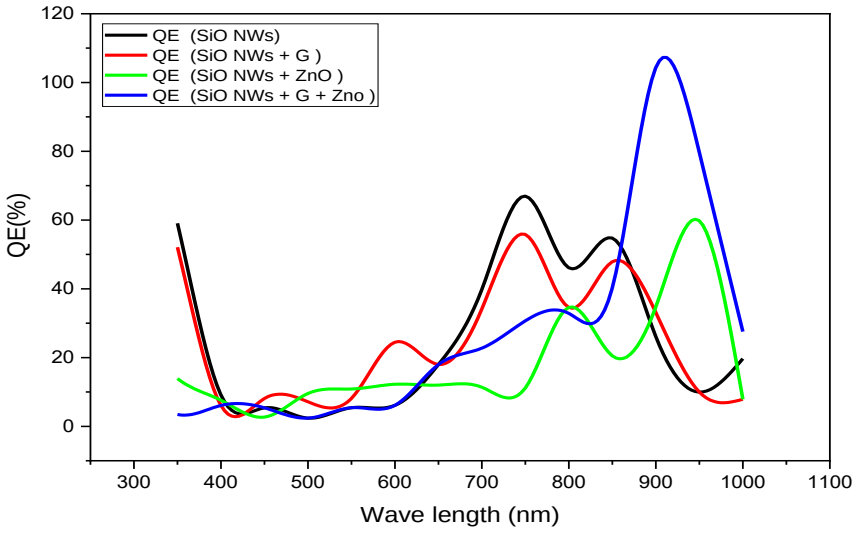

Fig. (4-10) The quantum efficiency spectra as a function of the wavelength for all the prepared devices.

From Table (4-6), shows that the responsivity, detectivity, and quantum efficiency all increase when graphene and zinc oxide nanoparticles are added to the silicon nanowire device. This is because the graphene and zinc oxide nanoparticles improve the collection of charge carriers in the device. The SiO NWS/G, ZnO NPs device exhibits the highest responsivity (0.79A/W), detectivity (35.68 x10^{6} cm.$Hz^{1/2}$.W^{-1}), and quantum efficiency (107.43%) at 900 nm. This indicates that this device configuration is most effective in converting incident photons into

an electrical signal with high sensitivity and efficiency at the given wavelength.

Comparatively, the SiO NWS device has lower responsivity, detectivity, and quantum efficiency values. These results suggest that the Si NWS/G-ZnO NPs device is the most sensitive of the four devices. It is also the most efficient at converting incident photons into electrical current.

Table (4-6) The result of the responsivity, detectivity and quantum efficiency for all the prepared devices at 900 nm for S1,S2, S3, and S4.

Device type	λ (nm)	Responsivity (A/W)	Detectivity $*10^6$(cm.$Hz^{1/2}$.W^{-1})	Quantum Efficiency (%)
SiO NWS	**750**	**0.40**	**18.41**	**67.42**
SiO NWS/G NPs	**750**	**0.34**	**15.50**	**56.85**
SiO NWS/ZnO NPs	**950**	**0.46**	**20.98**	**60.74**
SiO NWS/G/ZnO NPs	**900**	**0.79**	**35.68**	**107.43**

The Table (4-7) compares the quantum efficiency, responsivity, detectivity, and wavelength of our study to other reports in the literature. The table shows that our study has the highest quantum efficiency and detectivity of all the reports. The responsivity of our study is also comparable to the other reports.

The wavelength of our study is in the visible and near-infrared region, which is a desirable range for many applications. The other reports in the table have wavelengths in the visible, near-infrared, and ultraviolet regions.

The Table also shows that the responsivity, detectivity, and quantum efficiency of our study increase when graphene and zinc oxide nanoparticles are added to the silicon oxide nanowire device. This is

consistent with the results of our study, which showed that the addition of graphene and zinc oxide nanoparticles improves the collection of charge carriers in the device.

the results of our study are promising and suggest that your device has the potential to be a high-performance photodetector.

Table (4-7) Shows Performance comparison of devices photodetector [132].

Devices structure	manufacturing method	Quantum efficiency(%)	Responsivity (A/W)	D* (cm $Hz^{1/2}$/W)	λ (nm)	Ref.
G/ZnO/n-Si photodetector Practical study	a self-powered photo detector	–	0.5	$3.9*10^{13}$	488	[30]
p-Si / graphene / n-ZnO photodetector Practical study	hydrothermal method and chemical vapor deposition	– sensitivity 1071	–	–	365	[31]
p^+-BLG / n^+-ZnO NWs	theoretical study by The Silvaco Atlas TCAD software, analytical modeling	56 @ 350 nm, 4.7 @ 480 nm, 2.11 @580 nm 1.6 @ 800 nm	0.16	$2.44*10^9$	350	[32]
p^+-BLG / n^+-Si NWs / p^--si		50 @ 350 nm, 46.86 @ 480nm, 50 @ 580 nm, 15.2 @ 800nm	0.23	$1.26*10^{11}$	580	
p^+-BLG / n^+-ZnO NWs / p^--si		71 @350 nm, 71 @ 480 nm, 41.68 @ 580nm, 9.6 @ 800 nm	0.28	$4.2*10^{12}$	480	
SiO NWS	Practical study by Chemical etching and PLD	67.42	0.4	$18.3*10^6$	750	**Our study**
SiO NWS/G NPs		56.85	0.34	$15.25*10^6$	750	
SiO NWS/ZnO NPs		60.74	0.46	$20.69*10^6$	950	
SiO NWS/G,ZnO NPs		107.43	0.79	$34.25*10^6$	900,	

4.5.2 Optical Sensing(Solar Cell): I-V Characteristics Heterojunction in Light and Dark

In this section, the current-voltage measurements have been used to determine the electrical properties of films, The study of current-voltage

properties in the light and dark case is important because it clearly indicates the possibility of using these films as a photosensor.

To determine photocurrent in (μA) unit of the composite films, The current-voltage(I-V) characteristics of the films under illumination conditions have been studied for forward and reverse biases, and dark and illumination for reverse biases.

Figures (4.13), and (4.14) show (I-V) characteristics for SiO NWs /ZnO NPs, SiO NWs/G/ZnO NPs..500p heterojunction under light with various forward and reverse bias voltages where the effect of light is clear in changing the current values for prepared samples. From this Figures, it can be observed that the values of photocurrent increase with an increase in the applied voltage in the light case which is attributed to the increase of the charge carriers.

For the SiO NWs/G/ZnO NPs..500p heterojunction under illumination at reverse bias, the width of the depletion region increases with the increase of the applied voltage which leads to an increase in the absorption through it and the creation of the electron-hole pairs.

Therefore, the current flow across the junction will be increased. which shows that the illumination current increases with an increase in the applied voltage Also the values for forward current in the illumination state are 0.4μA, 1.2μA, 0.8μA and 0.6μA for SiO NWs, SiO NWs /G NPs, SiO NWs /ZnO NPs, SiO NWs/G/ZnO NPs..500p composite films respectively.

In the case of Si NWs in Figure (4.11), the behavior varies slightly so that the amount of current remains constant almost until it reaches the applied voltage of more than 2Volt and starts to increase. It can be seen from this Figure also that the curve exhibits a non-linear feature,

indicating that the conduction mechanism is non-ohmic.as An increase in the current may be observed after adding Graphene and Zinc Oxide to the Silicon Oxide Nanowire substrate.

Figures (4.11), (4.12), (4.13), and (4.14) for SiO NWs, SiO NWs /G NPs, SiO NWs /ZnO NPs, SiO NWs/G/ZnO NPs..500p composite films respectively, show current increases of films with illumination lamp intensity of 100 mWcm-2, with an active area about (0.56 cm2). In the same way that the forward current increases so does the reverse current, which increases with add (G, ZnO NPs).

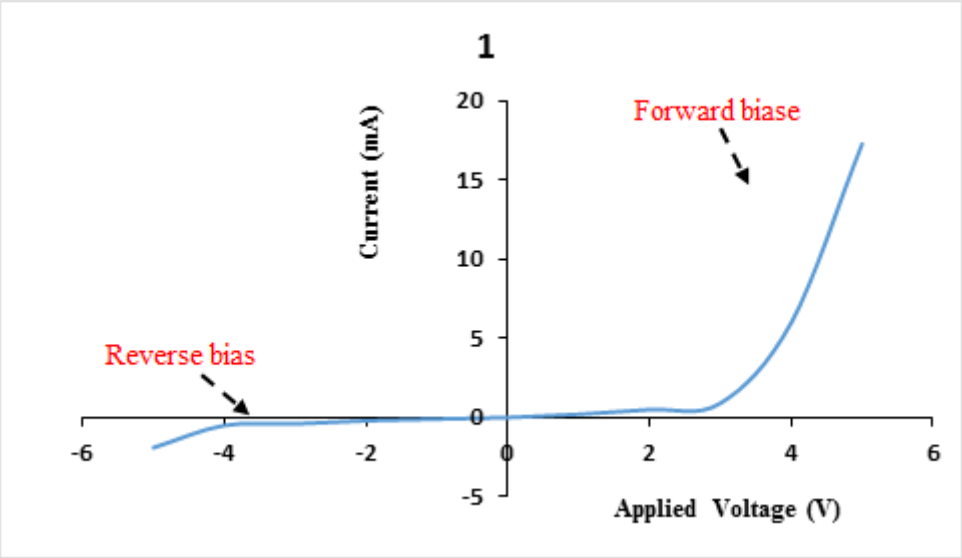

Fig. (4-11) I-V Characteristics in Light of SiO NWs (p-type) for forward and reverse bias.

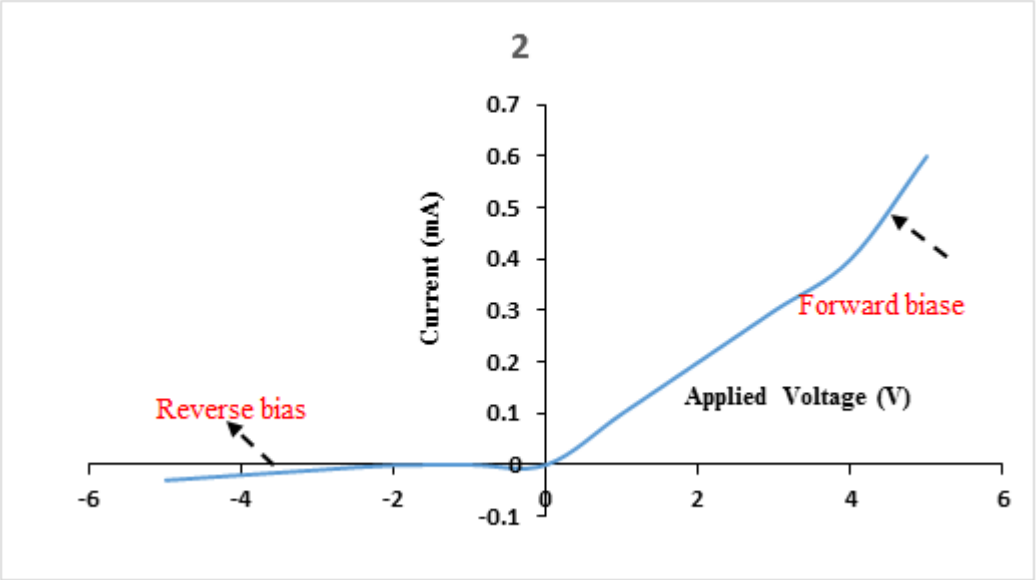

Fig. (4-12) I-V Characteristics in Light of SiO NWs(p-type)/G for forward and reverse bias.

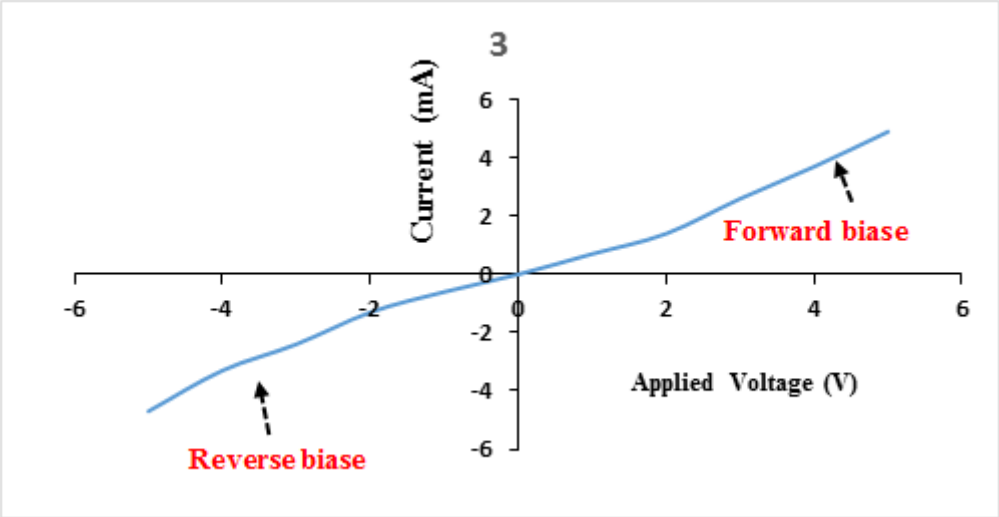

Fig. (4-13) I-V Characteristics in Light of SiO NWs (p-type)/ZnO(n-type) NPs for forward and reverse bias.

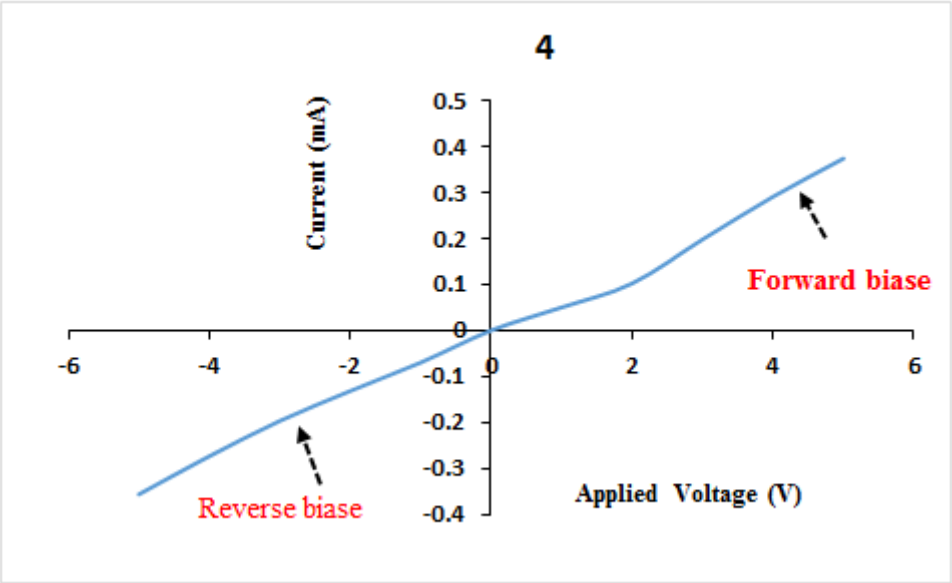

Fig. (4-14) I-V Characteristics in Light of SiO NWs(p-type)/G /ZnO (n-type) NPs for forward and reverse bias.

Figures (4-15, 4-16,4-17,and 4-18) exhibit the reverse current as a function of applied voltage in dark and light for SiO NWs, SiO NWs /G NPs, SiO NWs /ZnO NPs, SiO NWs/G/ZnO NPs..500p heterojunction. The results showed that the values of current increase with the increase of the applied reverse voltage due to the change in doping ratios and this behavior are similar to what we observed in the forward bias.

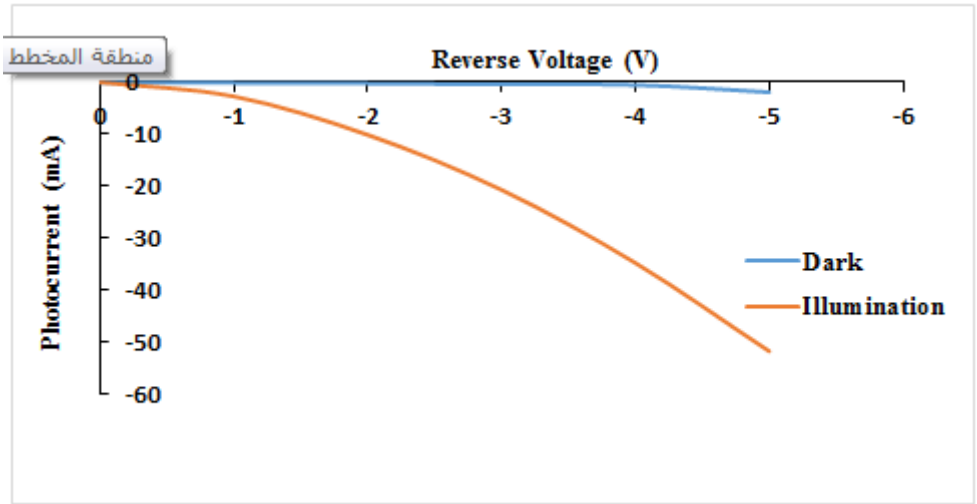

Fig. (4-15) I-V Characteristics in Dark and Light of SiO NWs and reverse bias.

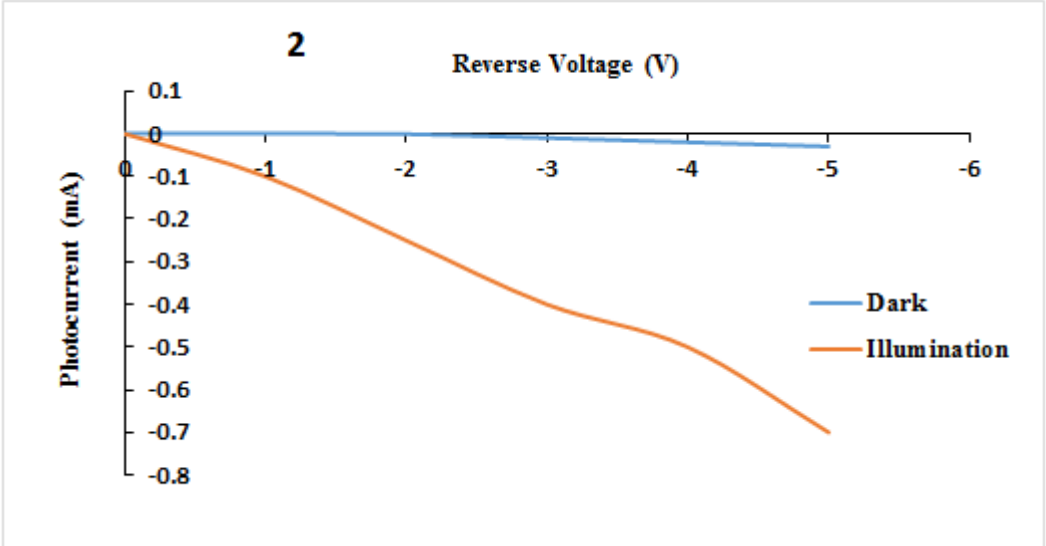

Fig. (4-16) I-V Characteristics in Dark and Light of SiO NWs/G NPs for reverse bias.

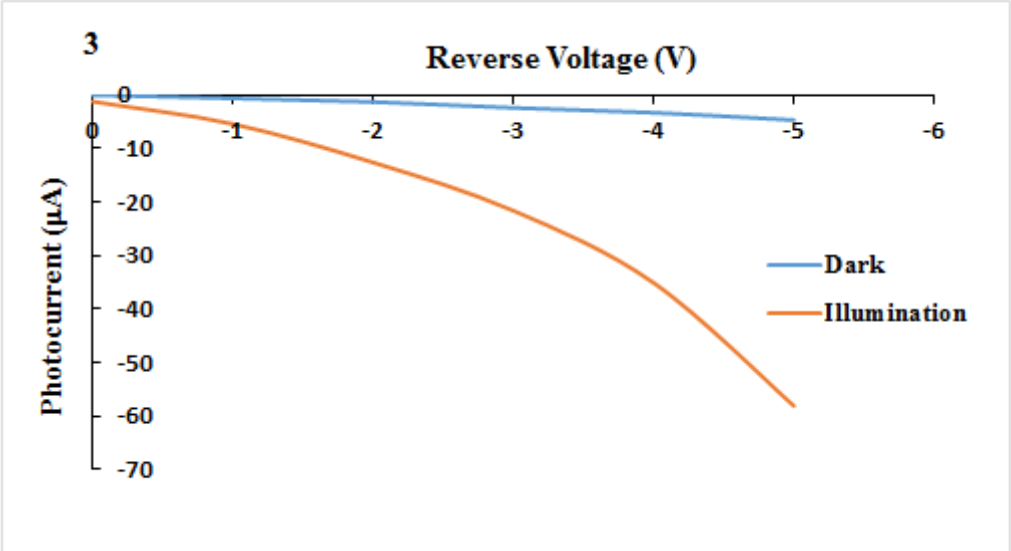

Fig. (4-17) I-V Characteristics in Dark and Light of SiO NWs/ZnO NPs for reverse bias.

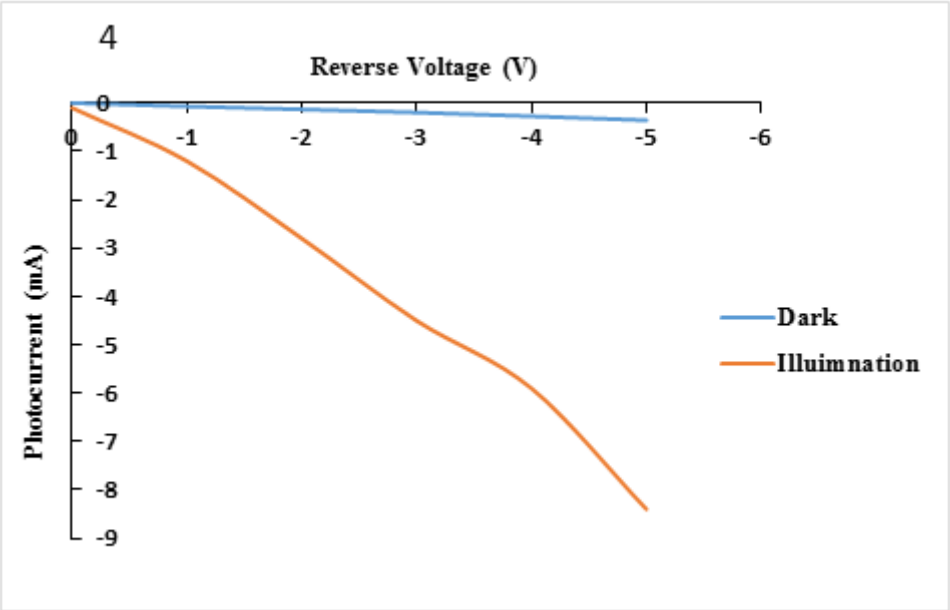

Fig.(4-18) I-V Characteristics in Dark and bright of SiO NWs/G /ZnO NPs for reverse bias

The values of solar cell parameters of (V_{oc}, I_{sc}, V_{max}, I_{max}, F.F and η) which represent the maximum open circuit voltage, short-circuit current, maximum voltage, maximum current ,the fill factor, and the efficiency of the solar cell respectively under the illumination condition, of SiO NWs, SiO NWs /G NPs, SiO NWs /ZnO NPs, SiO NWs/G/ZnO NPs..500p heterojunction were arranged in Table (4.8). The fill factor and efficiency can be calculated from equations (2.35) and (2.36) respectively. In general, it can be observed that the maximum efficiency value was (0.016 %) for (SiO NWs / G/ ZnO NPs) sample, while the lowest value was (0.010 %) for (SiO NWs /G NPs) sample.

Table (4.8) Measured and calculated values of four junctions

Solar cell Samples	V_{Oc} (mV)	I_{Sc} (μA)	V_m (mV)	I_m (μA)	F.F %	η%
SiO NWs	87	0.4	55	0.25	39.51	0.013
SiO NWs /G NPs	66	0.6	34	0.3	26.51	0.010
SiO NWs / ZnO NPs	80	0.8	35	0.36	19.68	0.012
SiO NWs / G/ ZnO NPs	56	1.2	28	0.6	25	0.016

4.6 Conclusions

This research is successfully synthesized and characterized SiO NWs/Graphene and ZnO NPs hybrid nanostructures by using pulsed laser deposition (PLD). The crystalline, morphology, Raman spectroscopy, and optical properties (reflectance and energy gap) of the synthesized hybrid nanostructure systems were characterized.

The XRD results showed that the addition of GO and ZnO to the SiO NWs did not significantly affect the hexagonal structure of the thin films. There was a slight displacement in the locations of some characteristic peaks, which is likely due to the formation of chemical compounds between SiO, GO, and ZnO.

The results of AFM showed that the lowest values were obtained for the SiO NWs sample, with RMS roughness and average particle size of 1.44 nm and 15.39 nm, respectively. The highest value for the root mean square (RMS) roughness and average particle size were recorded at 6.20 nm and 40.45 nm, respectively, for the SiO NWs/G-ZnO 500 Pulse sample.

The results of SEM aligned with the findings from the AFM measurements, indicating that the introduction of graphene and ZnO nanoparticles onto the SiO NWs substrate resulted in significant changes in the surface topography of the films. The presence of the graphene layer appears to have smoothened the surface of the silicon oxide nanowires, while the ZnO nanoparticles contribute to the creation of a rougher surface. The addition of graphene and ZnO nanoparticles together led to increased roughness values and a reduction in average particle size. The enhancement of the hexagonal structure observed in the SiO NWs/G, ZnO films, characterized by higher G and ZnO ratios, is consistent with the XRD results.

The Raman spectroscopy results showed that upon the addition of ZnO to SiO NWs/GO, the G/D ratio increases resulting in a value of 1.2. This indicates that the addition of ZnO leads to increased orderliness in the GO lattice. Additionally, the Raman spectrum of GO shows the presence of a peak around 1600 cm-1, commonly observed in the Raman spectrum of graphene, which suggests the possibility of a coating layer of reduced graphene oxide (RGO) on SiO NWs.

The optical properties (reflectance and energy gap) showed that SiONWs exhibit lower reflectance than bulk silicon due to their enhanced light trapping and absorption properties. The addition of graphene and zinc oxide to SiONWs enhances the reflectivity in specific regions, including the UV and visible ranges, due to improved light trapping, absorption, and modifications in surface properties.

The energy gap of SiO NWs was not significantly influenced by the addition of graphene or zinc oxide, nor by the ternary compound. Specifically, the direct and indirect energy gap values for the four samples were found to be similar, indicating that the silicon nanowire base is dominant and that the graphene and zinc oxide layers are thin nanolayers that do not significantly impact the energy gap of SiO NWs.

The photodetector based on the hybrid nanostructure systems was fabricated. The responsivity, detectivity, and quantitative efficiency of the photodetector were calculated, and the results showed that the photodetector has excellent performance. The study has the highest quantum efficiency and detectivity of all the reports. The responsivity of this study is also comparable to the other reports.

The responsivity, detectivity, and quantum efficiency of this study increase when graphene and zinc oxide nanoparticles are added to the silicon oxide nanowire device, which showed that the addition of graphene and zinc oxide nanoparticles improves the collection of charge

carriers in the device. The wavelength used in this study is in the visible and near-infrared region, which is a desirable range for many applications.

This study provides a promising platform for the development of next-generation optoelectronic devices with broad spectral detection and high quantitative efficiency. It is expected to contribute to the advancement of various fields, including security, environmental monitoring, and medical diagnostics.

(References)

1. Schwarz, James A., Cristian I. Contescu, and Karol Putyera, eds. Dekker encyclopedia of nanoscience and nanotechnology. Vol. 5. CRC press, 2004.
2. Murty, Budaraju S., et al. Textbook of nanoscience and nanotechnology. Springer Science & Business Media, 2013.
3. Das, I., and Ansari, S. A., " Nanomatirials in Science and technology" . of Scientific and industrial research, Vol. 68, 2009.
4. Roduner, E., "Size matters: why nanomaterials are different." Chemical Society Reviews, Vol. 35, No. 7, pp. 83-592, 2006.
5. Ismail, M., Gul, S., Khan, M. A., and Khan, M. I. "Plant Mediated Green Synthesis of Anti-Microbial Silver Nanoparticles—A Review on Recent Trends", Reviews in Nanoscience and Nanotechnology, Vol. 5, No. 2, pp. 119-135, 2016.
6. Rao, C. N. R., Müller, A., and Cheetham, A. K., (Eds.), " The Chemistry of Nanomaterials: Synthesis, Properties and Applications". John Wiley and Sons, 2006.
7. Murthy, M. K., and ErBedre Heeramani, E. N., "Advanced Challenges of Nano Technology Based Accounting." Icrismet-2016, August, ISBN , p.p. 978-93, 2016.
8. Dr. Abdullah Al-Dwayyan and Dr. Mohammed bin Saleh Al-Salhi, "Introduction to Nanotechnology", Department of Physics Astronomy, King Saud University, King Saud University Press, 2007.
9. Rodríguez, J. A., and Fernández-García, M. (Eds.), “Synthesis, properties, and applications of oxide nanomaterials”. John Wiley & Sons, 2007.
10. Okuda, Mitsuhiro, et al. "Top-down design of magnonic crystals from bottom-up magnetic nanoparticles through protein arrays." Nanotechnology 28.15 (2017): 155301.
11. Ealia, S. Anu Mary, and M. P. Saravanakumar. "A review on the classification, characterisation, synthesis of nanoparticles and their application." IOP conference series: materials science and engineering. Vol. 263. No. 3. IOP Publishing, 2017.
12. Yokoyama, T., Masuda, H., Suzuki, M., Ehara, K., Nogi, K., Fuji, M., and Toda, K, "Basic Properties And Measuring Methods Of Nanoparticles", ELSEVIER, Nanoparticle Technology Handbook, p.p. 3-48 , 2008.
13. Ghosh Chaudhuri, Rajib, and Santanu Paria. "Core/shell nanoparticles: classes, properties, synthesis mechanisms, characterization, and applications." Chemical reviews 112.4 (2012): 2373-2433.
14. Marinescu, Liliana, et al. "Optimized synthesis approaches of metal nanoparticles with antimicrobial applications." Journal of Nanomaterials 2020 (2020).
15. Abdalla, Abdalla Abdalrazig. "Production of Silicon From Sand by Magnesium." (2014).

16. Krebs, Robert E. The history and use of our earth's chemical elements: a reference guide. Greenwood Publishing Group, 2006.
17. Bansal, Shonak, et al. "A highly efficient bilayer graphene/ZnO/silicon nanowire based heterojunction photodetector with broadband spectral response." Nano technology 31.40 (2020): 405205.
18. Casalino, Maurizio, et al. "State-of-the-art all-silicon sub-bandgap photodetectors at telecom and datacom wavelengths." Laser & Photonics Reviews 10.6 (2016): 895-921.
19. Bamola, Priyanka, et al. "Nanostructured Oxide Based Ceramic Materials for Light and Mechanical Energy Harvesting Applications." Advanced Ceramics for Energy and Environmental Applications. CRC Press, 2021. 116-135.
20. Morales-Narváez, Eden, Abdel-Rahim Hassan, and Arben Merkoçi. "Graphene oxide as a pathogen-revealing agent: sensing with a digital-like response." Angewandte Chemie 125.51 (2013): 14024-14028.
21. Banhart, Florian, Jani Kotakoski, and Arkady V. Krasheninnikov. "Structural defects in graphene." ACS nano 5.1 (2011): 26-41.
22. Georgakilas, Vasilios, et al. "Broad family of carbon nanoallotropes: classification, chemistry, and applications of fullerenes, carbon dots, nanotubes, graphene, nanodiamonds, and combined superstructures." Chemical reviews 115.11 (2015): 4744-4822.
23. Zhang, Yue, et al. "Functionalization of graphene sheets through fullerene attachment." Journal of Materials Chemistry 21.14 (2011): 5386-5391.
24. Su, Longxing, et al. "Self-powered ultraviolet photodetectors driven by built-in electric field." Small 13.45 (2017): 1701687.
25. Gangwar, Jitendra, Bipin Kumar Gupta, and Avanish Kumar Srivastava. "Prospects of Emerging Engineered Oxide Nanomaterials and their Applications." Defence Science Journal 66.4 (2016).
26. Rathi, Rakesh. Nanotechnology. S. Chand Publishing, 2009.
27. Wang, Jing, et al. "Synthesis, properties and applications of ZnO nanomaterials with oxygen vacancies: a review." Ceramics International 44.7 (2018): 7357-7377.
28. Wen, Xin, Qingmin Zhang, and Zhuang Shao. "Magnetron sputtering for ZnO: Ga scintillation film production and its application research status in nuclear detection." Crystals 9.5 (2019): 263.
29. Ryu, Hanjun, and Sang-Woo Kim. "Emerging pyroelectric nanogenerators to convert thermal energy into electrical energy." Small 17.9 (2021): 1903469.
30. Lee, Youngsu. "Multi-Functional Optoelectronic Heterostructure Devices Based on Transfer Printing of Nanomaterials." (2021).
31. Brown, Matthew S., and Craig B. Arnold. "Fundamentals of laser-material interaction and application to multiscale surface modification." Laser precision microfabrication. Springer, Berlin, Heidelberg, 2010. 91-120.

32. Shugaev, Maxim V., et al. "Fundamentals of ultrafast laser–material interaction." Mrs Bulletin 41.12 (2016): 960-968.
33. Allmen, Martin V., and Andreas Blatter. Laser-beam interactions with materials: physical principles and applications. Vol. 2. Springer Science & Business Media, 2013.
34. Pyatenko, Alexander, et al. "Mechanism of pulse laser interaction with colloidal nanoparticles." Laser & Photonics Reviews 7.4 (2013): 596-604.
35. Migliore, Leonard R. Laser materials processing. CRC Press, 2018.
36. Escobar-Alarcón, L., et al. "Preparation and characterization of bismuth nanostructures deposited by pulsed laser ablation." Journal of Physics: Conference Series. Vol. 582. No. 1. IOP Publishing, 2015.
37. Stafe, Mihai, et al. "Pulsed laser ablation of solids." Rom. Rep. Phys 62.4 (2010): 758-770.
38. Itina, Tatiana E., et al. "Mechanisms of small clusters production by short and ultra-short laser ablation." Applied Surface Science 253.19 (2007): 7656-7661.
39. Amendola, V., and Meneghetti, M. “What controls the composition and the structure of nanomaterials generated by laser ablation in liquid solution?”, Physical Chemistry Chemical Physics, Vol. 15, No. 9, pp. 3027-3046, 2013.
40. Amendola, V., and Meneghetti, M,. “Laser ablation synthesis in solution and size manipulation of noble metal nanoparticles“ Physical chemistry chemical physics, Vol. 11, No. 20, pp. 3805-3821, 2009.
41. Yang, L., et al. "Growth of diamond nanocrystals by pulsed laser ablation of graphite in liquid." Diamond and Related Materials 16.4-7 (2007): 725-729.
42. Rao, M. C. "Pulsed Laser Deposition—Ablation Mechanism and Applications." International Journal of Modern Physics: Conference Series. Vol. 22. World Scientific Publishing Company, 2013.
43. Rao, M. C. "Pulsed Laser Deposition—Ablation Mechanism and Applications." International Journal of Modern Physics: Conference Series. Vol. 22. World Scientific Publishing Company, 2013.
44. Eason, Robert, ed. Pulsed laser deposition of thin films: applications-led growth of functional materials. John Wiley & Sons, 2007.
45. Zhang, M.L., Peng, K.Q., Fan, X., Jie, J.S., Zhang, R.Q., Lee, S.T. and Wong, N.B. (2008) ‘Preparation of large-area uniform silicon nanowires arrays through metal-assisted chemical etching’, Journal of Physical Chemistry C, Vol. 112, pp.4444–4450.
46. Cao, Dao Tran, et al. "Effect of AgNO3 concentration on structure of aligned silicon nanowire arrays fabricated via silver–assisted chemical etching." International journal of nanotechnology 10.3-4 (2013): 343-350.
47. Aslani, Alireza. "Microscopy Methods in Nanochemistry." Current microscopy contributions to advances in science and technology. A Méndez-Vilas (Ed.). Formatex Research Center, Microscopy Book Series 5.2 (2012): 1291-1311.

48. Tian, B.Z., Zheng, X.L., Kempa, T.J., Fang, Y., Yu, N.F., Yu, G.H., Huang, J.L. and Lieber, C.M. (2007) 'Coaxial silicon nanowires as solar cells and nanoelectronic power sources', Nature, Vol. 449, pp.885–889.
49. Sun, X., Lin, L., Li, Z., Zhang, Z. and Feng, J. (2009) 'Fabrication of silver-coated silicon nanowire arrays for surface-enhanced Raman scattering by galvanic displacement processes', Applied Surface Science, Vol. 256, pp.916–920.
50. Chow, Philip CY, and Takao Someya. "Organic photodetectors for next-generation wearable electronics." Advanced Materials 32.15 (2020): 1902045.
51. Ouyang, Weixin, et al. "Enhancing the photoelectric performance of photodetectors based on metal oxide semiconductors by charge-carrier engineering." Advanced Functional Materials 29.9 (2019): 1807672.
52. Yotter, Rachel A., and Denise Michelle Wilson. "A review of photodetectors for sensing light-emitting reporters in biological systems." IEEE Sensors Journal 3.3 (2003): 288-303.
53. Schaefer-Prokop, Cornelia, et al. "Digital radiography of the chest: detector techniques and performance parameters." Journal of thoracic imaging 18.3 (2003): 124-137.
54. Basant, C.; S., P.L.; B., K.S.; R., R.C.N. Infrared Photodetectors Based on Reduced Graphene Oxide and Graphene Nanoribbons. Advanced Materials 2011, 23, 5419–5424. doi:10.1002/adma.201101414.
55. Chitara, B.; Krupanidhi, S.B.; Rao, C.N.R. Solution processed reduced graphene oxide ultraviolet detector. Applied Physics Letters 2011, 99, 2013–2016. doi:10.1063/1.3640222.
56. Chang-Jian, S.K.; Ho, J.R.; Cheng, J.W.J.; Hsieh, Y.P. Characterizations of photoconductivity of graphene oxide thin films. AIP Advances 2012, 2, 022104. doi:10.1063/1.3702871.
57. Guo, W.; Xu, S.; Wu, Z.; Wang, N.; Loy, M.M.T.; Du, S. Oxygen-Assisted Charge Transfer Between ZnO Quantum Dots and Graphene. Small 2013, 9, 3031–3036. doi:10.1002/smll.201202855.
58. Lai, S.K.; Tang, L.; Hui, Y.Y.; Luk, C.M.; Lau, S.P. A deep ultraviolet to near-infrared photoresponse from glucose-derived graphene oxide. Journal of Materials Chemistry C 2014, 2, 6971. doi:10.1039/C4TC01175A.
59. Liu, H.; Sun, Q.; Xing, J.; Zheng, Z.; Zhang, Z.; Lu, Z.; Zhao, K. Fast and Enhanced Broadband Photoresponse of a ZnO Nanowire Array/Reduced Graphene Oxide Film Hybrid Photodetector from the Visible to the Near-Infrared Range. ACS Applied Materials & Interfaces 2015, 7, 6645–6651. doi:10.1021/am509084r.
60. Shao, D.; Gao, J.; Chow, P.; Sun, H.; Xin, G.; Sharma, P.; Lian, J.; Koratkar, N.A.; Sawyer, S. Organic?Inorganic Heterointerfaces for Ultrasensitive Detection of Ultraviolet Light. Nano Letters 2015, 15, 3787–3792. doi:10.1021/acs.nanolett.5b00380.

61. Dang, V.Q.; Trung, T.Q.; Kim, D.I.; Duy, L.T.; Hwang, B.U.; Lee, D.W.; Kim, B.Y.; Toan, L.D.; Lee, N.E. Ultrahigh Responsivity in Graphene–ZnO Nanorod Hybrid UV Photodetector. Small 2015, 11, 3054–3065. doi:10.1002/smll.201403625. 28 of 30.
62. Cheng, Ching-Cheng, et al. "Self-powered and broadband photodetectors based on graphene/ZnO/silicon triple junctions." Applied Physics Letters 109.5 (2016): 053501.
63. Ito, Y.; Zhang, W.; Li, J.; Chang, H.; Liu, P.; Fujita, T.; Tan, Y.; Yan, F.; Chen, M. 3D Bicontinuous Nanoporous Reduced Graphene Oxide for Highly Sensitive Photodetectors. Advanced Functional Materials 2016, 26, 1271–1277. doi:10.1002/adfm.201504146.
64. Yang, H.; Cao, Y.; He, J.; Zhang, Y.; Jin, B.; Sun, J.L.; Wang, Y.; Zhao, Z. Highly conductive free-standing reduced graphene oxide thin films for fast photoelectric devices. Carbon 2017, 115, 561–570. doi:10.1016/j.carbon.2017.01.047.
65. Liu, Yu, et al. "Enhanced ultra-violet photodetection based on a heterojunction consisted of ZnO nanowires and single-layer graphene on silicon substrate." Electronic Materials Letters 16.1 (2020): 81-88.
66. Bansal, Shonak, et al. "A highly efficient bilayer graphene/ZnO/silicon nanowire based heterojunction photodetector with broadband spectral response." Nanotechnology 31.40 (2020): 405205.
67. Mondal, Hasmat, Tamal Dey, and Rabaya Basori. "Silicon nanowire arrays with nitrogen-doped graphene quantum dots for photodetectors." ACS Applied Nano Materials 4.11 (2021): 11938-11948.
68. Singh, Pooja, et al. "Development of an ultrasensitive IR sensor using ZnO/SiNWs hybrid nanostructure." Materials Today: Proceedings 66 (2022): 2303-2307. 69. Iqbal, Muhammad Aamir, et al. "Nanostructures/graphene/silicon junction-based high-performance photodetection systems: progress, challenges, and future trends." *Advanced Materials Interfaces* 10.7 (2023): 2202208.
69. Hussein, Mohammed T., and Mohammed Jawad H. Kadhim. "Study the Optical and Structural Properties for Thin Film Zinc Oxide (ZNO) Produced by Pulsed Laser Deposition." Journal of University of Babylon for Pure and Applied Sciences 27.4 (2019): 223-229.
70. A. Giardini, V. Marotta, A. Morone, S. Orlando, and G. Parisi, Thin films deposition in RF generated plasma by reactive pulsed laser ablation. Applied Surface Science, 2002. 197: p. 338.
71. Eason, Robert, ed. Pulsed laser deposition of thin films: applications-led growth of functional materials. John Wiley & Sons, 2007.
72. Krebs, Hans-Ulrich, et al. "Pulsed laser deposition (PLD)--a versatile thin film technique." Advances in Solid State Physics (2003): 505-518.
73. King-Smith, P. Ewen, Erich A. Hinel, and Jason J. Nichols. "Application of a novel interferometric method to investigate the relation between lipid layer

thickness and tear film thinning." Investigative ophthalmology & visual science 51.5 (2010): 2418-2423.
74. G. E. Jauncey, The Scattering of X-Rays and Bragg's Law. Proceedings of the National Academy of Sciences of the United States of America, 1924. 10(2): p. 57.
75. D. E. Sands, Introduction to crystallography, Courier Corporation, 1993.
76. Madhavi, J. J. S. A. S. "Comparison of average crystallite size by X-ray peak broadening and Williamson–Hall and size–strain plots for VO2+ doped ZnS/CdS composite nanopowder." SN Applied Sciences 1.11 (2019): 1509.
77. Liu, Hui, et al. "Cathodoluminescence modulation of ZnS nanostructures by morphology, doping, and temperature." Advanced Functional Materials 23.29 (2013): 3701-3709.
78. Wang, Ming, and Liping Liu. "Investigation of microscale aging behavior of asphalt binders using atomic force microscopy." Construction and Building Materials 135 (2017): 411-419.
79. Mwema, Fredrick Madaraka, et al. "Atomic force microscopy analysis of surface topography of pure thin aluminum films." Materials Research Express 5.4 (2018): 046416.
80. Motzkus, Charles, et al. "Size characterization of airborne SiO 2 nanoparticles with on-line and off-line measurement techniques: an interlaboratory comparison study." Journal of nanoparticle research 15 (2013): 1-36.
81. Karoutsos, Vagelis. "Scanning probe microscopy: Instrumentation and applications on thin films and magnetic multilayers." Journal of nanoscience and nanotechnology 9.12 (2009): 6783-6798.
82. W. Zhou, R. Apkarian, Z. L. Wang, and D. Joy, Fundamentals of scanning electron microscopy (SEM), in Scanning microscopy for nanotechnology, Springer, 2006.
83. A. Ul-Hamid, A beginners' guide to scanning electron microscopy. Vol. 1. ,Springer, 2018.
84. Ketenoglu, Didem. "A general overview and comparative interpretation on element-specific X-ray spectroscopy techniques: XPS, XAS, and XRS." X-Ray Spectrometry 51.5-6 (2022): 422-443.
85. Liu, Nian, et al. "Functionalization of silicon nanowire surfaces with metal-organic frameworks." Nano Research 5 (2012): 109-116.
86. Jones, Robin R., et al. "Raman techniques: fundamentals and frontiers." Nanoscale research letters 14 (2019): 1-34.
87. Mosca, Sara, et al. "Spatially offset Raman spectroscopy." Nature Reviews Methods Primers 1.1 (2021): 21.
88. Piscanec, S., et al. "Raman spectroscopy of silicon nanowires." Physical Review B 68.24 (2003): 241312.

89. Fu, Xiaoqi, et al. "Excitation profile of surface-enhanced Raman scattering in graphene–metal nanoparticle based derivatives." Nanoscale 2.8 (2010): 1461-1466.
90. Bykkam, Satish, et al. "Few layered graphene sheet decorated by ZnO nanoparticles for anti-bacterial application." Superlattices and Microstructures 83 (2015): 776-784.
91. Landi Jr, Salmon, et al. "Use and misuse of the Kubelka-Munk function to obtain the band gap energy from diffuse reflectance measurements." Solid state communications 341 (2022): 114573.
92. Abdullahi, Sabiu Said, et al. "Sımple method for the determınatıon of band gap of a nanopowdered sample usıng Kubelka Munk theory." NAMP J 35 (2016): 241-246.
93. Barhoumi, A., et al. "Aluminum doped ZnO thin films deposited by direct current sputtering: structural and optical properties." Superlattices and Microstructures 82 (2015): 483-498.
94. Deng, Ruopeng, et al. "Optical and transport measurement and first-principles determination of the ScN band gap." Physical Review B 91.4 (2015): 045104.
95. Eichler, H. J., and Hermerschmidt, A. (2006). Light-induced dynamic gratings and photorefraction. In Photorefractive Materials and Their Applications. Springer, New York, NY.
96. Sun, J., and Kosel, J. (2012). Finite-element modelling and analysis of hall effect and extraordinary magnetoresistance effect. Finite Element Analysis-New Trends and Developments, p. 201-224.
97. Popovic, R. S. (2004). Hall Effect Devices, Published by CRC Press.
98. G. B. Armen, Hall Effect Experiment. Department of Physics and Astronomy, 2007. 401: p. 37996.
99. Schroder, Dieter K. Semiconductor material and device characterization. John Wiley & Sons, 2015.
100. Lim, Jongchul, et al. "Long-range charge carrier mobility in metal halide perovskite thin-films and single crystals via transient photo-conductivity." Nature Communications 13.1 (2022): 4201.
101. Laquai, Frédéric, et al. "Charge carrier transport and photogeneration in P3HT: PCBM photovoltaic blends." Macromolecular rapid communications 36.11 (2015): 1001-1025.
102. Hyseni, Genc, Nebi Caka, and Kujtim Hyseni. "Infrared thermal detectors parameters: semiconductor bolometers versus pyroelectrics." WSEAS Trans. Circuits Syst 9.4 (2010): 238-247.
103. Kasap, Safa O., and John A. Rowlands. "Review X-ray photoconductors and stabilized a-Se for direct conversion digital flat-panel X-ray image-detectors." Journal of materials science: materials in electronics 11 (2000): 179-198.
104. Zhang, Ye, et al. "Graphdiyne-based flexible photodetectors with high responsivity and detectivity." Advanced Materials 32.23 (2020): 2001082.

105. Callister, W. D. (2006). An introduction: material science and engineering. John Wiley and Sons Inc.
106. Sze, S. M., and Kwok, K. Ng. (2006). Physics of Semiconductor Devices. John wiley and sons.
107. Kressel, H. (2012). Semiconductor lasers and herterojunction LEDs. Elsevier.
108. Milnes, A. G. (2012). Heterojunctions and metal semiconductor junctions. Elsevier.
109. De Visschere, P., Burgelman, M., and Pauwels, H. (1987). II–VI heterojunction device physics. Solid-State Electronics, 30(11): p. 1215-1220.
110. Goetzberger, A., Knobloch, J., and Voss, B. (1998). Crystalline silicon solar cells (Vol. 1). Chichester: Wiley.
111. Tanabe, K. (2021). Nanostructured Materials for Solar Cell Applications. Nanomaterials, 12(1): p. 26.
112. Colinge, J. P., and Colinge, C. A. (2005). Physics of semiconductor devices. Springer Science and Business Media.
113. Martil, I., and Diaz, G. G. (1992). Determination of the dark and illuminated characteristic parameters of a solar cell from IV characteristics. European journal of physics, 13(4): p. 193.
114. Priambodo, P. S., Sukoco, D., Purnomo, W., Sudibyo, H., and Hartanto, D. (2013). Electric energy management and engineering in solar cell system. Solar Cells–Res Appl Perspect, InTech, 12: p. 327-351.
115. El Assyry, A., Lamsayah, M., Warad, I., Touzani, R., Bentiss, F., and Zarrouk, A. (2020). Theoretical investigation using DFT of quinoxaline derivatives for electronic and photovoltaic effects. Heliyon, 6(3): p. e03620.
116. Kalogirou, S. (Ed.). (2017). McEvoy's handbook of photovoltaics: fundamentals and applications. Academic Press.
117. Yang, Zongxian, et al. "Large-scale production of highly stable silicon monoxide nanowires by radio-frequency thermal plasma as anodes for high-performance Li-ion batteries." Journal of Power Sources 497 (2021): 229906.
118. Luo, Wei, et al. "Critical thickness of phenolic resin-based carbon interfacial layer for improving long cycling stability of silicon nanoparticle anodes." Nano Energy 27 (2016): 255-264.
119. Xiao, Zhexi, et al. "Uniform coating of nano-carbon layer on SiOx in aggregated fluidized bed as high-performance anode material." Carbon 149 (2019): 462-470.
120. Strankowski, Michał, et al. "Polyurethane nanocomposites containing reduced graphene oxide, FTIR, Raman, and XRD studies." Journal of Spectroscopy 2016 (2016).
121. Surekha, G., et al. "FTIR, Raman and XRD analysis of graphene oxide films prepared by modified Hummers method." Journal of Physics: Conference Series. Vol. 1495. No. 1. IOP Publishing, 2020.

122. Al-Ruqieshi, Majid Salim Mohammed. *Synthesis and Characterization of Silicon Oxide and Silicon Carbide Nanostructures*. University of Malaya (Malaysia), 2010.

123. Van Heerden, J. L., and R. Swanepoel. "XRD analysis of ZnO thin films prepared by spray pyrolysis." Thin Solid Films 299.1-2 (1997): 72-77.
124. Srivastava, Varsha, Deepak Gusain, and Yogesh Chandra Sharma. "Synthesis, characterization and application of zinc oxide nanoparticles (n-ZnO)." Ceramics International 39.8 (2013): 9803-9808.
125. Sirelkhatim, Amna, et al. "Review on zinc oxide nanoparticles: antibacterial activity and toxicity mechanism." Nano-micro letters 7 (2015): 219-242.
126. Biroju, Ravi K., et al. "Catalyst free growth of ZnO nanowires on graphene and graphene oxide and its enhanced photoluminescence and photoresponse." Nanotechnology 26.14 (2015): 145601.
127. Fan, Zhanxi, et al. "Facile synthesis of gold nanomaterials with unusual crystal structures." Nature Protocols 12.11 (2017): 2367-2376.
128. Chakraborty, Pranay, et al. "Lattice thermal transport in superhard hexagonal diamond and wurtzite boron nitride: A comparative study with cubic diamond and cubic boron nitride." Carbon 139 (2018): 85-93.
129. Boruah, Buddha Deka, Anwesha Mukherjee, and Abha Misra. "Sandwiched assembly of ZnO nanowires between graphene layers for a self-powered and fast responsive ultraviolet photodetector." Nanotechnology 27.9 (2016): 095205.
130. Gaidi, Mounir, et al. "Enhanced photocatalytic activities of silicon nanowires/graphene oxide nanocomposite: Effect of etching parameters." Journal of Environmental Sciences 101 (2021): 123-134.
131. Cheng, Ching-Cheng, et al. "Self-powered and broadband photodetectors based on graphene/ZnO/silicon triple junctions." Applied Physics Letters 109.5 (2016): 053501.
132. Liu, Yu, et al. "Enhanced ultra-violet photodetection based on a heterojunction consisted of ZnO nanowires and single-layer graphene on silicon substrate." Electronic Materials Letters 16.1 (2020): 81-88.
133. Bansal, Shonak, et al. "A highly efficient bilayer graphene/ZnO/silicon nanowire based heterojunction photodetector with broadband spectral response." Nanotechnology 31.40 (2020): 405205.
134. Xue, Jingjing, Rui Wang, and Yang Yang. "The surface of halide perovskites from nano to bulk." Nature Reviews Materials 5.11 (2020): 809-827.
135. Weber, Matthieu, et al. "High-performance nanowire hydrogen sensors by exploiting the synergistic effect of Pd nanoparticles and metal–organic framework membranes." ACS applied materials & interfaces 10.40 (2018): 34765-34773.

136. Ghosh, Ramesh, Arindam Pal, and P. K. Giri. "Quantitative analysis of the phonon confinement effect in arbitrarily shaped Si nanocrystals decorated on Si nanowires and its correlation with the photoluminescence spectrum." Journal of Raman Spectroscopy 46.7 (2015): 624-631.

137. Yu, D. P. "Wide Band-Gap Semiconductor Nanowires Synthesized by Vapor Phase Growth." *Nanowires and Nanobelts: Materials, Properties and Devices. Volume 1: Metal and Semiconductor Nanowires*. Boston, MA: Springer US, 2003. 343-391.